POLITECNICO DI MILANO

Dipartimento di Elettronica Informazione e Bioingegneria

Piezoelectric energy harvesting from galloping instability: numerical model and experimental tests

Relatrice: Gisella Marita Tomasini

Correlatore: Stefano Giuseppe Giappino

Tesi di laurea di:

Mattia Marsetti - Matr. 833603

Anno accademico 2016/2017

Mattia Marsetti

Piezoelectric energy harvesting from galloping instability:
numerical model and experimental tests

Tesi di Laurea Magistrale in Automation and Control Engineering

Mattia.Marsetti@mail.polimi.it

Data di esposizione
21-12-2016

To Anas, Luckman, Rakia

this page intentionally left blank

CONTENTS

LIST OF FIGURES

LIST OF TABLES

LIST OF SYMBOLS

$X_{i,j}$	For the property named 'X' the first subscript indicates the material used ("p": piezoelectric layer, "s": supporting beam, "b": bluff body, "e": extension for the bluff body). The second subscript, if present, indicates the region in which the property "X" is considered
$\phi_j{}^{(i)}$	i-th mode of vibration for the region j
$V_{i,j}$	Volume of the material i for the region j
w_i	Width of layer i
ρ_i	Density of layer i
t_i	Thickness of layer i
m_i	Mass per unit length of layer i
c_i	Young modulus of layer i
D	Side width of the bluff body
f_n	Natural frequency of the system expressed in Hz
ω_n	Natural frequency of the system expressed in rad/s
h	Non-dimensional damping of the system
r_{aero}	Aerodynamic damping
r_{mech}	Structural (mechanical) damping
r_{ele}	Electrical damping
$r_{m_{el}}$	Overall mechanical and electrical damping
A	Surface of the bluff body that is hit by the flow
c_s	Strouhal number

d_i	Distance of the layer i from the neutral axis of the region j
ρ_{bluff}	Bluff body density
ρ_{air}	Air density
L_j	Length of the region j
P	Output electrical power
S_i	Strain of layer i
U	wind speed
U_r	Vortex shedding resonance speed
U_g	Galloping onset speed
U^*	Reduced wind speed
V_r	Relative speed
η	Efficiency of conversion
V_{conn}	Voltage output for the connection selected; "*conn*" indicates whether the connection is parallel "p" or series "s"
C_{conn}	Capacitance obtained for the connection selected
χ_{conn}	Electromechanical coupling obtained for the connection selected

ABSTRACT

The purpose of the present research is to realize a working prototype to be installed on freight trains for the power sustainability of a wireless sensor node required for structural diagnosis. The work deals with the modelling, designing and validating of a galloping piezoelectric energy harvester. Using the piezoelectric effect, this system is able to convert the energy from bending vibrations, induced by the galloping aerodynamic instability, into usable electric energy.

Subject of the first part of the analysis is the development of a non-linear coupled distributed model that predicts the limit cycle oscillation of the device, together with the power output produced for different resistive load connected and for various wind speeds considered.

A sensitivity analysis follows, in which the parameters of the galloping energy harvester are varied in order to evaluate the effects on the maximum power output and the minimum onset speed gathered. Based on the conclusions of this analysis, different prototypes are realized for the achievement of various objectives.

Results of base excitation tests are then presented, which show good accuracy of the electromechanical model. An experimental procedure is set in order to identify an appropriate galloping force model from the wind tunnel experiments. The results are interpreted with respect to the hypothesis behind the model proposed, in particular with respect to the vortex shedding resonance.

Keywords: energy harvesting; galloping instability; piezoelectricity; wind tunnel

Lo scopo del presente lavoro è di realizzare un prototipo di recupero energetico da montare a bordo di treni merci per finalità diagnostiche. La trattazione documenta il processo realizzativo a partire dallo sviluppo di un modello analitico, la sua analisi e la validazione. Tramite l'effetto piezoelettrico, il prototipo è studiato per convertire in energia elettrica l'energia meccanica delle vibrazioni indotte dall'instabilità aerodinamica del galoppo.

Soggetto della prima parte della ricerca è lo sviluppo di un modello non-lineare che descrive l'accoppiamento elettromeccanico del sistema ed è in grado di predire i cicli limite delle oscillazioni del dispositivo, assieme alla potenza recuperata nelle possibili velocità di vento imposte e per diversi carichi resistivi connessi.

Una analisi di sensibilità segue con lo scopo di mostrare quali parametri del modello producono una minore velocità minima della vena che produca l'instabilità e quali altri siano vantaggiosi per migliorare l'efficienza di conversione. Basandosi sulle conclusioni di questo studio è possibile determinare quali prototipi siano da realizzare per conseguire diversi obiettivi.

Una serie di esperimenti di validazione viene infine presentata per provare la validità del modello sviluppato: il comportamento elettromeccanico viene valutato con prove ad eccitazione impressa alla base. Dalle prove in galleria del vento viene invece identificato un modello per descrivere la forza del galoppo. Un ulteriore commento ai risultati viene fornito in merito al fenomeno di interferenza con il distacco di vertici e per quanto riguarda la validità delle ipotesi adottate nella trattazione.

Parole chiave: recupero energetico; instabilità da galoppo; galleria del vento

INTRODUCTION

The energy harvesting, or energy scavenging, is the research field that investigates the various possibilities to convert into usable power different form of energies available in the environment. In a world of technological advances, power demands are becoming more significantly a task to be achieved in many applications in order to guarantee sustainability and longevity. Batteries, despite some improvements, are remaining far beyond the requisites of long-term and low-maintenance use and therefore many research topics are currently under investigations, that promote different ways to provide power to small and smart electronics. At the same time, thanks to the progress in miniaturized sensors and processors, many researchers are studying wireless sensor nodes. These low-power demand devices are able to wirelessly communicate, exchanging information over a wide area for diagnostic purposes in a variety of fields. This scenario has gathered the raise of a new generation of power devices, capable of self-powering and of an autonomous and intelligent data management.

A wide number of researches have explored the fields of solar, thermal and body-derived energy harvesting. This effort provides the possibility to deploy large autonomous sensor networks, that are powered using the most suitable ambient resources in each context. For the latter reason, the fluid-flow energy harvesting is currently representing a promising source of energy for those environments in which sufficient flow velocities are present. There are two main research fields that explore energy conversion method from wind or water flows. The first one is represented by centimeter-scale turbines, which show high efficiency and power density mostly for a relatively high range of flow speeds. The second method, which grants acceptable power levels starting from a lower set of wind speeds, harvests the mechanical energy induced by various aerodynamic instabilities. The core of these devices is typically an airfoil or a bluff body and the preferred conversion method is the piezoelectric

effect. Among vortex or wake induced vibrations and flutter instabilities, galloping has proven to be the most promising instability, since it offers sufficient power densities for a wide range of fluid speeds.

The present investigation is intended to describe the realization of a galloping piezoelectric energy harvester, with the purpose to provide sufficient power for a wireless sensor application. Under an experimental and analytical procedure, the study is aimed at giving the guidelines for the optimization of a galloping piezoelectric energy harvester and at validating the simulated predictions on the realized devices.

The phenomenon of galloping was first studied to explain the unstable motion of transmission lines [1]; then an empirical model was retrieved and validated in 1964 [2]. In the next decades, this instability has been mostly known in civil engineering, for the disruptive effects that it can have over towers and bridges. The idea of applying galloping to the energy harvesting world is found after a recent study [3], dated 2010. In the last years, a few experimental researches [4] [5] have shown the possibility to harvest energy in the order of mW for wind speeds up to 8 m/s. Other studies have focused on the optimization of a galloping energy harvester according to analytical or numerical methods [6] [7].

With respect to the works cited, in this research not only an analytical model is developed, but ad hoc tests are performed in order to identify the characteristic parameters. The interaction with vortex shedding is taken into consideration, with the consequences on the validity of the model adopted. According to numerical simulations, the dependence upon different parameters is considered for what concern the achievable performances.

These tasks are accomplished starting with the development of an analytical model for the harvester, which accounts for the non-linear effect of the galloping force and the coupling between the electrical and mechanical equations. By simulating the model for different configurations, a sensitivity analysis is carried out, that shows which parameters can grant higher power output and a sustainable fatigue. A prototype that can satisfy the target application is then realized and tested. For the identification of the different parameters and the validation of the model various experiments are performed: the electromechanical model validation is obtained with the use of a shaker for imposed motion, while the aerodynamic force model is evaluated within a wind tunnel facility. The limit cycle oscillations reached for a different set of wind speeds and resistive loads connected are then shown to be consistent with the numerical predictions, together with the power output. Observations are drawn on the impact that the vortex shedding interference has on a galloping energy harvester.

In detail, the present work is divided into four chapters and a conclusive section. It shows the development and analysis of an analytical model and the experimental validation through a series of tests.

As described in Chapter 1, many energy sources are available in nature and energy harvester devices are specifically designed in order to take advantage of the particular environment in which they are set. Different energy conversion methods are presented for what concerns the vibrational energy harvester family; advantages and disadvantages are shown for each of them. The piezoelectric effect is determined to be the most suitable method for the present application and it is chosen for the realization of a prototype. The wind energy harvesting topic is then addressed and different experimental researches are compared in order to evaluate the most suitable technique. The galloping aerodynamic instability is found to be the most appropriate phenomena to harvest a sufficient amount of energy for a wide range of fluid velocities.

The model of a vibrational harvester is developed through Chapter 2. The galloping force model is presented according to the quasi-steady theory. The model of the mechanical device together with the electromechanical coupling mechanism is described applying the Lagrangian equation.

A sensitivity analysis is carried out in Chapter 3, where the objective is the investigation of the effects that each parameter variation has on the overall performance of the harvester. The conclusions allow to establish which geometrical design fits the application targets and therefore indicate the principles to realize an optimized device.

Chapter 4 illustrates the realization of the prototypes according to the optimization knowledge achieved. The modal mass and natural frequency of each device is compared with the numerical prediction. The electromechanical model is further validated using a comparison between the numerical and experimental transfer functions obtained via an input base motion. The prototypes are then tested inside a wind tunnel facility to compare the approximation of the galloping force model. An identification process is set up in order to identify the aerodynamic coefficients that describe the galloping force. This identified model is then evaluated according to the experimental power output and displacement reached by the prototypes, so that the validity of the analytical procedure is proved. limits of the model are underlined, regarding the lower reduced speed range at which the results obtained are not following the predictions.

The final chapter is a summary of the obtained results, regarding the optimization of the harvester and its validation with the experimental data. Limits of the theory applied are proven to exist according to the tests performed. Objectives of the future tasks to be

accomplished are illustrated in order to come to the realization of a working prototype with better performance.

1 STATE OF THE ART

This chapter is intended to give to the reader a brief and general view of the energy harvesting scenario, with particular focus on the wind energy harvesting brand. A comparison between the main energy sources for harvesting is then given in terms of power densities as a motivation for the present study. A general review of the possible power conversion mechanisms is given and an evaluation of the achievable performances of each strategy is conducted by referring to real prototypes. The wind energy harvesting field is presented with a review of the most important works that deal with vibrations induced by aerodynamic instabilities. Over the different possibilities illustrated, galloping is found to be the one that is most suitable for the purpose of the target application. A detailed explanation of the phenomenon follows, with a description of the most significant mathematical models presented in various researches for a galloping based energy harvester. The open questions left by other experimental studies are then addressed as a focus for the following work.

1.1 Energy Harvesting

Energy scavenging devices are designed to collect a small portion of the alternative form of energy surrounding the device and to transform it into a usable form of energy for a self-powered system. They are normally required to harvest the amount of power needed to operate a sensor and in general to maintain a wireless communication with a certain duty cycle. The main objective for an energy harvester is to sustain the power demands of the system which is connected to for an indefinite time, in such a way to make it an energetically autonomous system, requiring possibly minimum maintenance.

In recent years, the field of power harvesting has experienced a significant growth, mainly due to the increasing desire to sustain small power-requiring electronics able to communicate without wires and batteries. Technological advances have in fact made possible to implement miniaturized sensors and control units in compact packaging. Thus, it is nowadays common to design more complex and expanded sensor networks that have primary a need of being low-maintenance and long life-time devices. For the latter, it is clear the disadvantage that batteries show because they all present a limited life-time and also exhibit deterioration with time as reported in Figure 1.1. According to the study by Roundy [8], it is shown that the efficiency of the main types of batteries is typically deteriorating with time, so that after a maximum of 5 years even Lithium and Alkaline batteries have no longer acceptable performance. Many recent researches are aimed at replacing batteries in such devices in order to diminish maintenance costs and elongate the life-time of the device. Note also that for many applications it is desirable, if not even necessary, to avoid cables for a data/power connection due to the inaccessible location where it is to be installed a sensor or for the distance from the central controller. As a side example a self-powered monitoring system is especially useful for human body implants, where batteries removal requires additional surgery and, for a similar reason, in the case of structural buildings health monitoring where maintenance and installation costs would be very high for a cabled network.

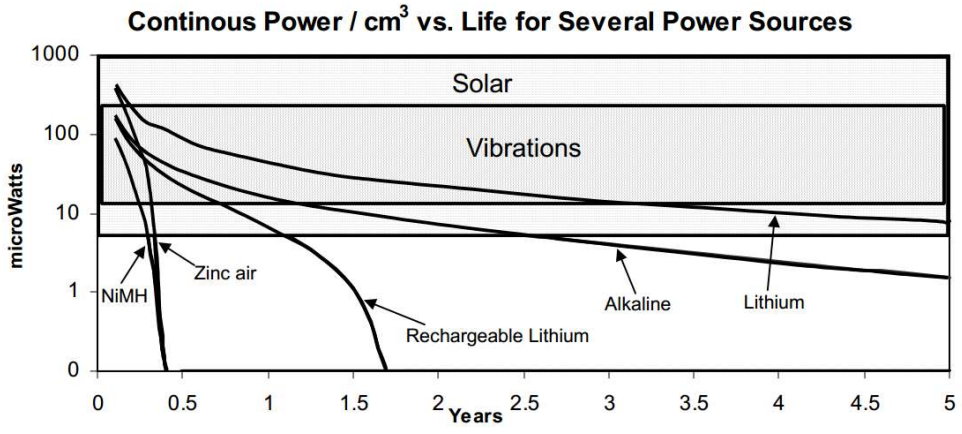

Figure 1.1 Power densities and life time of common energy sources [8]

Many technologies have been tested in various energy scavenging prototypes using a variety of power sources from heat to fluid waves and vibrations. Such devices are proved to be sufficiently efficient for common power node requirements. It must be noted anyway that for each application the appropriate harvesting method must be selected to fit the application.

1.2 Energy sources

The environment is full of different kind of accessible energy sources, that can be harvested with many different techniques. In some cases, it is possible to scale up a conversion device, but, for most of the applications where energy harvesters are used, limited volumes and weights are required. Thus, an important parameter to be evaluated in a preliminary study for a sensor node application is the power density that can be achieved for the specific system. It is generally expressed in W/m^3 or W/m^2, which indicates the amount of power that can be produced per volume or sectional area of the device. It is important because it states which is the minimum device volume required to harvest a certain amount of power. This measure is related to the fact that energy harvesting applications normally require small devices with adequate power capabilities. An energy harvesting system must also consider the impact that the harvesting produces on the subject environment: for example, blood flow has been considered for powering microelectronics devices for human health monitoring, but resulted in a non-acceptable application for the hearth effort [9]. For an introductory perspective, the reader is referred to Table 1.1 where the average power densities are shown for the types of ambient energy commonly harvested. In the following, the main techniques for power harvesting are described with reference to [10] [11].

	Power density [µW/cm^3] 1 Year lifetime	Power density [µW/cm^3] 10 Year lifetime	working principle
Solar (Outdoors)	15,000 - direct sun		photovoltaic
	150 - cloudy day		
Solar (Indoors)	6 - office desk		
Vibrations	200		piezoelectric/ magnetostrictive/ electrostatic/ electromagnetic
Shoe Inserts	330		
Acoustic Noise	0.003 - 75 Db		
	0.96 - 100 Db		
Daily Temp. Variation	10		thermoelectric
Temperature Gradient	15 per 10° gradient		
Batteries (non-recharg. Lithium)	45	3.5	electrochemical
Batteries (rechargeable Lithium)	7	0	
Hydrocarbon fuel (micro heat engine)	333	33	
Fuel Cells (methanol)	280	28	
Nuclear Isotopes (uranium)	6,00E+06	6,00E+05	nuclear

Table 1.1 Comparison of energy scavenging and energy storage methods

Solar energy

PV devices are capable of providing relatively high efficiency over a broad range of wavelengths. These devices are known for being typically low cost and for being able to provide the voltage and current levels needed to power microelectronic circuits. Despite these advantages, they highly depend on a series of factors that influences their harvesting capacity. First of all, the energy available on a particular location depends on its latitude, altitude, atmospheric condition and it is in the order of 100-300W$\cdot m^{-2}$(From the poles to the equator). In particular, the energy available drops down to zero during night time and varies during the day due to the incidence angle to the PV device. There already exist several commercial products with a typical efficiency of 15%.

The most significant disadvantage for this brand of power harvesting is that, if the harvester has to operate continuously, it must collect and store the energy needed for night time

operations. Another limit for this application is that it need to be placed outdoor for best energy harvesting since the indoor average energy levels are around 1 W· m^{-2} [11].

Thermal Energy

Extraction of energy from a thermal source is granted by a thermal gradient via the Seebeck effect or the pyroelectric effect. The effectiveness of these conversions is limited by the Carnot efficiency to:

$$\eta \leq \frac{T_h - T_c}{T_h} \tag{1.1}$$

where T_h and T_c are respectively the absolute temperature of the "hot" and "cold" side of the device. Thus, for a greater efficiency of conversion a more significant temperature gradient is required. Equation (2.102) represents a strong bottleneck on the application of energy thermal harvester. In a study by Starner [9] the entire human body was considered with a temperature gradient of 37°– 20°C (body temperature - ambient temperature). The resulting conversion efficiency of 5.5% would only yields to 6.4 W from the total dissipation of 116 W (sitting human body), while a device covering just the neck could potentially deliver 0.2-0.32W.

Note that energy conversion from thermal gradients is the basis of many large scale power plants, but such technologies are not generally scalable to the level required for sensor network nodes. For this reason, commercial devices typically implement thermocouples in arrays: with this technique, it is possible to provide 100 μW from a 10 K temperature differential with a device of 9.3 mm diameter. A commercial wearable device is the ©Seiko Thermic wristwatch, that uses 10 thermoelectric modules to generate sufficient microwatts to run its mechanical clock movement with body heat.

Mechanical sources

Sources of mechanical energy may be divided in three groups, as those dependent on a quasi-constant motion, those dependent on intermittent motion and those where the motion is cyclic as suggested by Gilbert and Balouchi [11].

1. As belonging to the first category of **steady state mechanical sources** wind or water flows are found. These types of energy source is available in common ventilation ducts, in natural/artificial water channels or in wind currents. Common techniques for harvesting applications in this area include micro wind turbines;
2. For **intermittent mechanical source,** it is intended the energy derived from a motion where power is generated only in a short part of the cycle. An attractive

source is, for instance, the human power dissipation during normal walking. This activity is capable of producing an average of 5.88 W per foot depending on the body weight, shoe deflection and walking frequency [9]. Another example to be considered is the process of vehicles passing over a deflection harvesting device, which is capable of collecting high quantity of energy, but where again the average power level is dependent upon the variable process frequency.

3. The most representative example of **cyclic sources** of energy are mechanical vibrations. They are found in most environments and normally they can be harvested without impacting the process that has generated it. The energy available depends mainly on the frequency and amplitudes of the vibrations. Those are commonly present as a series of superimposed harmonics of various amplitudes. Since an energy harvester is typically capable of narrow-frequencies energy conversion, the device must be appropriately selected in order to fit the system inputs. Note also that the characteristics of the vibrations may dramatically change due to a different configuration of the generating environment.

Power transfer

As an alternative to power harvesting, it must be noted that some researchers are trying to optimize techniques aimed at wirelessly transferring power from a central unit to a network of secondary nodes. In the work by Percy et al. [12] an autonomous radio frequency power transfer system is built. The base station is able to rotate in order to monitor the other nodes' charge status and to transfer power to the nodes that first need it within the range of 3 m. A conversion efficiency of 39.1% was found, but it must be considered that the efficiency highly depends upon the distance between the central node and the others, making this method less effective for wide networks.

1.2.1 Vibrational energy harvester

This section deals with vibrational-based energy, with focus on the energy densities available in different environments and on the most used techniques for energy conversion.

Sources of vibrations

Common daily life or industrial tools provide a wide range of vibrations available for energy scavenging. The work by Roundy [8] compared the energetic potential of typical environments as reported in Table 1.2. As it will be further explained in this chapter, there is also the possibility of inducing vibrations to the energy harvesting device by means of other mechanical phenomena such as fluid flows.

Vibration Source	Peak Acc. (m/s^2)	Frequency of Peak (Hz)
Base of 5 HP 3-axis machine tool with 36" bed	10	70
Kitchen blender casing	6.4	21
Clothes dryer	3.5	21
Door frame just after door closes	3.0	25
Small microwave oven	2.25	21
HVAC vents in office building	0.2 – 1.5	60
Wooden deck with people walking	1.3	85
Breadmaker	1.03	21
External windows (size 2 ft x 3 ft) next to a busy street	0.7	na
Notebook computer while CD is being read	0.6	75
Washing Machine	0.5	9
Second story floor of a wood frame office building	0.2	na
Refrigerator	0.1	240

Table 1.2 List of vibration sources with their maximum acceleration magnitude and frequency of peak acceleration [8]

Types of vibrational energy conversion

There are four main methods applied for energy conversion from vibrational sources that are presented in the following for a comparison. The general model describing a vibrational energy harvester is a mass-spring-damper system, such as the one reported in Figure 1.2. The system is composed of a seismic mass m and a spring of stiffness k:

$$m\ddot{x}(t) + b\dot{x}(t) + kx(t) = -m\ddot{u}(t) \tag{1.2}$$

The variable $x(t)$ represents the relative motion of the seismic mass associated to the system with respect to its equilibrium position, while $u(t)$ is the position of the entire device relative to the inertial frame. A damper is modeled as proportional to the velocity in order to account for the dissipation effects that occur due to losses and power conversion. The latter severely depends on the method of energy conversion considered.

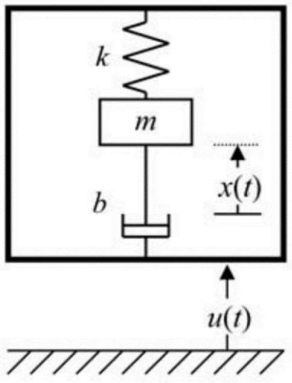

Figure 1.2 model of a translational inertial generator

Magnetostrictive conversion

Magnetostrictive conversion is based on the property of certain ferromagnetic material to exhibit strain under a magnetic field. In fact, at a microscopic level, the polarization direction, which is homogeneous in nominal condition, is directed according to the magnetic field direction, thus causing the material deformation. The well-known Villari effect is the opposite and it is applied in this conversion. As the external force stresses the material, inducing a change in the resulting magnetic field, the power is harvested with the use of a coil. In fact, the changing magnetic flux will cause an electromotive force inside the wire that can be used to power the load.

The magnetostrictive conversion is normally modelled as a linear phenomenon under the following hypothesis: low operational frequencies, constant strain over the material and reversible process. The following constitutive equations can then be written:

$$\begin{cases} S = s^H T + dH \\ B = dT + \mu^T H \end{cases} \tag{1.3}$$

Where T and S are the mechanical stress and strain respectively; B is the magnetic flux and H is the magnetic field respectively. Coefficients s^H and μ^T represent the compliance at constant magnetic field and the magnetic permeability at constant stress. The piezo-magnetic coefficient d describes the coupling between the mechanical and magnetic areas. Note that equation (1.3) is analogous to the constitutive equation of a piezoelectric material.

This technology has the disadvantage to require higher volumes with respect to the others presented in this chapter.

Electrostatic conversion

Electrostatic conversion is based on a parallel plate capacitor, pre-charged from an external source, whose plate geometry is varied through a mechanical effort. This results in a variation of voltage or charge that is used to provide electrical energy to a load.

The capacitance for a parallel plate capacitor with plate A and plate separation d is:

$$C = \varepsilon \frac{A}{d} = \frac{Q}{V} \tag{1.4}$$

Where ε is the dielectric constant of the insulating material, Q and V are respectively the charge and the Voltage on the capacitor. The energy stored on the capacitor is:

$$E = \frac{1}{2}QV \tag{1.5}$$

The conversion takes place as the voltage or the charge is constrained and the capacitor plates are moved by means of an external force. For instance, if the voltage is kept constant the resulting energy is computed by combining (1.4) and (1.5) as:

$$E = \varepsilon\frac{AV^2}{2d} \tag{1.6}$$

If the external force is then applied in the separation of the parallel plate, since force is the rate of change in energy with distance, the reaction force can be found from (1.6):

$$F = \varepsilon\frac{AV^2}{2d^2} \tag{1.7}$$

Roundy considered [8] three possible structures named out-of-plane gap closing, in-plane gap closing and in-plane overlap varying. He concluded that in-plane gap closing structures offer the greatest power output capability. In this configuration, the external mechanical force is employed to impose an oscillating motion to one of the plates, thus changing the total distance between plates with time.

Main disadvantage for this technique is the fact that an external voltage source is needed for pre-charging the capacitor, making it difficult to implement such harvester in a fully autonomous energy harvester. A second issue is represented by the fact that a mechanical limiter must be put in place in order to avoid the contact between the two parallel faces.

Electromagnetic conversion

An electromagnetic conversion relies on the relative motion between a magnet and a coil, which is responsible of a voltage generation as according to the Faraday's law. In a coil made up of N turns of side length l moving through a magnetic field with flux density B at a velocity $\dot{x}(t)$ the voltage generated is:

$$v(t) = NlB\dot{x}(t) \tag{1.8}$$

If we consider that the coil has a resistance R_c and an inductance L_c and that the conversion device is attached to a resistive load R_L, then the load current is:

$$i = \frac{v}{R_L + R_c + j\omega L_c} \tag{1.9}$$

The resulting force is then:

$$F = BlN \tag{1.10}$$

Which, considering that the vibration forces the system to oscillate with frequency ω, introduces the following damping b in equation (1.2):

$$b = \frac{(NlB)^2}{R_L + R_c + j\omega L_c} \tag{1.11}$$

A number of authors have considered a series of electromagnetic conversions prototypes ranging from MEMS (Micro Electro-Mechanical Systems) to larger scale devices, which represents an advantage for this technology that has a great scalability. It has also been shown by experimental proof that a conversion device of this shape is capable of converting energy with an efficiency of up to 30% in the optimized prototype described in the work by Beepy et al. [13]. The voltage output is typically very low (in the order of hundreds of millivolts) and therefore it normally requires an amplification device before the power harvested can be used by the device connected. Anyway, this conversion method presents the advantage that is has no contacting parts and therefore it typically presents a low damping together with the fact that it is autonomous from an external power source.

Piezoelectric conversion

A piezoelectric material has the property that if subjected to strain it exhibits a proportional generation of electric field. In fact, strain energy results in a deformation of the dipole and the formation of charge, that can be removed from the material to power a device. Conversely, if an electric field is applied it undergoes strain. Because of this reason this technique has received the most attention due to the ease at which it can be integrated into a system. The most common piezoelectric materials are *lead zirconate titanate* (PZT), which is a ceramic, and *Polyvinylidene fluoride (PVDF),* which is a polymer.

The constitutive equations that describe the behavior of a piezoelectric material are [14]:

$$S = s^E T + dE \tag{1.12}$$

$$D = \varepsilon^T E + dT \tag{1.13}$$

Where T and S are the mechanical stress and strain, D and E are the electric displacement and the electric field. The term s^E is the mechanical compliance when the electric field is

constant and ε^T is the dielectric constant (permittivity) under constant stress. The coefficient d causes coupling between the mechanical and electric domains. Note that without the latter coefficient equations (1.12) and (1.13) can be simply read as the Gauss' and Hooke's laws. In open circuit condition the output voltage can be evaluated as:

$$V_{oc} = -\frac{d}{\varepsilon} tT \tag{1.14}$$

where t is the distance between the surfaces of the piezoelectric material.

A piezoelectric material is typically capable of providing high voltages at low currents, allowing an appropriate harvester to power directly its interface, without the use of any extern power source. Moreover, these kinds of systems offer a great scalability, that has already been experienced up to the MEMS-dimension, where the main concern is that the electromechanical coupling is significantly reduced.

1.2.2 Performances

As a summary, the methods presented in the previous section are compared in Table 1.3**Errore. L'origine riferimento non è stata trovata.**, where for each technique are listed significant research activities with the relative power provided, volume of the device and vibrational input characteristics [11]. In the work by Du Toit [15], an investigation is developed on the feasibility of a MEMS-scale autonomous sensor network. The piezoelectric, electrostatic and electromagnetic power conversion methods are compared and the author concluded that piezoelectric devices have the highest power density per volume.

Operating mode	Author(s) [reference]	Output power (μW)	Frequency [Hz]	Amplitude [m/s^2]	Volume [mm^3]
piezoelectric	Glynne-Jones	2.1	80.1	2.3	125
	Roundy et al.	210	120	2.5	1 000
	Roundy et al.	375	120	2.5	1 000
	Marzencki et al.	0.6	900	9.81	2
electrostatic	Mitcheson et al.	3.7	30	50	750
	Despesse	1 052	50	8.8	1 800
	Despesse	70	50	9.2	32
electromagnetic	Shearwood and Yates	0.3	4 400	382	5.4
	Glynne-Jones et al.	180	322	2.7	840
	Perpetuum et al.	4 000	100	0.4	30 000

Table 1.3 Comparison between main researches held in the field of vibrational energy harvesting grouped per typology of conversion used [11]

1.3 Fluid energy harvesting

The field of energy harvesting from fluid flow is investigated in the present sub-chapter. There are two main categories belonging to this family of harvesters. The fluid may be conveniently converted into an electrical power thanks to centimeter-scale turbines equipped with electric generator. Otherwise, vibrations may be artificially induced by a proper aerodynamic instability, so that the induced vibrations are harvested according to the techniques previously exposed. The main advantages and disadvantages of each strategy are discussed, by reference to existing prototypes and with a final summary of the overall performances obtained in literature.

1.3.1 Wind and water micro-turbines

Windmills have been used to harvest energy for centuries and state of the art windmills have a power density of about 34 W/m^2. Their concept is to use the wind flow to induce a rotational motion of a fan which is connected to an electric motor that produces electric power. According to the Betz approach, the maximum power that an optimized turbine can generate is:

$$P = \frac{1}{2}\rho_{air} A C_B U^3 \tag{1.15}$$

where ρ_{air} is the air density, A the sectional turbine area, U the wind speed and C_B is equal to 0.59. As it will be shown in the following sections, this type of harvesters has the highest power to volume performance within the family of wind energy harvesters. A strong limitation for these harvesters is that they typically reach a critical speed over which the rotational parts undergo excessive stress and the device may be damaged. These systems are already employed for powering diagnostic sensors in ventilation ducts where flow speeds are below 10 m/s. It must be noted that maintenance cost is not negligible since a fan mechanism will require lubrication, which doesn't make this class of systems profitable for an autonomous self-powered device even if it is possible to realize very compact design. In Figure 1.3(a), it is illustrated the work by Howey et al. [16] with the final prototype of a centimeter-scale windmill that employs a permanent magnet generator.

A fairly new category of wind micro-turbines is formed by piezoelectric windmills, where the idea is to apply strain to a piezoelectric element thanks to the action of a wind flow. A significant example is the windmill by Priya [17] where the motion of a fan rotates a shaft connected to a circular array of 12 prestressed cantilevered piezoelectric bimorphs that is then subjected to oscillations as illustrated in Figure 1.3(b). Priya also established that the system can be severely damaged for wind speeds beyond 5 m/s. The advantage found for this configuration is that the power generation is allowed even for smaller fluid speeds with respect to the case of classical micro-turbines.

(a) (b)

Figure 1.3 (a) The micro-wind turbine proposed by Howey et al. (b) Piezoelectric windmill prototype with circular array of piezoelectric bimorphs developed by Priya S.

A second interesting option for a piezoelectric windmill has been proposed by Kan et al [18]. The core of the unit is again a fan that is forced to rotate by a wind flow. In this case the shaft is connected to a circular array of permanent magnets attached to a rotary disk. The consequent rotation of the magnetic field excites the magnets fixed on the tip of cantilevered piezoelectric elements placed on the fixed frame. The piezoelectric bimorphs are then subjected to an induced vibration, with a frequency depending on the rotational speed applied to the fan. The design proposed by the authors is reported in Figure 1.4. Even in this case a maximum critical speed is established around 13 m/s when contacting of the piezoelectric tip and the fixed frame takes place.

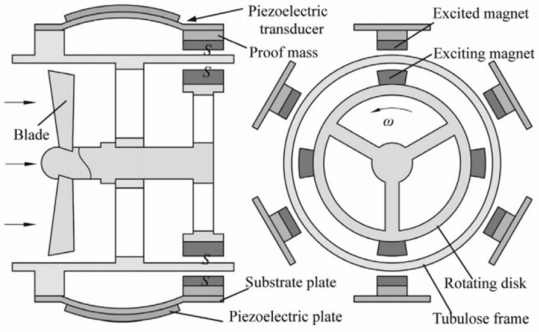

Figure 1.4 Piezo-magnetic windmill prototype design developed by Kan et al. [18]

1.3.2 Vibrations induced by aerodynamic instabilities

This is mainly the case in which the vibration present in the surrounding environment is not sufficient for the application power requirements or the case in which another form of energy

is available with major continuity or intensity. Flow induced vibrations are typically regarded as undesirable and destructive phenomena, that occur in a broad range of structures and have been studied in order to be avoided. In recent years, flow induced vibrations generated from ambient wind or water flows have been applied to the energy scavenging concept. In this way, it is possible to generate a mechanical oscillation if an appropriate design is studied to trigger the instability. The vibrating system is then used to extract power with one of the energetic conversions previously discussed. Different aerodynamic instabilities are present in several research studies, that are presented in the following sections.

Vortex induced vibrations energy harvesters

Vortex shedding is a phenomenon in which the air flowing past a bluff body creates an oscillating pressure field behind it, often referred to as a Karman vortex street, as depicted in Figure 1.5.

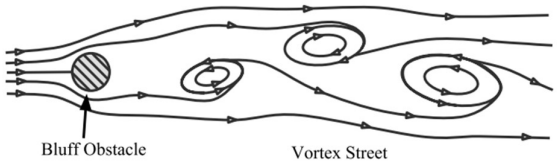

Figure 1.5 Streamline diagram of the vortex shedding phenomenon

The frequency f_s at which vortices shed from the bluff body, is proportional to the fluid speed and it is described by the Strouhal relation:

$$f_s = \frac{c_s U}{D} \tag{1.16}$$

where c_s is the Strouhal number, which depends on the cross-section geometry used, D is the diameter of the blunt body and U is the fluid velocity across the obstacle. The Strouhal number is a constant that depends upon the body cross-section geometry and in general its value is between 0.1 and 0.2.

When the body is free to oscillate in the direction orthogonal to the flow, it is then exposed to the oscillating force field described. If the Strouhal frequency f_s is close to the natural frequency f_n of the body, the latter is excited at its resonance and may undergo very high amplitude vibrations. The flow speed which guarantees the complete synchronization is the Strouhal speed, defined as:

$$U_r = f_n \frac{D}{c_s} \tag{1.17}$$

This phenomenon is called lock-in resonance and it is a particular synchronism that is maintained even if the flow speed changes in a narrow range of speeds (for a cylindrical body the flow speed is allowed to change as 10% less or 30% more U_r [19]).

Two main strategies might be observed in literature, that employs this instability:

- a bluff body is chosen that undergoes this instability by the effect of the self-excited motion. The induced vibrations are called VIV (Vortex Induced Vibrations);
- the vortices generated by a first bluff body are applied over a second structure that is therefore forced to oscillate. In this case the wake of the first object is responsible for the induced vibrations. The induced vibrations are in this case called WIV (Wake Induced Vibration).

The latter case is the one depicted in Figure 1.6, where it is represented the design proposed by Weinstein et al. [20]. A bluff body is placed upstream in order to determine a vortex street; the receiving structure is an appropriate cantilever beam with a piezoelectric base insert and a fin at the structure tip.

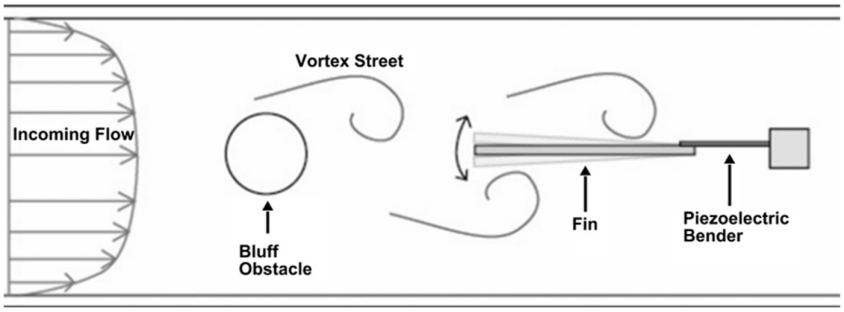

Figure 1.6 Vortex induced vibration energy harvester schema [20]

With a simple Bernoulli relation, it is possible to determine the pressure differential, which corresponds to the force exerted on the fin as:

$$\Delta p = \frac{1}{2}\rho({v_1}^2 - {v_2}^2) \tag{1.18}$$

where Δp is the difference in pressure, ρ is the density of the air and v is the velocity of the vortex with subscripts indicating side of the fin. For optimal power harvesting an energy

harvester must have a natural frequency close to the shedding frequency of the Karman vortex street, which is a strong limitation in all the situations in which the wind flow has not a constant speed. Another disadvantage is the fact that a bluff body is required, which needs additional volume for the energy scavenging application. An example of a working prototype is proposed by Weinstein et al. [20], see **Errore. L'origine riferimento non è stata trovata.**(a). The prototype confirms the limitations on the narrow range of frequencies at which the vortex shedding instability is triggered. Adjustable weights are located on the fin in order to show that the device can be tuned to work at a specific wind speed. The application of the proposed model is in fact the diagnosis of an air ventilation duct, where the wind speed profile is expected to be uniform and constant, so that there is no real application in outdoor environments.

The possibility of a bluff body that is self-excited by the vortex shedding is illustrated in the work by Zhang and Wang [21]. This solution is again a piezoelectric harvester, see **Errore. L'origine riferimento non è stata trovata.**(b), which shows the same limitation on the narrow range of working fluid speeds. The research cited also compare the results with another experimental prototype of a WIV harvester. The conclusions claim that WIV harvesters are able to produce the highest level of power, while VIV harvester have the advantage to require inferior volumes.

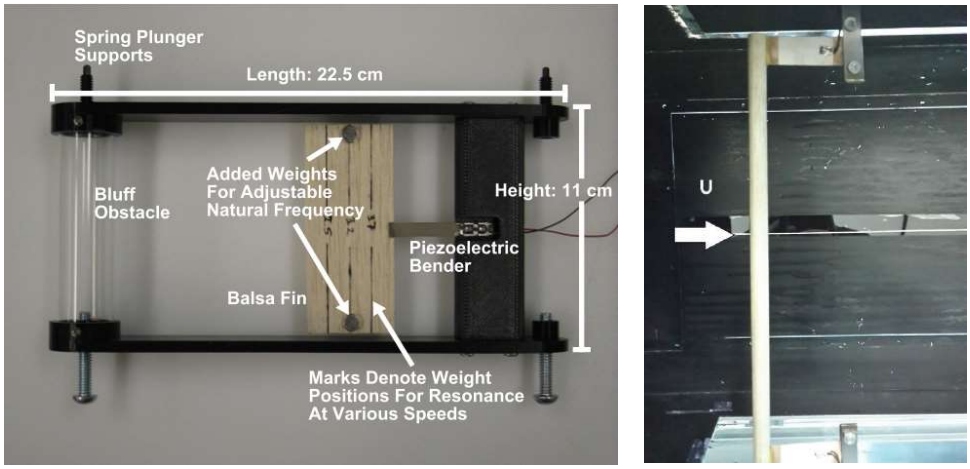

(a) (b)

Figure 1.7 (a) Prototype of a wake WIV energy harvester [20] (b) Prototype of a VIV energy harvester [21]

Flutter based energy harvesters

Flutter instability is typical found in two degrees of freedom systems, mostly for translational and rotational motions, and it is part of the static instabilities class, because it depends on the system stiffness. The instability is determined by the sign of the extra-diagonal terms of the stiffness matrix. The same effect was responsible for the Takoma Bridge collapse.

The work by Bryant and Garcia [11] has developed a "T-shaped" prototype, represented in Figure 1.8, with a wing tip body, that converts mechanical energy into electrical energy by means of a piezoelectric base transducer. The mathematical model applied by Bryant and Garcia is derived from a semi-empirical model of the non-linear electromechanical and aerodynamic system.

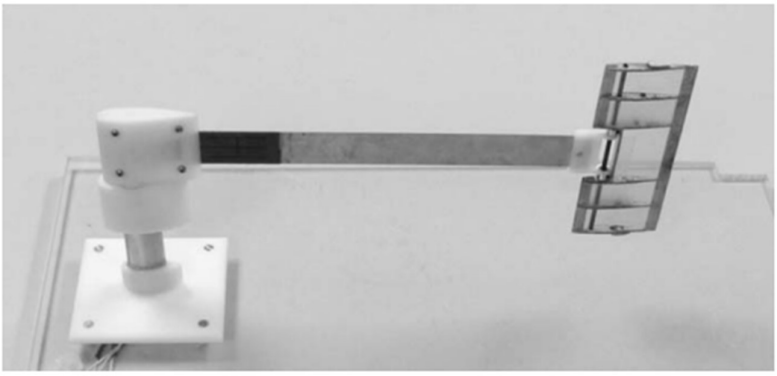

Figure 1.8 Flutter energy harvester prototype created by Bryant and Garcia [22]

The applicability of such systems is constrained by the limit of working flow speeds that enhance the instability. The device must be optimized in order to widen the range of operational speeds, and this optimization can often interfere with the need of a compact design.

Galloping-based energy harvesters

Galloping is an aeroelastic response mechanism in which the fluid-dynamic loading are resulting from the velocity of the structure motion. It is a single degree of freedom instability in which the fluid-flow forces the oscillation of a bluff body in the direction perpendicular to the flow. The instability is triggered after a certain onset speed, called the galloping onset speed, is reached. Beyond this limit the initial response of a structure undergoing becomes a divergent oscillation, which increases in amplitude and has the same frequency of the

structure involved. When the energy input by the wind is balanced by the energy absorbed by the non-dimensional damping the galloping transient results in limit cycle oscillations. The process is generally characterized by low frequency and high amplitude oscillations.

This instability has been applied to different experimental energy harvester prototypes that have a design similar to the one shown in Figure 1.9. The bluff body is located at the end of a cantilever beam that is then subjected to oscillating motion when galloping occurs. A piezoelectric material at the base of the bender accomplishes the power conversion from mechanical strain to output electrical power.

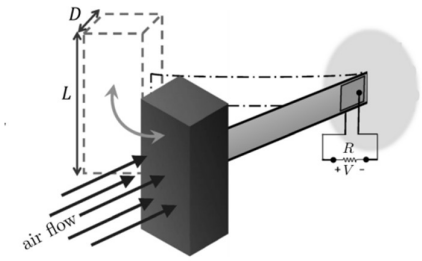

Figure 1.9 Galloping Piezoelectric Energy Harvester schema

The clear advantage of this approach for an energy harvester, is that beyond the galloping velocity the instability will always take place, guaranteeing the full efficiency of the device connected even in case of higher speeds. Even if most of the solutions proposed are based on the use of piezoceramics, an electromagnetic energy harvester from galloping vibrations was proposed by Dai et al. [23].

Wake galloping energy harvesters

In wake galloping the variation in aerodynamic loading results from changes in interference effects caused by the motion of one structure relative to another. In parallel cylinders, it was demonstrated that the presence of the wake galloping phenomenon depends on the position of the front cylinder and vibrations only occur for specified spacing distances between the two parallel cylinders as illustrated in Figure 1.10. Jung and Lee [24] proposed an electromagnetic system based on such phenomenon using two cylinders at different spacing. Like for the vortex shedding instability even this approach involves high volumes due to the presence of two bluff bodies and it also has limitations for the narrow range of fluid speed that triggers the phenomenon.

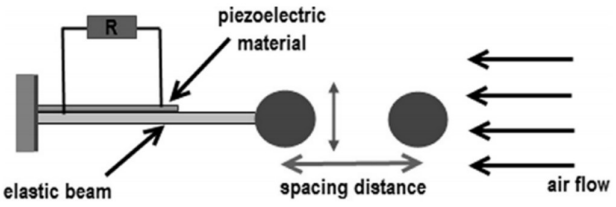

Figure 1.10 Wake galloping energy harvester configuration

Performances

All the flow induced vibration techniques described are compared in Table 1.4 by means of representative researches for each wind flow instability adopted. It is important to note at this point that the majority or researchers have developed applications with target wind speed in the range 4-11 m/s, and there are no concerns about extending the range of operation instead of maximizing the power output for a very short range of fluid velocities. It is also apparent that in every case the minimum volume required for a flow energy harvester is greater than the ones needed by other systems, but the achievable power is significant.

Phenomenon	Authors [reference]	Max average Power $[mW]$	wind speed $[m/s]$	volume $[cm^3]$	Power density $[mW/cm^3]$
cross-flow flutter	Li et al. [25]	0.6	na	na	na
flutter	Bryant and Garcia [22]	2.2	7.9	23.7	0.093
	Erturk et al. [26]	10.7	9.3	1200	0.009
	Kwon [27]	4	4	12	0.333
galloping	Sirohi and Mahadik 2011 [28]	1.14	4.7	332	0.003
	Sirohi and Mahadik 2012 [5]	53	5.2	402	0.132
	Ewere et al. [29]	13	8	196	0.066
	Zhao and Yang 2013 [30]	139	15	240	0.579
	Zhao and Yang 2015 [31]	4.5	8	40	0.113
	Zhao et al. [4]	8	8	240	0.033
	Yang et al. [32]	8.2 (square) 6 (rect 2:3) <1 (triangle) <1 (D-section)	8	240	0.034 0.025 <0.004 <0.004
VIV	Akaydin et al.	0.1	1.1	na	na
	Song et al. [33]	0.08	0.35	18.8	0.004
	Weinstein et al. [20]	5	5.5	440	0.011
	Zhang and Wang [21]	7e-7(VIV) 3e-4(WIV)	1 - 3	123 617	5.6E-9 4.8E-7
wake galloping	Akaydin et al. [34]	0.004	7.2	848	4.7E-6
	Jung and Lee [24]	370	4.5	1669	0.222
wind flow	Kan et al. [18]	na	11	35	na
	Priya [17]	7.5	4.4	na	na
	Howey et al. [16]	2.5	7	4.5	0.556

Table 1.4 Comparison between main researches held in the field of wind flow energy harvesting

1.4 Galloping Piezoelectric energy harvesters in literature

In this paragraph the concept of harvesting energy from a galloping based vibration is further developed. A more accurate description of the phenomenon is held, with the mathematical formulation of the aerodynamic force generated. The hypotheses behind the approach followed are illustrated, and other effects of fluid stream conditions are highlighted. A series of examples from the prototypes of galloping piezoelectric energy harvesters (GPEHs) realized in recent researches is given with focus on the designs proposed, the materials used, the range of operation and the harvesting capability. This comparison is aimed at making an evaluation of the possibilities explored to date, in order to understand which configuration is more suitable for the target application. Open questions left in literature works are also addressed as objectives for the present study.

1.4.1 Aerodynamic forces

First a SDOF system is considered, which is placed in an aerodynamic force field, due to the action of a homogenous and constant fluid flow. As reference to Figure 1.11 the important dimensions characterizing the system aerodynamics are:

- The system degree of freedom y which is directed orthogonal to the flow
- The absolute fluid speed U
- The angle of attack α, which is the incident direction of the wind with respect to the object surface
- The relative fluid speed V_r, which is the fluid speed relative to a point of the body
- The cross-section height D
- The cross-section width B

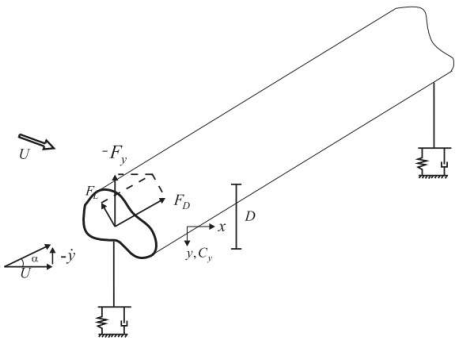

Figure 1.11 Single DOF system placed in aerodynamic field

As it is well established in aerodynamics a body hit by a bi-dimensional fluid flow is excited by the actions of aerodynamic forces that appear on the surfaces between the flow and the body itself. These forces are tangential and normal to each point of the body surface and under a global point of view they can be considered as a system of forces acting on the center of mass. Such a system is characterized by:

- the drag force F_D which has the same direction as the relative velocity;
- the lift force F_L which is normal to the first one;
- the aerodynamic moment M that is not considered in the description that follows because the system under investigation has only a single translational degree of freedom.

And they are normally represented as:

$$\begin{aligned} F_D &= \frac{1}{2}\rho C_D S {V_r}^2 \\ F_L &= \frac{1}{2}\rho C_L S {V_r}^2 \\ M &= \frac{1}{2}\rho C_M D S {V_r}^2 \end{aligned} \tag{1.19}$$

where F_D, F_L, M are the drag and lift forces and the aerodynamic moment respectively, ρ the fluid density, S the surface area hit by the flow and C_D, C_L and C_M are adimensional coefficients. The magnitude of these latter parameters depends on the fluid-body interaction, primarily as a consequence of the body shape and the incident direction of the flow.

Quasi-steady theory

The coefficients C_D, C_L and C_M are typically measured through experimental tests in which the tangential and normal forces are measured for different angles of attack α. These tests are carried out in static conditions, meaning that the forces are measured having a constant fluid flow and the body displacement being constrained. For this reason, the relations (1.19) are valid only for static flow conditions, which means that the fluid velocity relative to the body creates a constant angle through time. If the relative speed V_r changes with time, because of the motion of the body, the equations (1.19) are still valid as long as the oscillation of the body, and therefore the changes in the angle of attack, happens very slowly, in a quasi-static way. In quantitative term this condition holds true for a small value of the reduced frequency:

$$f^* = \frac{f_n}{U/D} \tag{1.20}$$

where the ratio U/D represents the frequency related to the time needed by a fluid particle to overpass the body. Therefore, for the purpose of the present application the parameters that guarantee the quasi-steady aerodynamics theory for a certain wind speed range are a small natural frequency f_n and a small cross-section width D. Another value used to describe the limit of applicability of the quasi-steady hypothesis is the adimensional reduced fluid speed:

$$U^* = \frac{U}{f_n D} \tag{1.21}$$

that is the inverse of the reduced frequency. Different values for the reduced wind speed to validate the quasi-steady theory can be found in literature from 20 to 60 [35] [36].

Influence of the fluid stream conditions

Many different factors may affect the flow in a considerable way and are listed for a qualitative comprehension of the phenomenon. These are parameters that can influence the outcome of wind tunnel tests and make hardly comparable the experimental data obtained by different teams in different facilities. At the same time these effects should be considered according the target environment that the GPEH device will be interacting to.

Effect of temperature

Temperature may affect the aerodynamic force if the environment has a significant thermal difference during the operating condition. For a 20°C temperature increase the air density may be reduced by approximately 10% affecting the aerodynamic force, which is linearly dependent upon the air density. This deterioration will at the same time affect the galloping onset speed, that will be higher for a hotter environment. Notice that other mechanical properties will be influenced by a wide temperature gap and a fully nonlinear model should be realized that account for all the possible variations. These observations may be important for outdoor implementation issues, but it is not a main concern for wind tunnel tests repeatability.

Effect of turbulence

For the effect of turbulence, it is common to refer to the work by Laneville and Parkinson [37], who showed that the latter has two main effects on the galloping instability of two dimensional rectangular cylinders:

1. It transforms cylinders with short afterbody from hard oscillators (which require a non-negligible initial transverse velocity to start vibrating) into soft oscillators.

2. It reduces the amplitudes of vibration at a given reduced wind speed. Nevertheless, for the square prism this mitigating effect is moderate and turbulence increases the tendency to interaction with Kármán-vortex resonance. By contrast, for the rectangular 2:1 cylinder turbulence both significantly reduces the vibration amplitude (up to the complete suppression of the instability for an intensity around 12.5%) and tends to decouple galloping from VIV. It was also shown that the galloping behavior is not sensitive to the length scale of turbulence (in a range comparable with the cross-section dimensions).

Effect of slenderness ratio

According to the literature known to the author it is still an open issue to clarify what is the impact of the ratio bluff body length over bluff section width (L/D) on the total aerodynamic load. It is apparent that a low ratio will affect the aerodynamic force by changing the boundary condition of the fluid stream, introducing three dimensional effects, that will lower the energy contribution of the extremities of the bluff body. It is important to note also that available researches on this topic are focused on civil engineer purposes and therefore deal with slender structures that are in most cases very different from the experimental prototypes of GPEH proposed that commonly have a slenderness ratio in the order of 3 to 6.

Note that the three-dimensional effect may be drastically reduced by means of end plates applied at the extremities of the cylinder that prevent air flowing through the ends. Ryabinin and Lyusin [38] have shown that the application of the end plates to a square cylinder with ratio $L/D = 10$ significantly changes the aerodynamic behavior. In particular, they stated that the addition of end plates has the following consequences:

- The range of angles of attack for which the sign of alpha is equal to the sign of the coefficient C_y is lowered when the stream can be considered bi-dimensional with the use of end plates
- Without disks the values of the normal component of the aerodynamic force at low angles of attack are smaller.

One can then assume that for a value of the slenderness ratio smaller than the one studied by Ryabinin and Lyusin, which is typical for a GPEH prototype, these properties are magnified and corrections on the polynomial approximation may be required on empirical basis. The main works on the determination of the approximating polynomial for the aerodynamic force estimation are based on the bi-dimensional fluid streaming hypothesis obtained with the use of end plates [39] [3] [2]. The application of end plates on a GPEH is in general not feasible due to the important inertial contributions that they would exert.

Effect of edge sharpness

Carassale et al. [40] have shown the effect that the edge sharpness has on the galloping instability by means of a prototype with perfectly sharp edges and other two with rounded edges. With reference to Figure 1.12 the edge sharpness is defined with respect to the radius r of the circumference approximating the section geometry at the corners. It is stated that:

- Rounded corner produces a reduction of the critical angle of incidence for which the flow reattaches on the lateral face exposed to the wind
- On the other side a rounded corner lowers the onset galloping speed due to a drop in the drag coefficient
- In case of the most rounded edge prototype (r/b=2/15) a strong dependence on the Reynolds number is found in turbulent flow.

Another important aspect to keep under observation is the smoothness of the bluff body surfaces, which affect the friction interaction between body and fluid. For this reason, a proper material should be used in order to guarantee this property.

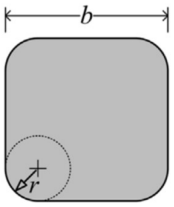

Figure 1.12 Edge sharpness representation for a square bluff body

Effect of blockage ratio

The blockage ratio, calculated here as the ratio of the cross-wind section dimension of the model to the height of the wind tunnel test should always be kept as low as possible. In fact, a high blockage causes flow speed to increase in the section near the body, thus making necessary the application of proper corrections to the measured fluid speed [41].

The blockage effect is usually considered as the sum of two contributions that are called the "solid-body blockage" and the "wake blockage".

- Solid-body blockage is a function of the volume and shape of the body: in fact, the constraint on the continuity of mass flow through the channel requires that the flow velocities near the body region are higher with respect to the undisturbed flow condition. In this case the effect is represented in Figure 1.13(a), where one can notice that the undisturbed flow velocity, indicated with the symbol V_∞, is recovered both downstream and upstream. Pressure distributions are symmetrical with a decrease in correspondence to the body region.
- The wake blockage is a function of the drag of the body and it is caused by the region of low flow velocities that extends downstream from the body, which is called the wake of the body. Considering again the continuity of fluid mass it is clear that the effective velocity after the body location increases as described in Figure 1.13(b). The pressures are distributed in a symmetric manner, with a uniform decrease in the downstream flow.

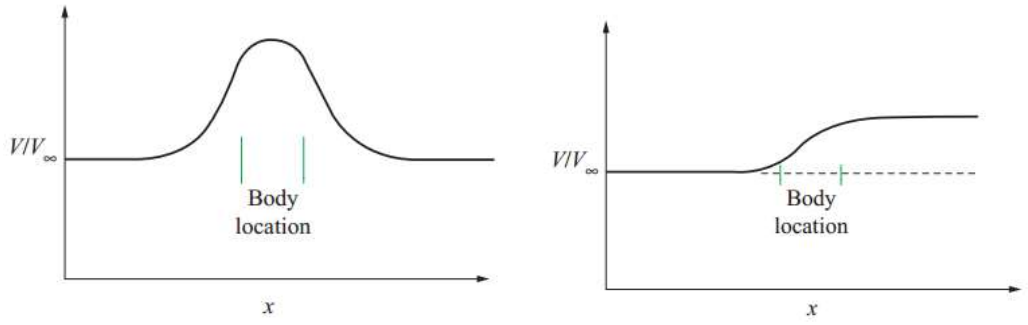

(a) (b)

Figure 1.13 Qualitative representation for (a) Solid-body blockage (b) wake blockage

As a result, the total velocity increment $\Delta V_\infty / V_\infty$ might be accessed with the method proposed by Maskell according to the ratio:

$$\frac{C_{Ff}}{C_F} = \frac{V_\infty^2}{(V_\infty + \Delta V_\infty)^2}$$

This ratio is computed as:

$$\frac{C_{Ff}}{C_F} = \frac{1}{1 + \varepsilon C_D S/A}$$

Where ε is the Maskell's blockage correction parameter, S is the cross-sectional reference area, C_D is the drag coefficient and A is the cross-sectional area of wind tunnel plane. This technique will be implemented during the experimental campaign so that the fluid velocity measured in the undisturbed flow region is corrected in order to account for the real wind speed interacting with the bluff body.

1.4.2 VIV-galloping interference effect

An important phenomenon that has been observed in many studies, but not yet completely explained is the interaction between the vortex shedding and the galloping instability. It has been verified that in most bluff bodies the lock-in frequency requires a wind velocity close to the galloping onset speed, thus creating an interference between the two effects. Both VIV at resonance and galloping act on the fundamental frequency of the system and therefore their effects can be superimposed and not easily distinguishable.

Such interaction has been classified by Mannini et al. [42] according to the following scale of interference:

1. Full interference: as in cases b2 and b3 in Figure 1.14(b) where the instability is triggered at U_r instead of U_g: this behavior represents a violation of the quasi-steady theory.
2. Partial interference: for the case b4 in Figure 1.14(b) the instability is triggered at a wind speed higher than the lock-in speed, but lower than the one predicted by the quasi-steady approach.
3. Quenching interference: for the case b1 in Figure 1.14(a) the so called quenching effect is visible: the VIV instability is able to maintain stable the system until the synchronization speed U_r is reached.
4. No interference: for high reduced wind speeds the two phenomena are supposed to arise separately at the respective onset speeds as in cases a1 and a2 in Figure 1.14(a).

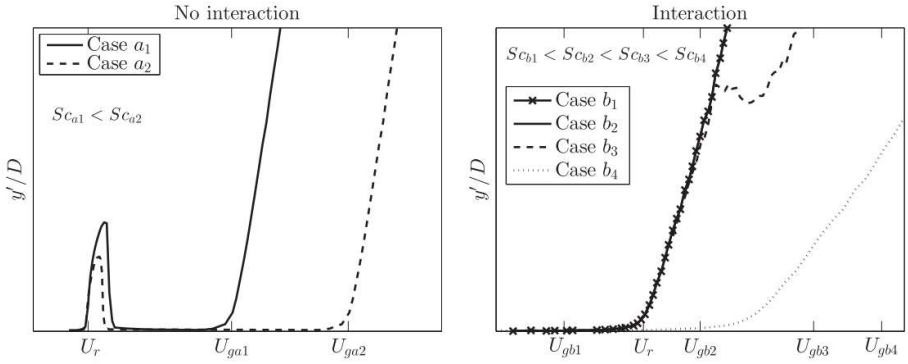

(a) (b)

Figure 1.14 VIV-galloping interaction for (a) no interaction and (b) partial-full interaction [42]

These four levels of interactions where experimentally related by Mannini et al. in a successive research [36] to the Scruton number, here introduced according to the following convention:

$$S_c = \frac{4\pi m\zeta}{\varrho L D^2} \tag{1.22}$$

where m is the mass of the GPEH, ζ its mechanical damping ratio. The onset galloping and vortex shedding wind velocities may also be easily written by including the Scruton number as:

$$U_g = \frac{2S_c}{a_1} f_n D \tag{1.23}$$

and:

$$U_r = \frac{f_n D}{S_t} \tag{1.24}$$

It is then possible to express the ratio between the galloping onset speed and the Karman-vortex resonance speed as:

$$\frac{U_g}{U_r} = \frac{2S_t}{a_1} S_c \tag{1.25}$$

where it is clear that for a specific cross-section geometry the separation between the two onset speeds is given only by the adimensional Scruton number. This value is considered of major importance in the *a priori* evaluation of the level of interference of the device under investigation; in fact, high values of $\frac{U_g}{U_r}$ guarantee that VIV and galloping are decoupled. Different thresholds are observed in literature: for example, Mannini et al. [42] found that for rectangular 2:1 cylinders a value of 4.5-8.5 is needed in order to avoid such interaction, according to Parkinson and Smith [2] instead the value is around 8.4 for the square section.

Note at this point that even if the ambition of realizing a GPEH device that shows a big enough Scruton number that decouples the VIV-galloping interaction, this is normally a task that strongly disagree with other requirements for the application. For this reason, it has not yet been possible to propose an energy harvester prototype that shows a good separation property between the two phenomena except the one proposed by Sirohi and Mahadik [5].

The behavior of such interaction for a square body has been described qualitatively by Parkinson and Wawzonek [43], who stated that such body can experience strong vibrations with amplitude increasing nearly linearly with wind speed from near U_r, if the ratio U_g/U_r is not too much greater than unity. An attempt to characterize the VIV-Galloping interaction in a quantitative way is thanks to the work by Corless and Parkinson [44]. In their research, they proposed a mathematical model for the aerodynamic resulting force, which is the algebraic sum of the galloping force model and the Hartlen-Currie model for vortex shedding. Even if the experimental results prove good accordance with the theory, it must be said that this model relies on a pair of empirical parameters that are gathered from preliminary tests on the bluff body used. For the latter reason this model is not suitable for the preliminary study of a GPEH and for the present study the only aerodynamical model implemented is the galloping model proposed by Parkinson and Smith.

1.4.3 Mathematical models for a Galloping based energy harvester

Galloping is a well-known unstable phenomenon: even if it is unlikely to happen in conventional buildings it is a problem for flexible and lightly damped structures with non-circular cross section. The first significant example in literature is related to the study of the instability that characterizes electrical lines, where the ice accretion on the wires modify the initially almost circular sections. Thereafter the attention has broadened to marine pipelines, traffic signs and gates with underflow.

The concept of energy harvesting from a galloping device is fairly new and no commercial device is yet available. Instead some authors have investigated the possibility to harvest energy from this phenomenon, in particular starting from the work by Berrero-Gil et al. [3], published in 2010. Numerical analyses have been conducted in order to compute the amount of power that can be harvested from a wind flow using piezoelectric materials [45] [29] [26] [31]. Some recent research activities are aimed at modelling and validating with wind tunnel experiments the first prototypes built [4] [5] [28].

In this section the most common mathematical models implemented by researchers are reviewed. For a more detailed explanation the reader is referred to chapter 2 of the present study.

Lumped parameter model

This approach considers the device as a mass-spring-damper system as:

$$m\ddot{y} + r\dot{y} + ky + \theta V = F \tag{1.26}$$

where the mass m is modeled in first approximation as the bluff body mass while the damping r is the structural damping and k is the effective stiffness of the structure. The degree of freedom modeled is y and it represents the displacement of the tip body in the direction transverse to the flow, where the body is oscillating. For the latter reason this method is also shortened as the SDOF (Single Degree Of Freedom) model. The external force F may be represented by means of a linearized approximation of the aerodynamic loads or with a polynomial of order 3. This mechanical equation is coupled with the piezoelectric constitutive equation simplified for the one-dimensional case with the second equation:

$$\frac{V}{R} + C_p\dot{V} - \theta\dot{y} = 0 \tag{1.27}$$

where R is the load resistance, V is the voltage across the piezoelectric patch surfaces, C_p is the capacitance of the piezoelectric material and θ is the electromechanical coupling coefficient.

This approach has a significant application in piezoelectric cantilever harvesters from base vibrations, where many authors have employed this rather simple model proving its reliability. In a study by Erturk and Inman [46] it was demonstrated that for a classic base vibration piezoelectric harvester the SDOF model needs to be corrected with a correction factor that is negligible for tip mass over beam mass ratio greater than 3-4. For what concerns galloping piezoelectric energy harvesters this model is often found in literature [47] [4]. It is important to note that this method is particularly convenient for a sensitivity analysis aimed at optimizing the geometrical design: the SDOF greatly simplify the computational effort for such a purpose. The effectiveness of this model is reduced if a longitudinal configuration is considered because the bluff body mass may not be really considered as a punctual mass at the end of the tip; another contribution must be applied to account for the mass distribution along the beam.

Coupled non-linear distributed parameter model

This method, which was theoretically applied to a GPEH for the first time by Abdelkefi [48], involves the superimposition of the vibrating modes of the structure. In this way, the analysis does not neglect the real deformation curvature of the piezoelectric patch. The vertical displacement y of a single point of the beam can be written as:

$$y(x,t) = \sum_{i=1}^{N} \phi_i(x) q_i(t) \tag{1.28}$$

where ϕ_i are the mode shapes and q_i are the modal coordinates for each mode considered, being x the longitudinal position of the point from the base of the beam. After comparing a 3-modes with a single-mode distributed model Zhao et al. [4] numerically showed that the only significant mode for the modal approach is the first one since the other modes appear at significantly higher frequencies, adding a negligible contribution. The model is then developed for the first mode using an energy approach, starting from the generalized form of Hamilton's principle for an electro-mechanical system [47] [5] [28] or from a force balance equation [49] [4] [50] [51]. It is possible to write the following system of coupled equations:

$$\begin{cases} m_1\ddot{q_1}(t) + r_1\dot{q_1}(t) + k_1 q_1(t) = F_1 \\ \dfrac{V}{R} + C_p\dot{V} - \chi\dot{q_1}(t) = 0 \end{cases} \tag{1.29}$$

Where m_1, r_1, k_1 are the modal mass, damping and stiffness parameters for the first mode and χ is the coupling term between the mechanic and electrical equations. F_1 is the first mode Lagrangian component of the aerodynamic force, which can again be considered as linear, for a first estimation of the galloping onset speed, or with a polynomial of proper order. In the latter case, it is possible to evaluate the transient and the final oscillation amplitude. The system can be solved either with a numerical method with a proper computing tool or by approximate solutions as suggested by Bibo and Daqaq [6] or Barrero-Gil et al [3]. Other authors have proposed an equivalent circuit representation to solve the non-linear problem [52]. When compared to the SDOF model the distributed model has the important advantage to consider the real deformation of the piezoelectric sheets according to the modal shape computed for the specific structure.

1.4.4 Experimental studies

This section presents the results obtained in similar experimental works found in literature. These researches are classified based on the configuration adopted for the GPEH model; the data regarding the geometrical parameters and the materials used are also illustrated. The conclusions found for these works and especially the maximum power outputs are reported in order to comprehend the advantages found. At the end of this paragraph an open issue is addressed, that is common to almost all the studies cited and that will represent an objective for the present research.

GPEH layouts

A galloping-based harvesting device is basically formed by three elements: a sustaining structure with the shape of a beam, a bluff body with specific cross section and light weight, a piezoelectric patch attached at the base of the bender. The device also need a clamping mechanism and an appropriate circuitry for the electrical power extraction, being the latter commonly limited to a simple resistive load for power consumption simulation. The PZT patches mounted are typically a pair and they are attached to the top and bottom beam surface at the base. They are commonly connected in parallel and the output voltage is dissipated on the resistive load. For a GPEH design two main strategies can be found in literature:

- the first configuration is the T-shaped design in which the bluff body is mounted on the tip of the beam in the direction orthogonal to beam axis. This category may also be divided into prototypes with a single beam terminating in the middle of the bluff body such as the one depicted in Figure 1.15(a) and devices that link the tip mass with two beams located at the extremities of the body as illustrated in Figure 1.15(b). In both cases the whole mass is located at the maximum distance from the clamping location. Note also that this first class of GPEH results in a total volume for the harvester that may be a concern for implementation in both length and width. The PZT coverage, defined as PZT length over beam length is in the order of 20-40%;
- as a second possibility, some authors have proposed a longitudinal design in which the bluff body is mounted following the beam direction. This configuration is represented in Figure 1.15(c). In this case the device has two faces that can be hit by the wind flow producing a galloping instability. Note that in this case the bluff body gives a more significant inertial contribution and that the structural stiffness is increased since a longer portion of the bender is occupied by the end body. This goes together with a compact shape of the device and a higher PZT coverage (≈80%).

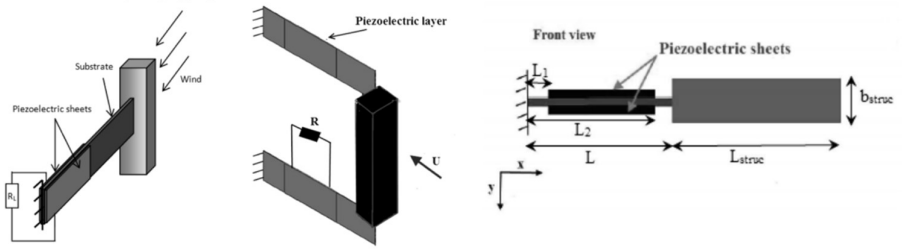

(a) (b) (c)

Figure 1.15 GPEH configurations schemas (a) "T-shaped" with single beam (b) "T-shaped" with two beams (c) longitudinal with axial bluff body

Geometrical parameters

The experimental configurations presented in literature have a total length varying from 150 to 335mm. The cross-section geometries investigated have different shapes from triangular to square and D-section and have a cross dimension in the order of 20-50mm. The bluff body length is comprised between 100 and 250mm, so that the length/width ratio is between 2-7. The most used cross section is the square one because it offers the highest power outputs and sufficiently low galloping speeds, as it has been shown also by an experimental proof by Yang et al. [32]. The tip mass is typically weighting between 1 and 60 g. All the parameters of the main prototypes described in literature are reported in Table 1.5.

author(s) [ref]	Layout	cross section	bluff length x width [mm]	beam length x width [mm]	beam thickness [mm]	Figure ref.
Sirohi and Mahadik [5]	longitudinal	D-section	235 x 30(diameter)	90 x 38	0.635	Figure 1.16 (b)
Sirohi and Mahadik [28]	T-double	Triangular (60°)	251 x 40x40	161 x 38	0.635	Figure 1.16 (d)
Ewere et al. [29]	T-single	square	100 x 50x50	228 x 40	0.4	Figure 1.16 (a)
Zhao et al. [4]	T-single	square	150 x 40x40	150 x 30	0.6	Figure 1.16 (e)
			150 x 40 x40			
			100 x 40 x40			
Zhao and Yang [31]	T-single	square	100 x 20 x20	130 x 28	0.3	Figure 1.16 (c)
Yang et al. [32]	T-single	square	150 x 40x40	150 x 30	0.6	Figure 1.16 (f)
		rectangular	150 x 40x60			
		rectangular	150 x 40x26.7			
		triangular	150 x 40(side)			
		D-section	150 x 40(diameter)			

Table 1.5 Comparison of existing GPEH prototypes

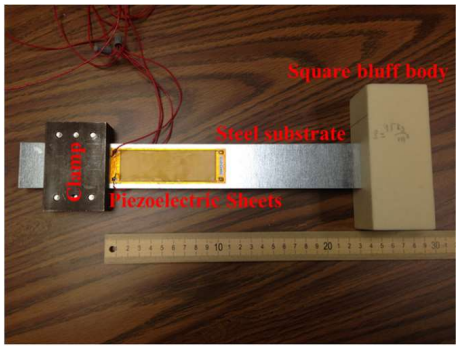

(a)

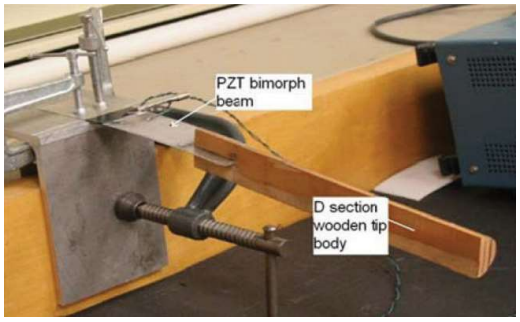

(b)

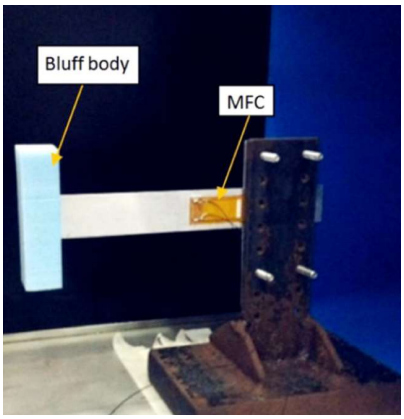

(c)

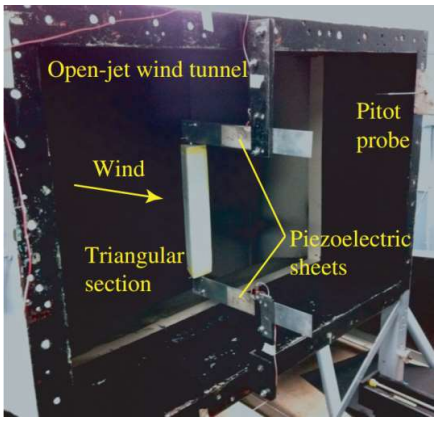

(d)

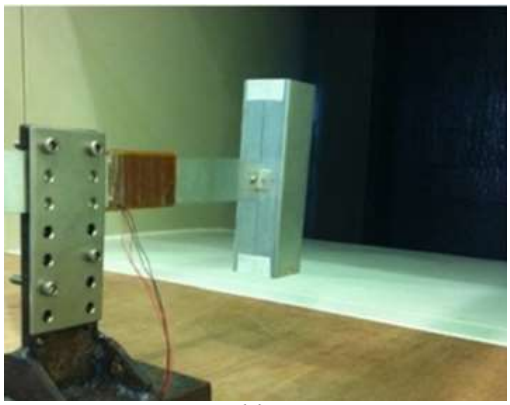

(e)

(f)

Figure 1.16 Experimental prototypes realized by: (a) Ewere et al. [29] (b) Sirohi and Mahadik [5] (c) Zhao and Yang [31] (d) Sirohi and Mahadik [28] (e) Zhao et al. [4] (f) Yang et al. [32]

Materials used

For the beam structure, the most used material is aluminum, but also steel has been successfully implemented. The bluff body is normally a very light body with small mass density: for this reason, the materials used are polyester, polyurethane foam, aluminum and wood. Many different brands have instead been used as the piezoelectric layer. To the author's knowledge no particular attention has yet been given in order to guarantee the harvester efficiency under certain indoor or outdoor conditions.

Target application

In most cases the application target is to provide sufficient power for the powering of an autonomous sensor node, see APPENDIX A.1. Commonly there are no volume constraints for the target applications, which typically is set in ventilation ducts. Such environments offer a protected scenario for the harvester and typically provide a range of flow velocity between 2 and 10 m/s. In general, the authors provide a shape optimization in order to have an acceptable galloping onset speed, which is commonly in the order of 2-5 m/s and the model validation is in general limited to a maximum wind speed of 8 m/s (except the work by Zhao and Yang [30], which reached 15 m/s).

Open issues and limits of the available researches

In every work cited, the galloping force is modeled according to the quasi-steady aerodynamic hypothesis, which assumes that the time scale of the perturbation problem is considerably slower than the one of the aerodynamic phenomenon. In particular, this is said to be valid for high values of the reduced wind speed U^* as already explained. None of the experimental work cited investigates the validity of this hypothesis, so that the galloping force modeled may be not coherent with the problem conditions. As it is reported in Table 1.6, different ranges of reduced wind speed are considered: in some cases, galloping is expected to arise at very low values. Therefore, an objective to be achieved in this research topic is the establishment of the limits beyond which the quasi-steady aerodynamic hypothesis is no longer valid.

Another common issue of the researches reviewed is that none of them takes into account the interference between vortex shedding and galloping, even if, in almost all the studies, the lock-in speed is close to the galloping onset speed. These observations are drawn by looking at Table 1.6, where the reader can see that the two-aerodynamic instability are located in a

very narrow range of frequency. The lock-in speed is computed from the declared frequency and side dimension of each prototype, while the galloping onset speed is reported as written in the papers; the experimental onset speed is the dimensional speed for which the tested prototype is found to undergo limit cycle oscillations. Note that, even if the prototype realized by Sirohi and Mahadik [5] has a ratio $\frac{U_g}{U_r} \gg 1$, no results are shown for the vortex shedding frequency range, so that it is not clear if this prototype showed an almost null interference. Therefore, it has not been explained yet if the galloping force model is to be considered valid even in case of interference with vortex-shedding, and which are the techniques to promote such separation between the two unstable phenomena.

Moreover, in the researches read, no validation is dedicated to the electromechanical model alone, but the prototypes are directly tested in wind tunnel facilities. The accuracy of the validation is then given only by the comparison between predicted and experimental power and displacement reached during a limit cycle. In such validations, where the electromechanical part is involved together with the aerodynamical part, some authors have found discrepancies between predicted and experimental results, which in one case are assumed to be dependent on possible non-linearity of the non-dimensional damping [31]. A separate validation of the electromechanical part could clearly confirm that the model applied to the study of a GPEH system is valid and that the main dynamics of the system are taken into account.

Only a few researchers have investigated the effects of a real power acquisition system connected to the GPEH [5], while most of the prototypes were simply connected to resistive loads to simulate an electrical power dissipation. This is still the obstacle that prevents galloping harvesters to be implemented in real applications.

	Ewere et al. [29]	**Zhao and Yang [31]**	**Sirohi and Mahadik 2011 [28]**	**Sirohi and Mahadik 2012 [5]**	**Zhao et al. [4]**	**Yang et al. [32]**
Strouhal speed [m/s]	1.23	2.73	4.00	0.60	2.24	2.24
Predicted galloping onset speed [m/s]	1.97	1.50	3.40	2.50	1.62	3.45
Experimental onset speed [m/s]	2.00	3.00	3.58	2.46	2.50	2.50
Reduced speed in the range of fluid velocities investigated	13-52	9-48	8-15	19-80	9-29	9-29
Frequency [Hz]	3.0	16.6	8.0	4.0	6.8	6.8

Table 1.6 Comparison of Strouhal and Galloping numerical speeds with respect to the experimental onset speed

2 ANALITICAL MODEL OF A GPEH

This chapter is aimed at the development of two different analytical models for a galloping piezoelectric energy harvester, whose reference configuration is shown in the first part. The lumped and distributed parameter models are considered with reference to other researches, that where proved to model the electro-mechanical coupling and to accurately describe the galloping force. Before introducing these two models, an introduction follows with a complete explanation of the piezoelectric effect and of the galloping model adopted. Final objective of the chapter is to conclude which model is more suitable to describe the properties of the system.

2.1 GPEH reference layout

For the ease of use in the application considered the design to be preferred is the longitudinal one. This layout in fact consists of a less voluminous body with the advantage that it can be mounted to harvest energy from two opposite directions of wind flow. No analytical comparison between the T-shaped and longitudinal configurations has yet been made for what concern the power capability, but the experiment by Sirohi and Mahadik [5] showed a relevant power/volume ratio for this configuration.

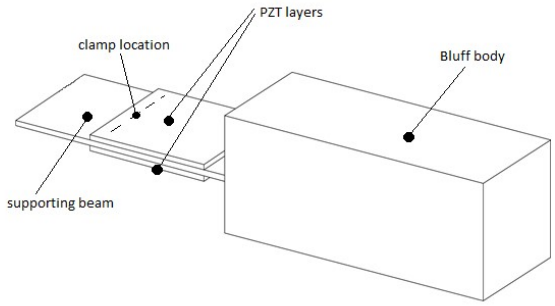

Figure 2.1 GPEH layout for a longitudinal configuration with two unimorph layers

The layout considered is the longitudinal GPEH with certain characteristics that make the case dealt with in this section a general case, from which all the prototypes described in the following can be modeled. In particular, as depicted in Figure 2.1, a supporting beam structure is considered with two PZT patches attached at each side and a bluff body attached to the beam free end. An extension is applied to the bluff body with a potentially different material. The purpose of this last region is also that it is meant to account for the effect of an added mass to the tip, which may account for a measuring system tool placed on the tip or for a lumped mass added on the end of the body. The origin of the fixed reference is placed on the clamped end of the beam with the X axis positioned along the longitudinal direction of the device, the Y axis being the oscillation direction (positive upwards). In order to simplify the following formulation, the variables used are defined in Table 2.1. Notice that the piezoelectric elements can be connected in series or in parallel, thus achieving different performance that are considered in the model.

$X_{i,j}$	For the quantity named 'X' the first subscript indicates the material used ("p": piezoelectric layer, "s": supporting beam, "b": bluff body, "e": extension for the bluff body). The second subscript, if present, indicates the region in which the quantity "X" is considered
$\phi_j^{(i)}$	i-th mode of vibration for the region j
$V_{i,j}$	Volume of the material i for the region j
w_i	Width of layer i
ρ_i	Density of layer i
t_i	Thickness of layer i
m_i	Mass per unit length of layer i

c_i	Young modulus of layer i
S_i	Strain of layer i
L_j	Length of the region j
d_i	Distance of the layer i from the neutral axis of the region j
D	Side width of the bluff body

Table 2.1 List of variables used in the modal approach

Note that for the sake of simplicity, even if the piezoelectric devices commercially available are made of different substrates, in this case the model is composed of two PZT layers that cover the entire element volume. In the real program written for numerical integration all the layers will be considered in a similar way to the one proposed in the following for the beam.

2.2 Piezoelectric beam model

For the considered GPEH device a unimorph piezoelectric patch is modeled, which consists of a single piezoelectric layer combined with different substrate layers that guarantee good elastic properties for the overall package. In the final prototype this piezoelectric device is attached to one or both sides of a supporting beam that is clamped at one end to a fixed support in a cantilever configuration. The general case study considered in the following is the configuration of a central supporting beam with a unimorph attached on each side.

2.2.1 Characteristics equations

When the beam considered undergoes bending, stress and strain for each layer vary according to the direction of the given bending moment. In Figure 2.2 it is depicted how fibers of the layers above the neutral axis are in traction, while the ones below are in compression.

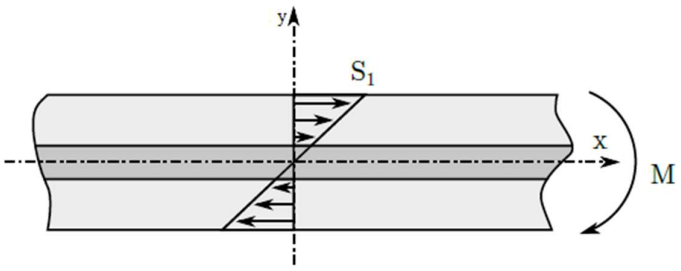

Figure 2.2 Convention for the positive direction of stress, strain and bending moment for a beam made of 2 PZT layers attached to a metal layer

According to the direct piezoelectric effect a piezoelectric layer produces charge when mechanically strained. This particular property is used in order to transform the mechanical energy from the bending of the beam induced by galloping to the suitable electric energy for the application. This process is described by the following constitutive equations for piezoelectric materials:

$$S_{ij} = s^E_{ij-kl} T_{kl} + d_{k-ij} E_k \tag{2.1}$$

$$D_i = d_{i-kl} T_{kl} + \varepsilon^T_{ik} E_k \tag{2.2}$$

where the mechanical strain S and stress T tensors are introduced, as well as the electric displacement D and the electric field E (the spatial directions are represented with the subscripts *i, j, k, l*). The other coefficients are the mechanical compliance at constant electric field s^E_{ijkl}, the permittivity at constant stress ε^T_{ik} and the coupling matrix d_{kij}. The latter is a 3x6 matrix made up of the deformation piezoelectric coefficients: note that without this term equations (2.1) (2.2) are respectively the Hooke's and Gauss' laws.

For the application under study the piezoelectric material is operating in the so called 3-1 mode, meaning that the deformation is applied along the direction 1, while the voltage is harvested along direction 3. In this case the couple of equations (2.1) (2.2) can be simplified as follows:

$$S_1 = s^E_{11} T_1 + d_{31} E_3 \tag{2.3}$$

$$D_3 = d_{31} T_1 + \varepsilon^T_{33} E_3 \tag{2.4}$$

The constitutive equations are then commonly rearranged in matrix form as:

$$\begin{bmatrix} S_1 \\ D_3 \end{bmatrix} = \begin{bmatrix} s^E_{11} & d_{31} \\ d_{31} & \varepsilon^T_{33} \end{bmatrix} \begin{bmatrix} T_1 \\ E_3 \end{bmatrix} \tag{2.5}$$

Note that the output current is related to the type of connection of the two unimorph present on the beam, that can be linked in series or in parallel.

2.2.2 Temperature influence

It has been demonstrated in the literature that the properties of a piezoelectric material are influenced by the environment temperature. In particular, for a PZT-5H layer Hooker [53] has measured an increase of about 200% in the piezoelectric constant d_{31} for a temperature variation in the range -70/120°C; an increase of 300% for the dielectric constant ε_{33}^{T} for the same variation interval and a decrease of the piezoelectric Young's modulus of about 30% from -20 to 50°C.

In a more recent work by Abdelkefi et al. [54] the temperature dependency is considered in a nonlinear-distributed parameter model of a GPEH: numerical results show that the output power, the limit cycle oscillations and the galloping critical speeds are modified according to the temperature level (considered in the range -20/60°C). It is determined that the effects of varying the operating temperature are more significant at specific load resistances and wind speeds and that more energy can be harvested at high wind speeds for a low temperature. In order to guarantee the efficiency of a GPEH in case the range of operating temperature is wide (i.e. outdoor applications) an analysis must be conducted at different temperature levels, so that a final optimization can be considered based on the worst case found.

2.3 Galloping force model

The GPEH system may be seen as a single degree of freedom oscillating body with a concentrated mass, which represents the bluff body and the contribution of the structure weight, a spring and damper that represent the structural stiffness and damping capability. A flow is assumed with constant and homogenous fluid characteristics, that hits the side surface of the body with a normal direction. In Figure 2.3 it is illustrated a rectangular-section bluff body subjected to the described condition, where the relative fluid speed is derived from the vectorial sum of the fluid velocity and the body speed with respect to a fixed frame.

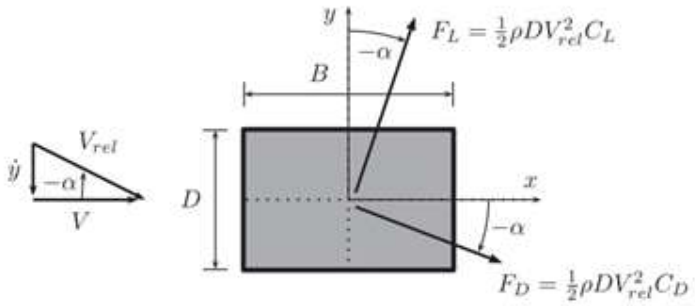

Figure 2.3 Side-view of the aerodynamic force per unit length acting on a rectangular-section bluff body

The total aerodynamic load results in a contribution along the vertical direction y for the system equal to:

$$F_y = F_L \cos\alpha - F_D \sin\alpha \tag{2.6}$$

where $\alpha = \tan^{-1}\left(\frac{\dot{y}}{U}\right)$.

For small enough variations of the angle of attack α around zero value and under the quasi-steady aerodynamic hypothesis, the following simplifications can be written:

- The relative fluid speed can be approximated as $V_r = \sqrt{U^2 + \dot{y}^2} \approx U^2$
- The angle of attack may be simplified as $\alpha \approx \left(\frac{\dot{y}}{U}\right)$
- It is possible to use a first-degree Maclaurin approximation for the sine and cosine function as: $\cos\alpha \approx 1$ and $\sin\alpha \approx \alpha$
- Since the aerodynamic coefficients depend upon the angle of attack they can be expanded according to Taylor's formula as:

$$C_L = C_L|_{\alpha=0} + \left.\frac{\partial C_L}{\partial \alpha}\right|_{\alpha=0} \alpha \tag{2.7}$$

$$C_D = C_D|_{\alpha=0} + \left.\frac{\partial C_D}{\partial \alpha}\right|_{\alpha=0} \alpha \tag{2.8}$$

Furthermore, it can be observed that for a bluff body the lift coefficient is equal to zero for null angle of attack and that the drag coefficient curve presents a minimum for $\alpha = 0$, meaning that its derivative is null in the origin. As a significant example the same

conclusions can be drawn from Figure 2.4, where the lift and drag coefficients are reported for an equilateral triangle bluff body subjected to different incident wind flow (as it is a symmetric cross section the coefficients have a symmetric dependence on the angle of attack). Eventually the aerodynamic force for a bluff body of length L moving with a homogenous speed along the y direction can be written as:

$$F_y = \frac{1}{2}\rho DLU^2(\mathrm{C}_L\cos\alpha - C_D\sin\alpha) \tag{2.9}$$

This expression is in general written as:

$$F_y = \frac{1}{2}\rho DLU^2 C_y \tag{2.10}$$

being C_y the aerodynamic force coefficient acting on the vertical component. By performing the aforementioned simplifications, it is obtained:

$$F_y = \frac{1}{2}\rho DLU^2\left(\left.\frac{\partial C_L}{\partial\alpha}\right|_{\alpha=0} - C_D|_{\alpha=0}\right)\frac{\dot{y}}{U} \tag{2.11}$$

Note in particular that this linearized expression for the aerodynamic force can be conveniently expressed as an equivalent damping action, since the aerodynamic force is proportional to the body speed. The equivalent aerodynamic damping value, once moved on the same side of the structural damping term, is:

$$r_{aero} = -\frac{1}{2}\rho DLU\left(\left.\frac{\partial C_L}{\partial\alpha}\right|_{\alpha=0} - C_D|_{\alpha=0}\right) \tag{2.12}$$

This contribution may also assume negative values and if this is the case the pair of complex conjugate poles that represent the solution of the motion equation are moved on the right-hand side of the imaginary plane. The equilibrium of the system will then be unstable and an initial perturbation will cause the system to undergo increasing amplitude oscillations. It is possible to evaluate if a particular aerodynamic system is subject to the galloping instability with the property known as the Den Hartog criterion [1]. In fact, for a small structural damping the condition for galloping to occur is:

$$-\left(\left.\frac{\partial C_L}{\partial\alpha}\right|_{\alpha=0} - C_D|_{\alpha=0}\right) < 0 \tag{2.13}$$

which basically means that the aerodynamic damping is negative. This property is determined only by the cross-section geometry and the angle of attack. If a system with a certain structural damping r_{mech} is considered the condition that triggers the instability is

defined beyond a specific wind speed. In fact, the condition to be applied is that the total damping acting on the system is negative, which can be written as:

$$r_{aero} + r_{mech} < 0 \tag{2.14}$$

By substituting the expression for the aerodynamic damping, the result can be express in terms of the fluid speed as:

$$U > \frac{r_{mech}}{-\frac{1}{2}\rho DL\left(\frac{\partial C_L}{\partial \alpha}\Big|_{\alpha=0} - C_D|_{\alpha=0}\right)} \tag{2.15}$$

As a final remark note that the expression of the force shown in this paragraph is referred to a galloping structure where the transverse oscillation of the bluff body is interested by the same speeds in the z-direction, which is normally a good approximation for a "T-shape" GPEH design. If instead the force is applied to a bluff body that has a non-uniform transverse speed profile the total force acting on the bluff body results from an integration of the forces per unit length acting on the body. In fact, the difference in relative speed causes also a different angle of attack and therefore a different aerodynamic load, which is the case of the longitudinal GPEH design.

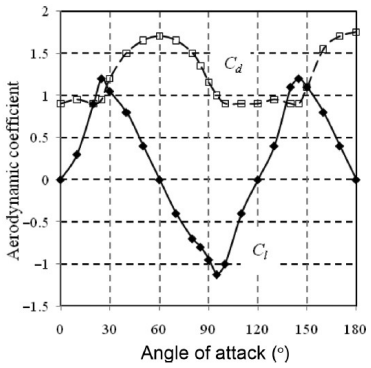

Figure 2.4 Equilateral triangle: C-lift and C-drag plots for a D-section for different angles of attack α [55]

2.3.1 Reynold's number influence

If instead it is important to evaluate the non-linear behavior of the system, the above expression for the force must be expanded to higher degrees. In this case the expansion must account for the dependence of the coefficients C_L and C_D upon the Reynolds number that is here introduced:

$$Re = \frac{\rho\, U\, D}{\mu} \tag{2.16}$$

where μ is the fluid viscosity and the Reynolds number is used to classify the flow regime as turbulent or laminar depending on its value.

The aerodynamic coefficient takes then the following form when interpolated with a higher order polynomial in tan(∝):

$$C_y = \sum_{i=1}^{N} a_i \left(\frac{\dot{y}}{U}\right)^i \tag{2.17}$$

where the coefficients a_i are conveniently estimated from static experiments and C_y accounts for the total effect of the drag and lift forces in the direction normal to the flow. Note that $a_1 = \frac{\partial C_L}{\partial \alpha}\Big|_{\alpha=0} - C_D|_{\alpha=0}$ since it is the first order expansion already computed. This approximation was first proposed by Parkinson and Smith [2], who have experimentally validated a seventh order model for a square cylinder that showed great agreement with the quasi-steady theory for sufficiently high values of reduced wind speeds and for a maximum value of the angle of incidence of 20°. The seventh-order polynomial approximation does also explain the hysteretic jump that is found in the steady state amplitude oscillations.

According to the work by Barrero-Gil et al. [39] a seventh order polynomial is required for a correct description of the phenomena for Reynolds number below 200. In this case the authors shown an analytical expression of the terms a_i as a function of the Reynolds number and proved by numerical evidence that a GPEH device is feasible even in such wind flow conditions. Note that only odd terms of a_i appear in the formulation when the bluff body is symmetric. In a later research [3] the authors have also shown that at sufficiently high Reynolds the galloping force can be approximated by a cubic polynomial expansion of $\left(\frac{\dot{y}}{U}\right)$ with the coefficients being independent of the Reynolds number as follows:

$$F_y = \frac{1}{2}\,\rho\, U^2 D \left[a_1 \frac{\dot{y}}{U} + a_3 \left(\frac{\dot{y}}{U}\right)^3\right] \tag{2.18}$$

This is the final expression of the external force per unit length acting on the system.

In Figure Figure 2.5 it is possible to have a comparison of the C_y coefficient approximation for a bi-dimensional square cylinder studied in different works [3] [38] [2], where it is important to retrieve from the picture the main constraint introduced by the third order approximation in terms of the maximum angle of incidence allowed. In fact, for sufficiently

high angles of attack ($\propto > 5$) it is apparent that the third order approximation is no longer reliable and the real behavior of the galloping system will not be accurately represented. According to the experimental results shown by Barrero-Gil et al. [3] the square cross-section presents the narrowest range of angles of attack for the validity of a third order approximation: therefore, particular attention must be placed on obtaining a sufficiently low angle of incidence. Other cross-sections such as the D-profile shows instead a more reliable matching of the approximation even for critical incidence angles. Another observation gathered from the graph is that there is a drop of the aerodynamic force beyond a critical incidence angle: from this value of α the lower shear layer of the fluid reattaches to the body and the Cy slope becomes negative.

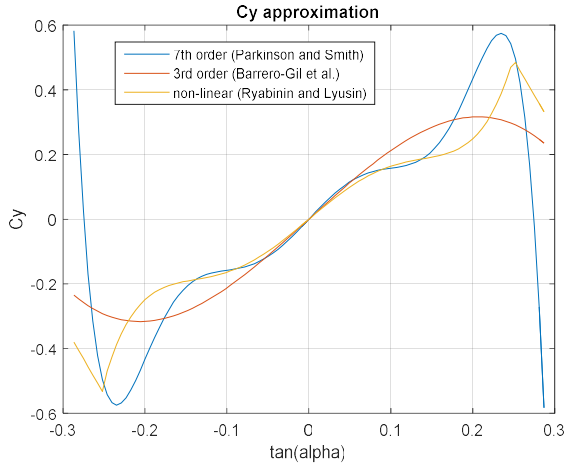

Figure 2.5 Aerodynamic coefficient approximation for a square bluff body in different works

2.3.2 Influence of the cross-section geometry

The coefficients a_1 and a_3 are experimentally evaluated for the cross-section geometry of the bluff body implemented. The most common profiles used in wind energy harvesting applications are listed in Table 2.2 for an orthogonal wind incidence angle. It is important to underline that these coefficients are no longer a valid approximation if the angle of attack changes dramatically with respect to the reference range and that their values are to be related to the flow conditions, such as turbulence and blockage ratio. These values are in fact not univocal and many different experiments have shown that there is a significant dispersion of the estimates.

Cross-section	a_1	a_3	Re	Source
Square	2.3	-18	33 000 - 66 000	Parkinson and Smith [2]
Isosceles triangle (delta=30°)	2.9	-6.2	10^5	Alonso and Meseguer [55]
D-section	0.79	-0.19	10^5	Novak and Tanaka [56]
Isosceles triangle (delta=53°)	1.9	6.7	10^4	Luo et al. [57]

Table 2.2 Aerodynamic coefficients for different bluff body cross-section geometries

2.3.3 Limits of application

This paragraph has introduced many different hypothesis behind the galloping force model adopted. In particular, the validity of the model described is guaranteed if the values of the geometrical parameters follow this series of indications:

- the ratio L/D should be sufficiently high in order to lower the three-dimensional effects on the top and bottom area of the bluff body;
- the natural frequency of the device should not be high in order to avoid that, for a certain level of oscillation amplitude of the cylinder, the angle of incidence is bigger than the region for which the polynomial approximation for C_y is valid;
- the bluff body should present perfectly sharp edges and a precise cross section geometry with smooth surfaces;
- the prototype design should account for the interaction with the vortex-induced-vibrations and in order for the galloping force model to be valid the range of fluid velocities considered should be far from the lock-in wind speed.
- the wind tunnel facility used for validation purposes should have a low turbulence and low blockage ratio;
- the Reynolds number should be comparable to the one declared in the reference work for the force approximation.

2.4 Analytical models of a GPEH

Two different models are illustrated in the following, that describes how it is possible to describe the coupling mechanism between the mechanical vibration and the electric conversion together with the galloping force.

2.4.1 Lumped parameter model

A first approach used to describe the GPEH is the single degree of freedom lumped parameter model, where the bluff body oscillations are considered as the ones of a simple oscillator as the one depicted in Figure 2.6. For this reason, the system is composed of the mass-spring-damper equation, cited in the first chapter, subject to the aerodynamic load as follows:

$$m\ddot{y} + r_{m\_el}\dot{y} + ky = F_{aero} \tag{2.19}$$

where the term r_{m_el} accounts for both the mechanical system damping and the electrical coupling with the piezoelectric element and the only degree of freedom represent the amplitude of oscillation at the tip of the bluff body. If the aerodynamic force F_{aero} is then written with just the first order approximate contribution it can be substituted with the corresponding aerodynamic damping, following the procedure explained in the previous section, thus obtaining:

$$m\ddot{y} + \left(r_{m\_el} - r_{aero}\right)\dot{y} + ky = 0 \tag{2.20}$$

The system equation has the well-known solution with natural frequency:

$$\omega_0 = \sqrt{\frac{k}{m}} \tag{2.21}$$

And the electro-mechanical damping:

$$r_{m\_el} = 2hm\omega_0 \tag{2.22}$$

where k, m, h are the equivalent stiffness, mass and non-dimensional damping for the system.

This simplified model can be very useful for an estimation of the galloping critical speed. In fact, the necessary condition for having an unstable system by means of a positive overall damping is satisfied when

$$r_{m\_el} + r_{aero} < 0 \tag{2.23}$$

which is obtained when

$$U > \frac{4h\sqrt{m}\sqrt{k}}{\rho_{aria} a_1 DL} \tag{2.24}$$

and the minimum wind speed for which the expression is valid is the onset speed U_g. Note also that if the bluff body is made of a homogenous material the expression can also be written as

$$U > \frac{4h\sqrt{\rho_{bluff}}\sqrt{k}}{\rho_{aria} a_1 L} \tag{2.25}$$

where ρ_{bluff} is the bluff body density and one can observe that the dependency of the galloping speed upon the cross-section width is eliminated.

Note that in the literature it is also present a more realistic SDOF lumped parameter model, where a second equation is introduced, derived from the piezoelectric constitutive equation. Referring to the work by Zhao et al. [4] the complete system can be written as:

$$\begin{aligned} m\ddot{y} + r_{mech}\dot{y} + ky + \Theta \mathrm{V} &= F_{aero} \\ \frac{V}{R} + C_p\dot{V} - \Theta\dot{y} &= 0 \end{aligned} \tag{2.26}$$

where V is the voltage across the terminals, C_p is the total capacitance realized by the PZT layers, R is the resistive load attached to the terminals, r_{mec} is the non-dimensional damping and Θ is the coupling term. This model is found to be sufficiently accurate when compared to the 1-distributed parameter model [4], but its strong limitation is that the coupling term must be evaluated through experiments and therefore this model is ineffective for a preliminary design optimization.

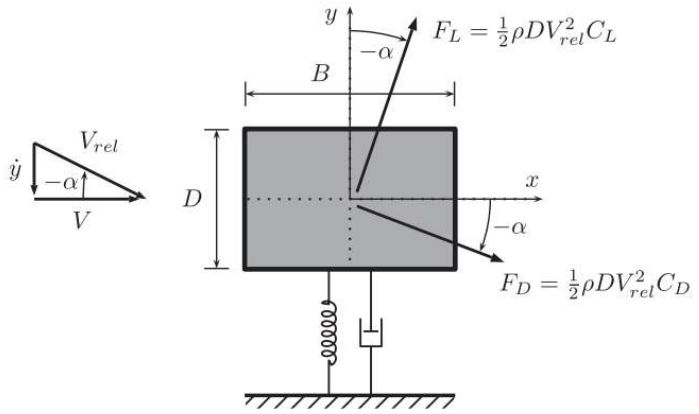

Figure 2.6 Schema of a lumped parameter galloping energy harvester

Limits of the model and observations

Despite being very simple this model has some strong limitations for its applicability:

- It is not possible to evaluate the system behavior for different load configurations: not even the variation of the galloping onset speed with respect to a different resistive load.
- The model fits well only for a GPEH where the model mass can be reduced in a single equivalent point and for this reason it should be avoided the use for the longitudinal design.
- It is not able to evaluate the system deformation in case the bluff body is made of sufficiently elastic material. In particular, it is not possible to estimate the level of electromechanical coupling, which strictly depends on the strain exerted on the PZT layer.

2.4.2 Distributed parameter model

A second approach is derived by the Hamilton's principle using the Euler-Lagrange formulation, which starts with the definition of the various energy forms. The main advantage is that it is possible to represent the system deformations, considering the finite stiffness of each layer of the GPEH, thus evaluations of the electromechanical coupling and of the natural frequency are obtained. The formulation is the same as the one presented in the works by Du Toit [15] and Preumont [14] and is given by the following integral:

$$\int_{t_1}^{t_2} \left[\delta\left(E_k - E_p + W_e\right) + \delta L_{aero} + \delta L_{el}\right] dt = 0 \tag{2.27}$$

where t_1 and t_2 are the initial and final times, E_k is the kinetic energy, E_p the elastic energy, W_e is the electrical energy, δL_{aero} is the work done by the aerodynamic force and δL_{el} is the work done by the electric charge.

Assumptions

Bending vibrations of the GPEH are descried according to the theory of continuous systems for bending beams. This approach undergoes the following hypothesis:

- A linear elastic constitutive law is considered in order to describe the relationship between stress and strain
- The section and the material properties must be constant along the same region and do not depend upon the axial position inside the beam volume.
- The beam section center of gravity lies on the principal axis in the considered plane of bending so that bending movement is decoupled from torsion.
- The "Euler-Bernoulli" theory is used to model the beam bending, which implies that the angular distortion produced in the beam by the action of shear forces is negligible, so that the following relationship can be established between the bending moment M and the transversal displacement y:

$$M = cJ\frac{\delta^2 y}{\delta x^2} \tag{2.28}$$

  where J is the geometric moment of inertia of the beam section along the principal axis orthogonal to the plane of bending and c is the Young modulus of the beam material.
- Furthermore, the "Euler-Bernoulli" theory is considered valid only for thin beams, which means beams where the total axial length is much greater than the height of the section.

Boundary conditions and stationary solutions

The design considered is made of various sections, for material properties and dimensions. Therefore, it is important to consider different regions, each of which is has constant section properties along its axial direction. The regions considered are four, as described in Figure 2.7. The purpose of the last region is to account for an added tip mass located at the end of the bluff body, or for a bluff body extension, realized with a different material.

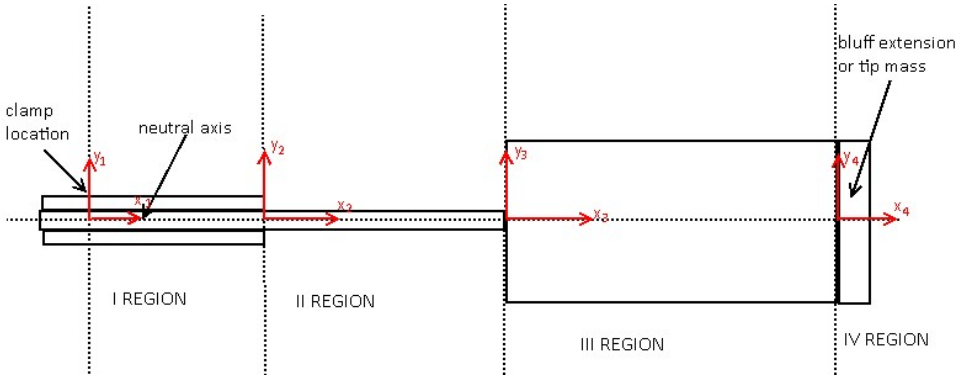

Figure 2.7 schema of the regions considered for the reference design

For the considered reference case, which has a symmetric cross section for every region, it is possible to set the neutral axis as the line of symmetry of such section. For a more general case, when the cross section is not symmetric (i.e. only one PZT layer is applied) it is possible to follow the procedure described by Du Toit [15] to obtain the neutral axis position.

When a region is made up of layers with different stiffness and density it is possible to define an equivalent inertia for the section as follows:

$$J = \frac{1}{Y_p}\sum_{i=1}^{n} Y_i\left(\frac{w_i t_i^3}{12} + w_i t_i d_i\right) \tag{2.29}$$

where the subscript i denotes a generic layer with certain thickness, width and distance from the neutral axis of the region considered, while the subscript p refers to the material which will be used as the equivalent for the inertia computation.

The modal approach considers a superimposition of an infinite number of modes of vibration: each of them is characterized by its own frequency and mode shape. The vibration of the j-th mode for the i-th region can then be written as the combination of a function of time times a function of the longitudinal displacement x as:

$$y_{ij}(x,t) = \alpha_{ij}(x)\beta_j(t) \tag{2.30}$$

where the functions α_{ij} and β_j have to following solutions for bending vibrations:

$$\alpha_{ij}(x) = A_{ij}\cos\gamma x + B_{ij}\sin\gamma x + C_{ij}\cosh\gamma x + D_{ij}\sinh\gamma x \tag{2.31}$$

$$\beta_j\,(t) = E_j\cos\omega_j t + F_j\sin\omega_j t \tag{2.32}$$

The overall displacement is then defined as the summation of the infinite modes of vibration: as:

$$y_i(x,t) = \sum_{j=1}^{\infty} \alpha_{ij}(x)\beta_j\,(t) \tag{2.33}$$

However, for the present problem it is reasonable to accept an approximation and limit the summation of infinite modes to the first n modes. Depending on the range of frequencies of interest for the problem the model may be reduced to a three-modes or even single-mode model. For a galloping energy harvester, many authors have reported experimentally that the only significant mode is the first one [30] [4] [28].

By combining the equations for the functions $\alpha_{ij}(x)$ and $\beta_j\,(t)$ each of the regions has its proper solution in the form:

$$y_1(x,t) = (A_{1n}\cos\gamma x + B_{1n}\sin\gamma x + C_{1n}\cosh\gamma x + D_{1n}\sinh\gamma x)e^{i\omega_n t} \tag{2.34}$$

$$y_2(x,t) = (A_{2n}\cos\gamma x + B_{1n}\sin\gamma x + C_{2n}\cosh\gamma x + D_{2n}\sinh\gamma x)e^{i\omega_n t} \tag{2.35}$$

$$y_3(x,t) = (A_{3n}\cos\gamma x + B_{3n}\sin\gamma x + C_{3n}\cosh\gamma x + D_{3n}\sinh\gamma x)e^{i\omega_n t} \tag{2.36}$$

$$y_4(x,t) = (A_{4n}x + B_{4n})e^{i\omega_n t} \tag{2.37}$$

The above system of equations has 14 unknowns in the variables A_{ij}, B_{ij}, C_{ij}, D_{ij} that are solved using the following boundary conditions on the equilibria of displacements and speed continuities, momentum and shear force balances between each region and considering that the first region is clamped, while the tip is a free end:

$$y_1(0,t) = 0 \tag{2.38}$$

$$\frac{\delta y_1(0,t)}{\delta x} = 0 \tag{2.39}$$

$$y_1(L_1,t) = y_2(0,t) \tag{2.40}$$

$$\frac{\delta y_1(L_1,t)}{\delta x} = \frac{\delta y_2(0,t)}{\delta x} \tag{2.41}$$

$$E_1J_1\frac{\delta^2 y_1(L_1,t)}{\delta x^2} = E_2J_2\frac{\delta^2 y_2(0,t)}{\delta x^2} \tag{2.42}$$

$$E_1J_1\frac{\delta^3 y_1(L_1,t)}{\delta x^3} = E_2J_2\frac{\delta^3 y_3(0,t)}{\delta x^3} \tag{2.43}$$

$$y_2(L_2,t) = y_3(0,t) \tag{2.44}$$

$$\frac{\delta y_2(L_2,t)}{\delta x} = \frac{\delta y_3(0,t)}{\delta x} \tag{2.45}$$

$$E_2J_2\frac{\delta^2 y_2(L_2,t)}{\delta x^2} = E_3J_3\frac{\delta^2 y_3(0,t)}{\delta x^2} \tag{2.46}$$

$$E_2J_2\frac{\delta^3 y_2(L_2,t)}{\delta x^3} = E_3J_3\frac{\delta^3 y_3(0,t)}{\delta x^3} \tag{2.47}$$

$$y_3(L_3,t) = y_4(0,t) \tag{2.48}$$

$$\frac{\delta y_3(L_3,t)}{\delta x} = \frac{\delta y_4(0,t)}{\delta x} \tag{2.49}$$

$$E_3J_3\frac{\delta^2 y_3(L_3,t)}{\delta x^2} + M_{tip}\frac{\delta^2 y_4\left(\frac{L_4}{2},t\right)}{\delta t^2} + J_{tip}\frac{\delta^3 y_4\left(\frac{L_4}{2},t\right)}{\delta t^2\delta x} = 0 \tag{2.50}$$

$$E_3J_3\frac{\delta^3 y_3(L_3,t)}{\delta x^3} - M_{tip}\frac{\delta^3 y_4\left(\frac{L_4}{2},t\right)}{\delta t^2\delta x} = 0 \tag{2.51}$$

As common practice this system is solved through numerical methods once the listed equations are arranged in the matrix H and the problem is re-stated as the following matrix equation:

$$[H]\underline{x} = \underline{0} \tag{2.52}$$

where $\underline{x}$ is defined as:

$$\underline{x} = [A_1 \quad B_1 \quad C_1 \quad D_1 \quad A_2 \quad \dots \quad D_3 \quad A_4 \quad B_4]^t \tag{2.53}$$

and the matrix H is reported in next page:

$$
H = \begin{bmatrix}
1 & 0 & 1 & 0 & 0 & 0 & 0 & 0 & 0 & 0 & 0 & 0 & 0 & 0 & 0 \\
0 & 1 & 0 & 1 & 0 & 0 & 0 & 0 & 0 & 0 & 0 & 0 & 0 & 0 & 0 \\
\cos\gamma l_1 & \sin\gamma l_1 & \cosh\gamma l_1 & \sinh\gamma l_1 & -1 & 0 & -1 & 0 & 0 & 0 & 0 & 0 & 0 & 0 & 0 \\
-\gamma_1 \sin\gamma l_1 & \gamma_1 \cos\gamma l_1 & \gamma_1 \sinh\gamma l_1 & \gamma_1 \cosh\gamma l_1 & 0 & -\gamma_2 & 0 & -\gamma_2 & 0 & 0 & 0 & 0 & 0 & 0 & 0 \\
0 & 0 & 0 & 0 & \cos\gamma l_2 & \sin\gamma l_2 & \cosh\gamma l_2 & \sinh\gamma l_2 & -1 & 0 & -1 & 0 & 0 & 0 & 0 \\
0 & 0 & 0 & 0 & -\gamma_2 \sin\gamma l_2 & \gamma_2 \cos\gamma l_2 & \gamma_2 \sinh\gamma l_2 & \gamma_2 \cosh\gamma l_2 & 0 & -\gamma_3 & 0 & -\gamma_3 & 0 & 0 & 0 \\
-EJ_1\gamma_1^2 \cos\gamma l_1 & -EJ_1\gamma_1^2 \sin\gamma l_1 & EJ_1\gamma_1^2 \cosh\gamma l_1 & EJ_1\gamma_1^2 \sinh\gamma l_1 & -EJ_2\gamma_2^2 & 0 & -EJ_2\gamma_2^2 & 0 & 0 & 0 & 0 & 0 & 0 & 0 & 0 \\
EJ_1\gamma_1^3 \sin\gamma l_1 & -EJ_1\gamma_1^3 \cos\gamma l_1 & EJ_1\gamma_1^3 \sinh\gamma l_1 & EJ_1\gamma_1^3 \cosh\gamma l_1 & 0 & EJ_2\gamma_2^3 & 0 & -EJ_2\gamma_2^3 & 0 & 0 & 0 & 0 & 0 & 0 & 0 \\
0 & 0 & 0 & 0 & -EJ_2\gamma_2^2 \cos\gamma l_2 & -EJ_2\gamma_2^2 \sin\gamma l_2 & EJ_2\gamma_2^2 \cosh\gamma l_2 & EJ_2\gamma_2^2 \sinh\gamma l_2 & EJ_3\gamma_3^2 & 0 & -EJ_3\gamma_3^2 & 0 & 0 & 0 & 0 \\
0 & 0 & 0 & 0 & EJ_2\gamma_2^3 \sin\gamma l_2 & -EJ_2\gamma_2^3 \cos\gamma l_2 & EJ_2\gamma_2^3 \sinh\gamma l_2 & EJ_2\gamma_2^3 \cosh\gamma l_2 & 0 & -EJ_3\gamma_3^3 & 0 & -EJ_3\gamma_3^3 & 0 & 0 & 0 \\
0 & 0 & 0 & 0 & 0 & 0 & 0 & 0 & \cos\gamma l_3 & \sin\gamma l_3 & \cosh\gamma l_3 & \sinh\gamma l_3 & -1 & 0 & -1 \\
0 & 0 & 0 & 0 & -EJ_3\gamma_3^2 \cos\gamma l_3 & -EJ_3\gamma_3^2 \sin\gamma l_3 & EJ_3\gamma_3^2 \cosh\gamma l_3 & EJ_3\gamma_3^2 \sinh\gamma l_3 & -\gamma_3 \sin\gamma l_3 & \gamma_3 \cos\gamma l_3 & \gamma_3 \sinh\gamma l_3 & \gamma_3 \cosh\gamma l_3 & 0 & -\omega^2 \frac{L_4}{2} M_4 & \omega^2 M_4 \\
0 & 0 & 0 & 0 & EJ_3\gamma_3^3 \sin\gamma l_3 & -EJ_3\gamma_3^3 \cos\gamma l_3 & EJ_3\gamma_3^3 \sinh\gamma l_3 & EJ_3\gamma_3^3 \cosh\gamma l_3 & -J_4\omega^2 & \omega^2 \frac{L_4}{2} M_4 & -\left(\frac{L_4}{2}\right)^2 \omega^2 M_4 & -\omega^2 \frac{L_4}{2} M_4 & \omega^2 M_4 & 0 & 0
\end{bmatrix}
$$

Kinetic Energy

The kinetic energy E_k is written as the sum of each mass contribution foreach region of the GPEH as:

$$E_k = \frac{1}{2}\int_{V_{s1}} \dot{y}_1{}^T \rho_s \dot{y}_1 dV + 2\frac{1}{2}\int_{V_{p1}} \dot{y}_1{}^T \rho_p \dot{y}_1 \, dV + \frac{1}{2}\int_{V_{s2}} \dot{y}_2{}^T \rho_s \dot{y}_2 \, dV + \int_{V_{s3}} \dot{y}_3{}^T \rho_s \dot{y}_3 \, dV + \frac{1}{2}\int_{V_{b3}} \dot{y}_3{}^T \rho_b \dot{y}_3 \, dV + \frac{1}{2}\int_{V_{e4}} \dot{y}_4{}^T \rho_e \dot{y}_4 \, dV \tag{2.54}$$

where the symmetry of the cross section is used by doubling the piezoelectric contribution. If the degree of freedom y is expressed according to the modal approach, limited to the first mode, it is possible to write:

$$\dot{y}_\iota = \phi_i{}^{(1)} \dot{q}^{(1)}, \qquad where\ \phi_i{}^{(1)} = \phi_i{}^{(1)}(x_i) \tag{2.55}$$

The notation is simplified in the following way:

$$\dot{y}_\iota = \phi_i \dot{q} \tag{2.56}$$

where the number denoting the mode considered is neglected since the following treatise will make use only of the first vibrating mode. By performing the aforementioned substitutions:

$$E_k = \frac{1}{2}\int_{V_{s1}} \dot{q}^T \phi_1{}^T \rho_s \phi_1 \dot{q} dV + \int_{V_{p1}} \dot{q}^T \phi_1{}^T \rho_p \phi_1 \dot{q} \, dV + \frac{1}{2}\int_{V_{s2}} \dot{q}^T \phi_2{}^T \rho_s \phi_2 \dot{q} \, dV + \frac{1}{2}\int_{V_{s3}} \dot{q}^T \phi_3{}^T \rho_s \phi_3 \dot{q} \, dV + \frac{1}{2}\int_{V_{b3}} \dot{q}^T \phi_3{}^T \rho_b \phi_3 \dot{q} \, dV + \frac{1}{2}\int_{V_{e4}} \dot{q}^T \phi_4{}^T \rho_e \phi_4 \dot{q} \, dV \tag{2.57}$$

Since the quantities to be integrated only depend upon the axial coordinate x it is possible to simplify the volume integrals in the following form:

$$E_k = \frac{1}{2}\left[w_s t_s \rho_s \int_0^{L_1} \phi_1{}^2 dx_1 + w_p t_p \rho_p \int_0^{L_1} \phi_1{}^2 dx_1 + w_s t_s \rho_s \int_0^{L_2} \phi_2{}^2 dx_2 + w_s t_t \rho_t \int_0^{L_3} \phi_3{}^2 dx_3 + w_b t_b \rho_b \int_0^{L_3} \phi_3{}^2 dx_3 + w_e t_e \rho_e \int_0^{L_4} \phi_4{}^2 dx_4 \right] \dot{q}^{\,2} \tag{2.58}$$

The equivalent mass M^* can be written as:

$$M^* = \left[w_t t_t \rho_t \int_0^{L_1} {\phi_1}^2 dx_1 + w_p t_p \rho_p \int_0^{L_1} {\phi_1}^2 dx_1 + w_t t_t \rho_t \int_0^{L_2} {\phi_2}^2 dx_2 + w_s t_s \rho_s \int_0^{L_3} {\phi_3}^2 dx_3 + w_b t_b \rho_b \int_0^{L_3} {\phi_3}^2 dx_3 + w_e t_e \rho_e \int_0^{L_4} {\phi_4}^2 dx_3 \right] \quad (2.59)$$

The overall kinetic energy is therefore:

$$E_k = \frac{1}{2} M^* \dot{q}^2 \quad (2.60)$$

By differentiating equation (2.60) with respect to the derivative of the modal coordinate q it is obtained:

$$\delta E_k = \delta \dot{q} M^* \dot{q} \quad (2.61)$$

Elastic Energy

The elastic energy is determined by the sum of strain and stress deformations that the GPEH experiences. For this reason, since the fourth region is not deformable it will not be included in the following definition of the total elastic energy:

$$E_p = \frac{1}{2} \int_{V_{s1}} S_{s1}^T T_{s1} dV_{s1} + \frac{1}{2} 2 \int_{V_{p1}} S_{p1}^T T_{p1} dV_{p1} + \frac{1}{2} \int_{V_{s2}} S_{s2}^T T_{s2} dV_{s2} + \frac{1}{2} \int_{V_{s3}} S_{s3}^T T_{s3} dV_{s3} + \frac{1}{2} \int_{V_{b3}} S_{b3}^T T_{b3} dV_{b3} \quad (2.62)$$

Then the formula is re-arranged by substituting the following definitions that apply respectively for stress and strain:

$$S = -z \frac{\delta^2 y}{\delta x^2} \quad (2.63)$$

$$T = cS \quad (2.64)$$

According to the piezoelectric constitutive law it is possible to state:

$$T_{p1} = c_{11}^E S_{p1} - e_{31} E_3 \quad (2.65)$$

The overall elastic energy can be split in the electrical contribution due to the piezoelectric layer and the contribution due to the other layers. The first being expressed as:

$$E_{p_{pzt}} = \int_{Vp} z^2 \left(\frac{\delta^2 y}{\delta x^2}\right)^2 c_{11}^E dV_p + \int_{Vp} z \frac{\delta^2 y}{\delta x^2} e_{31} E_3 \, dV_p \tag{2.66}$$

At this point it is important to consider the type of connection applied to the piezoelectric elements. For a series connection case the value e_{31} has opposite sign for the top and bottom PZT layers, so that the instantaneous electric fields are in the same direction with value for each layer equal to:

$$E_3 = -\frac{V_s}{2t_p} \tag{2.67}$$

where V_s is the voltage across the output terminals. For the parallel connection case, the value of e_{31} is instead the same for both the PZT patches and then the instantaneous electric fields are in the opposite directions:

$$E_{3_a} = -\frac{V_p}{t_p}, \quad E_{3_b} = \frac{V_p}{t_p} \tag{2.68}$$

where the subscript a indicates the top PZT layer and the subscript b the one at the bottom and V_p the voltage across the terminals. For the rest of the section a series connection will be considered as the default case. Considering that in equation (2.66) the quantities width of cross-section, elastic modulus and electric field are constant for any location of the volume the integrals can be further simplified as:

$$\begin{aligned} E_{p_{pzt}} = \; & w_p c_{11}^E \int_0^{L_1} \left(\frac{\delta^2 y}{\delta x^2}\right)^2 \int_{h_p}^{h_p+t_p} z^2 \, dz \, dx_1 \\ & + e_{31} \frac{V_s}{2t_p} w_p \int_0^{L_1} \frac{\delta^2 y}{\delta x^2} \int_{h_p}^{h_p+t_p} z \, dz \, dx_1 \end{aligned} \tag{2.69}$$

The integrals on the z axis are then solved:

$$\begin{aligned} E_{p_{pzt}} = \; & w_p c_{11}^E \int_0^{L_1} \left(\frac{\delta^2 y}{\delta x^2}\right)^2 \frac{1}{3}\left[\left(h_p + t_p\right)^3 - \left(h_p\right)^3\right] dx_1 \\ & + e_{31} \frac{V_s}{2t_p} w_p \int_0^{L_1} \frac{\delta^2 y}{\delta x^2} \frac{1}{2}\left[\left(h_p + t_p\right)^2 - \left(h_p\right)^2\right] dx_1 \end{aligned} \tag{2.70}$$

After solving the axial integration, it is found:

$$E_{p_{pzt}} = w_p c_{11}^E \frac{1}{3}\left[\left(h_p + t_p\right)^3 - \left(h_p\right)^3\right] \int_0^{L_1} {\phi_1}''^{(1)^2}\, dx\, q^2 + \frac{1}{2} e_{31} \frac{V_s}{2t_p} w_p \left[{t_p}^2 + 2t_p h_p\right]\left[{\phi_1}'^{(1)}(L_1) - {\phi_1}'^{(1)}(0)\right] q \tag{2.71}$$

The variable θ_s is then introduced as:

$$\theta_s = e_{31} \frac{w_p}{2}\left(t_p + 2h_p\right) \tag{2.72}$$

With an analogous procedure, the variable θ_p for the parallel connection is derived as:

$$\theta_p = 2\theta_s = 2e_{31} \frac{w_p}{2}\left(t_p + 2h_p\right) \tag{2.73}$$

By going back to the definition of elastic energy in equation (2.62) the rest of integrals are solved in a similar way:

$$\begin{aligned} E_{p_{mec}} = {} & w_{s1} c_{s1} \frac{1}{2} \int_0^{L_1} \left(\frac{\delta^2 y_1}{\delta {x_1}^2}\right)^2 \int_{-\frac{t_s}{2}}^{\frac{t_s}{2}} z^2\, dz\, dx_1 + w_{s2} c_{s2} \frac{1}{2} \int_0^{L_2} \left(\frac{\delta^2 y_2}{\delta {x_2}^2}\right)^2 \int_{-\frac{t_s}{2}}^{\frac{t_s}{2}} z^2\, dz\, dx_2 \\ & + w_{s3} c_{s3} \frac{1}{2} \int_0^{L_3} \left(\frac{\delta^2 y_3}{\delta {x_3}^2}\right)^2 \int_{-\frac{t_s}{2}}^{\frac{t_s}{2}} z^2\, dz\, dx_3 \\ & + 2 w_b c_b \frac{1}{2} \int_0^{L_3} \left(\frac{\delta^2 y_3}{\delta {x_3}^2}\right)^2 \int_{\frac{t_s}{2}}^{\frac{s}{2}+t_b} z^2\, dz\, dx_3 \end{aligned} \tag{2.74}$$

The integrals in the z-direction are solved as:

$$\begin{aligned} E_{p_{mech}} = {} & w_{s1} c_{s1} \frac{1}{2} \int_0^{L_1} \left(\frac{\delta^2 y_1}{\delta {x_1}^2}\right)^2 \left[\frac{1}{3}\left(\left(\frac{t_s}{2}\right)^3 + \left(\frac{t_s}{2}\right)^3\right)\right] dx_1 \\ & + w_{s2} c_{s2} \frac{1}{2} \int_0^{L_2} \left(\frac{\delta^2 y_2}{\delta {x_2}^2}\right)^2 \left[\frac{1}{3}\left(\left(\frac{t_s}{2}\right)^3 + \left(\frac{t_s}{2}\right)^3\right)\right] dx_2 \\ & + w_{s3} c_{s3} \frac{1}{2} \int_0^{L_3} \left(\frac{\delta^2 y_3}{\delta {x_3}^2}\right)^2 \left[\frac{1}{3}\left(\left(\frac{t_s}{2}\right)^3 + \left(\frac{t_s}{2}\right)^3\right)\right] dx_3 \\ & + 2 w_b c_b \frac{1}{2} \int_0^{L_3} \left(\frac{\delta^2 y_3}{\delta {x_3}^2}\right)^2 \left[\frac{1}{3}\left(\left(\frac{t_s}{2} + t_b\right)^3 - \left(\frac{t_s}{2}\right)^3\right)\right] dx_3 \end{aligned} \tag{2.75}$$

Constants terms are taken out of the integrals and the y-displacement is substituted according to the modal approach formulation as:

$$E_{p_{mech}} = w_{s1}c_{s1}\frac{1}{2}\left[\frac{1}{12}\ {t_s}^3\right]\int_0^{L_1}{\phi''_1}^2\,dx_1 + w_{s2}c_{s2}\frac{1}{2}\left[\frac{1}{12}\ {t_s}^3\right]\int_0^{L_2}{\phi''_2}^2\,dx_2 + w_{s3}c_{s3}\frac{1}{2}\left[\frac{1}{12}\ {t_s}^3\right]\int_0^{L_3}{\phi''_3}^2\,dx_3 + w_b c_b\frac{1}{3}\left[\left(\left(\frac{t_s}{2}+t_b\right)^3-\left(\frac{t_s}{2}\right)^3\right)\right]\int_0^{L_3}{\phi''_3}^2 \tag{2.76}$$

The overall elastic energy can then be expressed as the sum of the piezoelectric and other layers' contributions as:

$$E_p = \frac{1}{2}K^* q^2 + \frac{1}{2}\chi_s V_{el} q \tag{2.77}$$

Where the equivalent stiffness K^* is:

$$K^* = w_{s1}c_{s1}\frac{1}{2}\left[\frac{1}{12}\ {t_s}^3\right]\int_0^{L_1}{\phi''_1}^2\,dx_1 + w_{s2}c_{s2}\frac{1}{2}\left[\frac{1}{12}\ {t_s}^3\right]\int_0^{L_2}{\phi''_2}^2\,dx_2 + w_{s3}c_{s3}\frac{1}{2}\left[\frac{1}{12}\ {t_s}^3\right]\int_0^{L_3}{\phi''_3}^2\,dx_3 + w_b c_b\frac{1}{3}\left[\left(\left(\frac{t_s}{2}+t_b\right)^3 - \left(\frac{t_s}{2}\right)^3\right)\right]\int_0^{L_3}{\phi''_3}^2 w_p c_{11}^E\frac{1}{3}\left[\left(h_p+t_p\right)^3-\left(h_p\right)^3\right]\int_0^{L_1}{\phi''_1}^2\,dx\ q^2 \tag{2.78}$$

And the electromechanical coupling factor χ_s is defined as:

$$\chi_s = \theta_s[\phi_1'(L_1) - \phi_1'(0)] \tag{2.79}$$

Differentiating the elastic energy with respect to δq it is obtained:

$$\delta E_p = \frac{1}{2}\delta q K^* q + \frac{1}{2}\delta q \chi V_s + \frac{1}{2}\delta V_{el}\chi q \tag{2.80}$$

Notice that the electromechanical coupling depends upon the kind of connection the device has. For a parallel connection, the variable will assume the following expression:

$$\chi_p = \theta_p[\phi_1'(L_1) - \phi_1'(0)] = 2\chi_s \tag{2.81}$$

Charge force work

The electric energy of the two piezoelectric layers can be defined for reason of symmetry as:

$$W_e = \frac{1}{2}2\int_{Vp} E^T D\ dV \tag{2.82}$$

and

$$W_e = \int_{V_P} \left(-\frac{V_{el}}{2t_p}\right)^T \left(e_{31}S_1 - \varepsilon_{33}^S \frac{V_{el}}{st_p}\right) dV \tag{2.83}$$

By using the modal approach, it is possible to write:

$$W_e = \int_{V_p} \left(-\frac{V_{el}}{2t_p}\right)^T \left(e_{31}(-w\phi_1'' q) - \varepsilon_{33}^S \frac{V_{el}}{2t_p}\right) dV \tag{2.84}$$

Once the constant C_s is introduced as:

$$C_s = \varepsilon_{33}^S \frac{w_p L_1}{t_P} \tag{2.85}$$

equation (2.84) can be rewritten as:

$$W_e = -\frac{1}{2} V_{el}\theta q + \frac{1}{2} {V_{el}}^2 C_s \tag{2.86}$$

and then it is differentiated with respect to the system variables q and V_{el}:

$$\delta W_e = -\frac{1}{2}\delta V_{el}\theta q - \frac{1}{2}\delta q \theta V_{el} + \delta V_{el} C_s V_{el} \tag{2.87}$$

Notice that the value of C_s is again influenced by the type of electrical connection for the two PZT layers. For the parallel case connection, the value would be:

$$C_p = 2C_s = 2\varepsilon_{33}^S \frac{w_p L_1}{t_P}$$

The electric charge work can then be expressed as:

$$L_{el} = {Q_{el}}^T \delta V_{el} \tag{2.88}$$

and by differentiating the work with respect to the system variable V_{el}:

$$\delta L_{el} = {Q_{el}}^T \tag{2.89}$$

Aerodynamic force work

The aerodynamic force contribution is written as the integral of the aerodynamic loads acting on the bluff body in the third and fourth regions as:

$$\delta L_{aero} = \int_0^{L_3} F_{y3}(x)^T \delta y_3(x)\, dx_3 + \int_0^{L_4} F_{y4}(x)^T \delta y_4(x) dx_4 \tag{2.90}$$

where the displacement can be written according to the modal approach, thus obtaining:

$$\delta L_{aero} = \int_0^{L_3} F_{y3}(x)^T \phi_3\, dx_3\, \delta q + \int_0^{L_4} F_{y4}(x)^T \phi_4\ dx_4\, \delta q \tag{2.91}$$

Recalling the aerodynamic force formula presented in equation (2.18) the virtual work is:

$$\begin{aligned} \delta L_{aero} = \int_0^{L_3} \frac{1}{2}\, \rho\, U^2 D \left[a_1 \frac{\dot{y}}{U} + a_3 \left(\frac{\dot{y}}{U}\right)^3 \right]^T \phi_3\, dx_3\, \delta q \\ + \int_0^{L_4} \frac{1}{2}\, \rho\, U^2 D \left[a_1 \frac{\dot{y}}{U} + a_3 \left(\frac{\dot{y}}{U}\right)^3 \right]^T \phi_4\ dx_4\, \delta q \end{aligned} \tag{2.92}$$

The equation can be further simplified taking out the transpose since there are no vectors and by expressing again the vertical displacement in the modal form:

$$\begin{aligned} \delta L_{aero} = \frac{1}{2}\, \rho\, U^2 D \Bigg\{ \int_0^{L_3} \left[a_1 \frac{\phi_3 \dot{q}}{U} + a_3 \left(\frac{\phi_3 \dot{q}}{U}\right)^3 \right] \phi_3\, dx_3 \\ + \int_0^{L_4} \left[a_1 \frac{\phi_3 \dot{q}}{U} + a_3 \left(\frac{\phi_3 \dot{q}}{U}\right)^3 \right] \phi_4\ dx_4 \Bigg\} \delta q \end{aligned} \tag{2.93}$$

By extracting the quantities that are constant with respect to the axial directions from the integrals the following formula is obtained:

$$\begin{aligned} \delta L_{aero} = \frac{1}{2}\, \rho U D \Bigg\{ a_1 \frac{\dot{q}}{U} \int_0^{L_3} {\phi_3}^2\, dx_3 + a_3 \left(\frac{\dot{q}}{U}\right)^3 \int_0^{L_3} {\phi_3}^4 dx_3 \\ + a_1 \frac{\dot{q}}{U} \int_0^{L_4} {\phi_4}^2\, dx_4 + a_3 \left(\frac{\dot{q}}{U}\right)^3 \int_0^{L_4} {\phi_4}^4 dx_4 \Bigg\} \delta q \end{aligned} \tag{2.94}$$

The differentiation of the aerodynamic force work with respect to the variable q is:

$$\delta L_{aero} = F^* \tag{2.95}$$

where the variable F^* is defined as:

$$F^* = \frac{1}{2}\rho U D\left\{a_1\frac{\dot{q}}{U}\int_0^{L_3}{\phi_3}^2\,dx_3 + a_3\left(\frac{\dot{q}}{U}\right)^3\int_0^{L_3}{\phi_3}^4 dx_3 + a_1\frac{\dot{q}}{U}\int_0^{L_4}{\phi_4}^2\,dx_4 + a_3\left(\frac{\dot{q}}{U}\right)^3\int_0^{L_4}{\phi_4}^4 dx_4\right\} \tag{2.96}$$

Dissipative function

The dissipative energy contribution is given by a structural contribution, which can be easily gathered from an empirical proof. In the so called free decay test the system is subjected to an initial impulse that excites its response (an experimental example is shown in Figure 2.8). It is possible to write the following expression for the consequent free damped motion of the system:

$$x(t) = Xe^{-h\omega_0 t}\cos(\omega t + \varphi) \tag{2.97}$$

where X is the amplitude of motion, φ the phase contribution and h the non-dimensional damping:

$$h = \frac{r}{2m\omega_0} \tag{2.98}$$

and ω is defined as:

$$\omega = \omega_0\sqrt{1-h^2} \tag{2.99}$$

If two successive amplitude peaks $x_i(t)$ and $x_{i+1}(t+T)$ are considered, being T the period of oscillation, the logarithmic decrement is defined as:

$$\delta = ln\frac{x_i(t)}{x_{i+1}(t+T)} = ln\frac{Xe^{-h\omega_0 t}\cos(\omega t+\varphi)}{Xe^{-h\omega_0(t+T)}\cos(\omega(t+T)+\varphi)} \tag{2.100}$$

The latter brings to:

$$\delta = h\omega_0\frac{2\pi}{\omega_0\sqrt{1-h^2}} \tag{2.101}$$

Under the assumption of $h \ll 1$, it is possible to retrieve the non-dimensional damping from two consequent peaks as in:

$$h = \frac{\delta}{2\pi} \tag{2.102}$$

For a preliminary analysis on the system behavior, a non-dimensional damping can be evaluated according to the values found in similar prototypes to be in the range 1 - 1.5%.

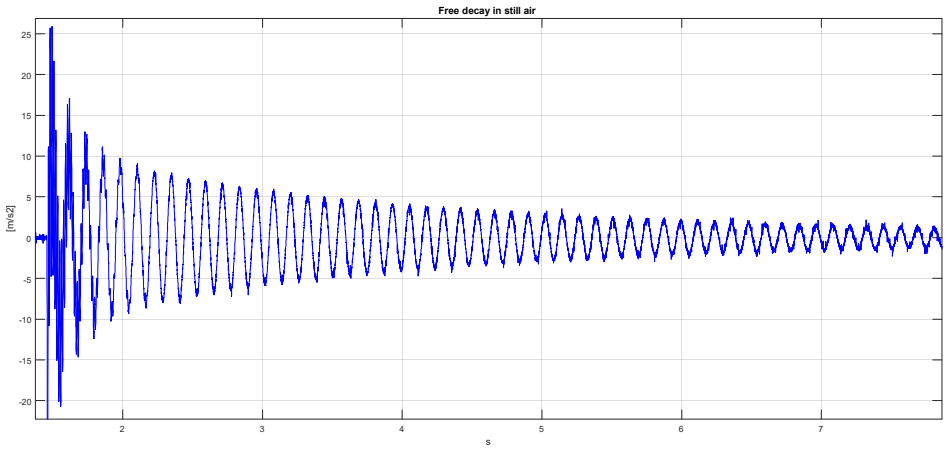

Figure 2.8 Experimental free decay acceleration response

Conclusive equations

By the application of the Hamilton principle it is then possible to write:

$$\int_{t_1}^{t2} \delta\dot{q}M^*\dot{q} - \delta qK^*q - \delta q\theta V_s - \delta V_{el}\theta V_s + \delta V_s C_p V_s + F^*\delta q + Q_{el}\delta V_s dt = 0 \tag{2.103}$$

which brings to:

$$\delta qM^*\ddot{q} + \delta qK^*q + \delta V_s\theta q + \delta q\theta V_s - \delta V_s C_p V_s - F^*\delta q - Q_{el}\delta V_s = 0 \tag{2.104}$$

It is convenient to express the system equation as the superimposition of the two system variables q and V_{el} as:

$$\begin{cases} M^*\ddot{q} + R^*\dot{q} + K^*q + \chi_s V_s = F^* \\ -C_p V_s + \chi_s q = Q_{el} \end{cases} \tag{2.105}$$

where the structural damping term R^* is introduced as described in the relative paragraph. In order to include the effect of an electrical connection the second equation is derived with respect to time obtaining the modified system:

$$\begin{cases} M^*\ddot{q} + R^*\dot{q} + K^*q + \chi_s V_s = F^* \\ -C_p\dot{V}_s + \chi_s\dot{q} = \dfrac{dQ_{el}}{dt} = i \end{cases} \tag{2.106}$$

where i is the current flowing through the electrical connection of the piezoelectric elements. This system may be combined with the equation of an electric load in order to account for the effect that the power harvesting unit has on the GPEH. As a simple example a resistive load is considered as connected to the open terminals of the piezoelectric units. In this case the third equation for the system is the first Ohm's law:

$$V = Ri \tag{2.107}$$

The system of equations (2.106) coupled with the resistive load equation (2.107) results in the following system:

$$\begin{cases} M^*\ddot{q} + R^*\dot{q} + K^*q + \chi_s V_s = F^* \\ \dfrac{V_s}{R} + C_s\dot{V}_s - \chi_s\dot{q} = 0 \end{cases} \tag{2.108}$$

The system can eventually be interpreted as a state space model by defining the following system variables:

$$\begin{bmatrix} x_1 \\ x_2 \\ x_3 \end{bmatrix} = \begin{bmatrix} q \\ \dot{q} \\ V_s \end{bmatrix} \tag{2.109}$$

The final model is obtained:

$$\begin{bmatrix} \dot{x_1} \\ \dot{x_2} \\ \dot{x_3} \end{bmatrix} = \begin{bmatrix} -\dfrac{R^* - \frac{1}{2}\rho_{aria}\, D\, Ua_1 k_1}{M^*} & -\dfrac{K^*}{M^*} & -\dfrac{\chi_s}{M^*} \\ 1 & 0 & 0 \\ \dfrac{\chi_s}{C_s} & 0 & -\dfrac{1}{C_s R} \end{bmatrix} \begin{bmatrix} x_1 \\ x_2 \\ x_3 \end{bmatrix} + \left(\frac{1}{2}\rho_{aria}\, D\, a_3 \frac{k_3}{U}\right) \begin{bmatrix} x_1 \\ 0 \\ 0 \end{bmatrix}^3 \tag{2.110}$$

Numerical simulation

The system of equation (2.110) is implemented in ©MATLAB and solved using a numerical integration method. Initial conditions must be provided with a non-zero displacement in

order to perceive the effect of a negative total damping introduced by the aerodynamics. The final limit cycle oscillation characteristics such as amplitude and frequency are obtained once it is evaluated that the transient is completed. Since the time to reach the limit cycle will differ according to any simulation parameters, the latter request is obtained by stopping the integration only when the maximum peaks in the displacement plotted over time are within a certain tolerance level.

Limits of the model and observations

This model is valid as long as the system dynamics is described by the first resonance mode, therefore a preliminary test on the prototype GPEH must establish a well-defined gap between the first two modes of vibrations. As already explained the galloping force model is a pure approximation, which validity must be checked with respect to the maximum angle of incidence. This rather complex model does not consider non-linear effects related to temperature variations or stream conditions impact or for a nonlinear damping characteristics.

3 SENSITIVITY ANALISYS AND DESIGN OPTIMIZATION

Throughout this chapter a detailed sensitivity analysis is carried out, starting from the prerequisites of the application. A series of objectives is then defined and a range of variation for each parameter is selected. The possible parameters variations are investigated with focus on the maximum power obtained for the considered range of wind speeds. As a side effect the maximum tip oscillations are observed, so that the efficiency of the conversion can be maximized, limiting the fatigue sustained by the device. The conclusions allow to design an optimized GPEH device by varying the main geometrical and electrical parameters.

3.1 Application and targets

The installation of a wireless node on a freight train considers a level of wind velocities around 15 -30 m/s. A continuous energy harvesting is required for the device, that should be able to produce enough energy for a continuous sensor diagnostic in the target wind velocity range. The total volume of the application should be compact, within a maximum length of 400 mm. A main concern for the maximum amplitude of oscillation allowable is given by the maximum strain sustainable by the piezoceramics and it must be guaranteed that for the regime wind speed the GPEH will oscillate below this critical limit. The turbulence impacting on the device will highly depend on the location in which the GPEH is placed and the placement will need an accurate evaluation before the definitive installation.

In the following simulations one parameter at a time is varied in order to decide which materials are more appropriate and which geometrical parameters should be considered. All the parameters that can be assigned in a design stage are investigated step by step and the results are compared for the target wind speed range and with a set of resistances connected

to the PZT patches. The range of variation for the parameters respects the characteristics of real materials that can be applied for the final prototype.

For the sensitivity analysis, a series of main objectives are given:

- the onset speed must be low enough to be reached by the minimum wind speed for which the node should be able to operate;
- a sufficient amount of energy should be harvested, that can guarantee full efficiency for the node in the target range of fluid speeds;
- the maximum oscillation amplitudes must be within a range that is given by geometrical constraints on the maximum volume and by the maximum strain that the piezoceramics can sustain;
- under a control perspective, the electromechanical coupling should be sufficiently high in order to control the device by varying the resistance connected.

Moreover, to be compliant with the hypothesis of the quasi-steady theory, that is adopted for the aerodynamic force model:

- the angle of incidence should not be higher than the constraint imposed by the polynomial approximation adopted;
- the reduced speeds in the operating region of fluid velocities should be high enough with respect to the quasi-steady theory;

In order to evaluate the overall performance of each case considered in this chapter, there will be made reference to the following figures:

- a graph representing the onset velocities plotted over the resistance range for the different variation over the parameter under investigation. This graph helps understanding the minimum and maximum onset speeds and therefore it indicates whether the target onset is reached. This graph may also be represented in terms of reduced wind speed so to make clear the separation between VIV and galloping;
- the root-mean-square power comparison between the different variations is instead plotted over a set of wind speeds for a specific value of resistive load and for a set of resistances for a wind speed of interest, giving a quantitative view of the optimal power case. Each point in this graph represents the property of the LCO obtained at the end of an accurate integration of the solution up to an almost steady value;
- at the same time, two similar graphs describe the maximum tip displacements reached during the LCO for the same wind speed and for the same resistance.

Furthermore, a set of parameters is grouped into a table for each of the variations performed that indicates the increase or decrease of the following quantities with respect to the base case:

- the first resonance frequency, which determines a higher reduced velocity for low value and vice versa;
- the electromechanical coupling which describes the amount of gathered energy for a certain LCO amplitude;
- the minimum onset speed for galloping computed over a full range of resistance values;
- the ratio between Vg and Vr, which is an indicator of the Scruton number and therefore illustrate how strong the interaction between lock-in and galloping is expected to be sufficiently high.

As a complementary parameter, the efficiency of conversion η is introduced as the ratio of power extracted from the flow by the oscillating body over the total power in the flow:

$$\eta = \frac{P_{el}}{P_{flow}} \tag{3.1}$$

In particular, P_{flow} is computed according to the definition given by Barrero-Gil et al. [3] as:

$$P_{flow} = \frac{1}{2}\rho U^3 D L_b \tag{3.2}$$

where L_b is the bluff body length. For P_{body} instead it is possible to consider the rms output power produced by the GPEH on the resistance connected to the device as:

$$P_{el} = \frac{1}{T}\int_0^T \frac{V_{el_{rms}}^2}{R} dt \tag{3.3}$$

The efficiency that is shown for each parameter variation is the highest obtained among all the resistances simulated for the wind speed range considered.

3.2 Reference case

A reference case GPEH is chosen using a reasonable set of characteristics that are listed in Table 3.1. For the clamp locations, the reader is referred to APPENDIX B.1. The results shown for this case are compared with the ones obtained by changing the value of one

parameter at a time. The range of variations for each parameter considered is shown in the third column of the same table. The geometrical parameters are varied according to the considered application (see section 3.1). The environment conditions are assumed as the one of a laboratory test with room temperature and low turbulence, having a uniform flow orthogonally incident with respect to the body. The geometrical design adopted is shown in Figure 3.1, where the parameters varied along the sensitivity analysis are reported for the sake of clarity.

PARAMETER VARIATIONS		**Reference case**	**Range of variations**
Piezo product	-	PPA1011	PPA1001-PPA1011
N° of piezo element	-	2	2
Clamp position	-	"clamp 0"	"clamp -6" "clamp 0" "clamp +6"
Connection		parallel	series - parallel
Cross section	-	square	triangular (30°) triangular (53°) square D-section
Non-dimensional damping (h)	%	1	0.5 - 2
Bluff body side dimension (D)	mm	40	20-60
Bluff body length (L_3)	mm	100	75 - 150
Bluff body density (ρ_b)	Kg/m^3	100	30 - 200
Bluff body extension	-	none	none
Beam thickness (t_s)	mm	0.5	0.3 – 0.7
Beam width (w_s)	mm	28	28 - 40
Second region length (L_2)	mm	25	0.1 - 40
Beam material	-	Steel	Aluminum Steel

Table 3.1 Parameters of the base case GPEH

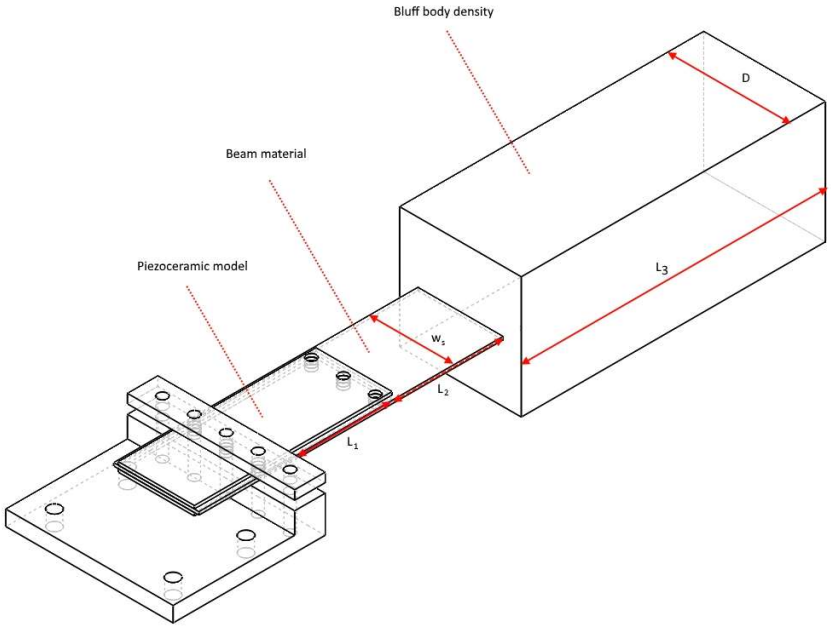

Figure 3.1 Reference design for the sensitivity analysis

The first three modes of vibration are located at well separated frequency in agreement with what was found in similar research such as [45] [58]. As already stated in Chapter 2 this gap between the first mode and the others is the premise for the application of the model implemented in this work and therefore the values obtained for the base case are showed in Table 3.2.

Mode	**Frequency [Hz]**
I mode	18.8
II mode	182.0
III mode	759.6

Table 3.2 Frequency obtained for the first three modes of vibration for the base case

The resulting modal shape obtained for the first mode of vibration is shown inFigure 3.2 , where it is evident that the beam deformation is major in the second region, that has the

minor stiffness and almost null for the third region, where the bluff body is almost a rigid body.

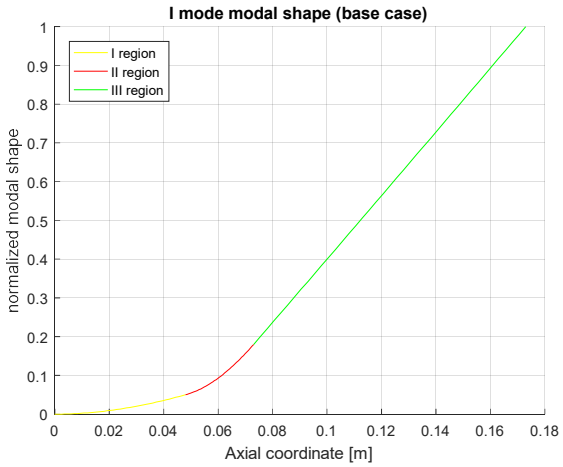

Figure 3.2 Modal shape for the three regions considered in the base case

3.2.1 Impact of the resistive load

The base case is first illustrated through a simple wind velocity and resistive load variation. The onset speed in meter per second varies according to the resistance connected to the PZT layer, forming the curve in Figure 3.3(a) where it is also depicted the wind velocity that gather the vortex resonance phenomenon. According to the model described the region upwards this line is the range of fluid velocities that trigger the galloping instability. With Figure 3.3(b) it is instead possible to evaluate if the quasi-steady theory is respected as the galloping onset speed is reached. If the reduced wind speed that the GPEH shows for the onset fluid velocity is low enough the aerodynamic model applied is no more a valid approximation, as explained in Chapter 2.

The influence of the resistance is also of major importance on the evaluation of the limit cycle characteristics in terms of both power and amplitude. For this comparison, a set of different wind speeds is considered for a wide resistance range and an integration is performed in order to reach the limit cycle of each case. For the lowest wind speed in Figure 3.4, it is noticed that the integration results in null tip displacement and harvested power for the resistance range for which the critical speed is higher than the one simulated: this basically means that the galloping instability is not reached and the system is damped to the equilibrium. It is interesting to observe also that the highest harvested power corresponds to the lowest amplitude oscillation cycles and this effect is more evident as the wind velocity is

much higher than the onset speed, see Figure 3.5. Another observation is that the optimal resistance for power harvesting is the one for which the critical speed reaches its peak. There is also a hint that the LCO (Limit Cycle Oscillation) amplitude has an almost linear dependency on the wind intensity.

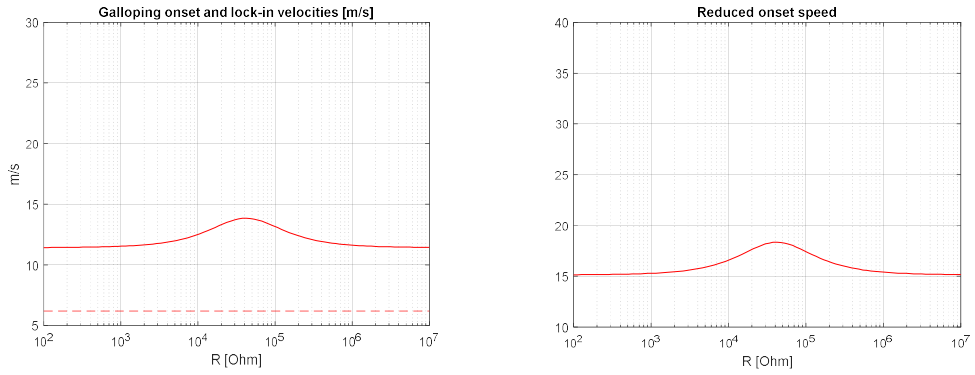

(a) (b)

Figure 3.3 (a) Reference case: onset speed (continuous line) and lock-in speed (dashed line) in m/s (b) reduced onset speed expected for galloping

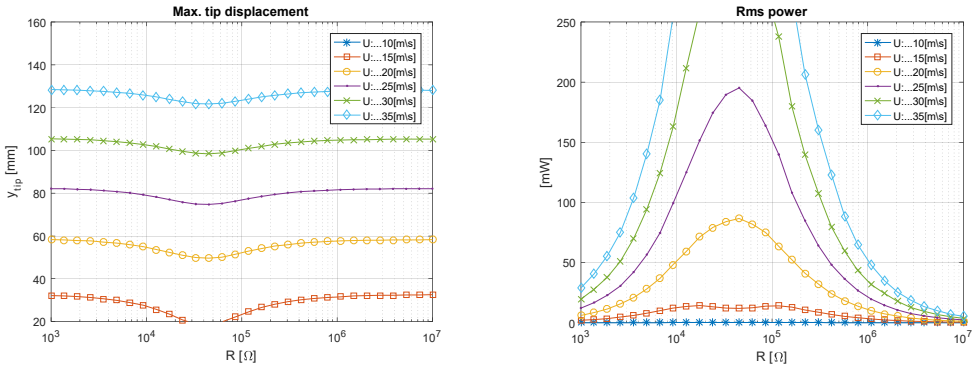

(a) (b)

Figure 3.4 Reference case: over possible resistances (a) Tip bluff body maximum displacement (b) rms power harvested during the limit cycle oscillations

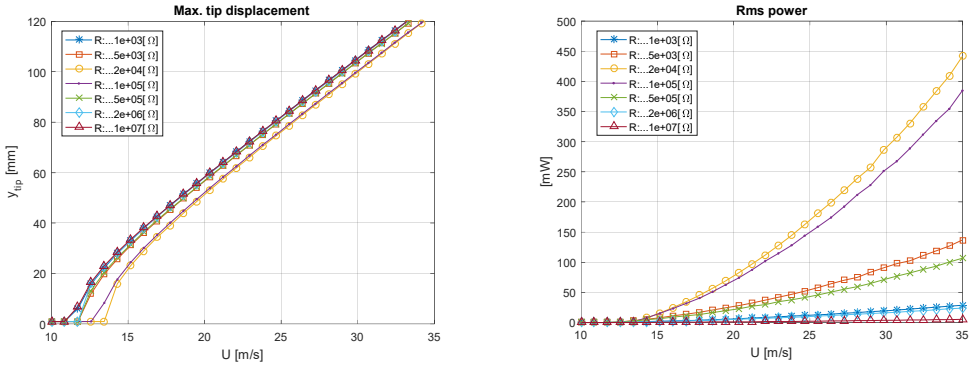

(a) (b)

Figure 3.5 Reference case: over a set of wind speeds (a) Tip bluff body maximum displacement (b) rms power harvested during the limit cycle oscillations

Another effect that can be seen by analyzing the transients of the solutions is that for the optimal resistance the time needed to reach the LCO is higher than the other cases as illustrated in Figure 3.6 (a). A significant curve can be plotted by taking the total time needed to reach the LCO considering different wind speed for the smallest resistance in the set as shown in Figure 3.6(b). Notice that the latter figure shows that for high wind speed a fast controller should be able to counteract the excessive amplitude of the limit cycle in a shorter time as the wind speed increases.

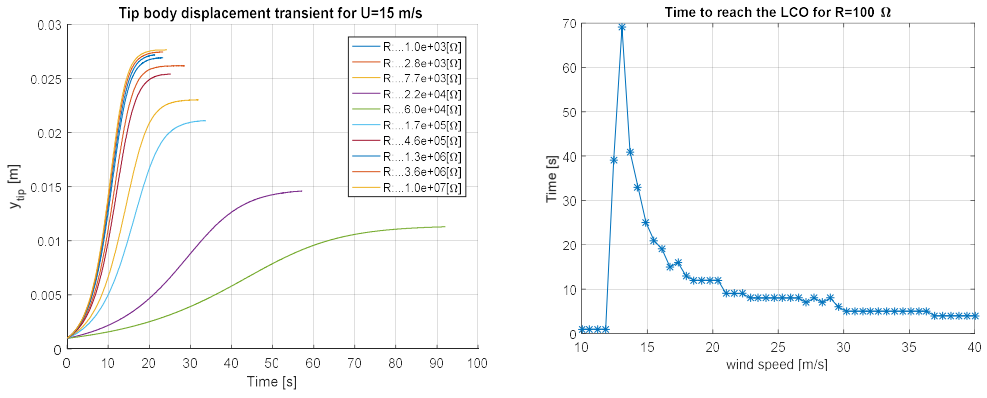

(a) (b)

Figure 3.6 (a) Reference case: envelops for tip displacement and (b) approximate transient time for R=100 Ω (tolerance: 1 s)

3.3 Preliminary considerations on the onset speed

The critical onset speed U_g can be evaluated according to the formulation developed in Chapter 2 for the lumped parameter model, recalled in the following equation:

$$U_g = \frac{4h\sqrt{m}\sqrt{k}}{\rho_{air} a_1 D L_3} \tag{3.4}$$

Which can also be re-arranged in the following way for a uniform bluff body with density ρ_b:

$$U_g = \frac{4h\sqrt{\rho_b}\sqrt{k}}{\rho_{air} a_1 \sqrt{L_3}} \tag{3.5}$$

which highlights the property that the onset speed of such GPEH design is not influenced by the side length dimension D. In the latter formula, to decrease the onset speed of galloping it is necessary:

- by reducing the non-dimensional mechanical-electrical damping of the system, which has a stabilizing contribution;
- to increase the value of the coefficient a_1, which depends upon the cross-section geometry adopted;
- to increase the bluff body length, which, despite an increase in the overall mass, yields to a significantly higher galloping force contribution;
- to decrease the bluff body density, so that the overall mass-damping is lowered and the aerodynamic damping that makes the system unstable is reached for a lower wind speed.

One significant observation is that the system should be designed with the lowest possible non-dimensional damping and with the cross-section that shows the highest value of a_1, so to lower the overall critical galloping speed. In order to understand which are the stiffness and modal mass values it is clear that there is no analytical solution for the problem since these are parameters that depend upon the modal shape. In particular, when the longitudinal design is considered most of the mechanical parameters in (3.4) have an impact on the modal mass and frequency of the model. For the reason mentioned, it is apparent that a sensitivity analysis must be carried out with the distributed parameter model, so that it is possible to evaluate the other objectives presented, such as maximum tip displacement and power output.

3.4 Sensitivity analysis

The parameters variations are reported in the following sections, grouped by the family of property interested by the variation.

3.4.1 Piezoelectric characteristics

The type of piezoceramics used for the application has a deep impact on the overall performance since a different product may significantly change the stiffness and the electro-mechanical coupling of the device. At the same time the connection used and the clamping position adopted have another important part in the determination of the total electromechanical coupling.

Choice of the piezoelectric patch

For this analysis two different commercial prototypes are investigated, whose compositions are reported in Table 3.3. As can be noted each product has its own substrates and the property of each layer gathers different characteristics both in terms of mechanical stiffness of the first region and of the electromechanical coupling. In fact, the piezoceramics are not composed by a single PZT layer as initially hypothesized, but are made of a series of substrates as depicted in Figure 3.7. In particular, the distance between the PZT layer and the neutral axis determines the level of strain sustained by the piezoelectric patch and therefore the electromechanical coupling level. In a symmetric configuration with two identical piezoelectric patches attached at both sides the neutral axis is located in the middle of the section and therefore the above-mentioned value is determined only by the thickness of the substrates below the PZT layer. In general, an asymmetric configuration with a single piezoceramic gathers an inferior level of coupling due to the fact that the neutral axis will be located closer to the PZT axis, according to the mechanical property of the section.

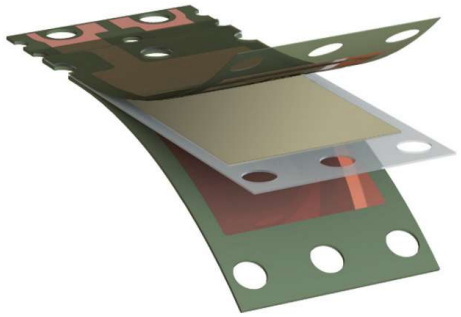

Figure 3.7 Representation of the different layers that forms a commercial piezoceramics (source: ©MIDE)

PPA 1001		**PPA 1011**	
Layer material	Thickness [mm]	Layer material	Thickness [mm]
Polyester	0.05	FR4	0.08
Copper	0.03	Copper	0.03
PZT 5H	0.15	PZT 5H	0.15
Stainless Steel 304	0.15	Copper	0.03
Polyimide	0.03	FR4	0.36
Total	0.46	Total	0.71

Table 3.3 Layers thickness for the two piezoceramics applied through the sensitivity analysis

The PZT patch is the same among the two devices and is a PZT 5H material, which has the properties listed in Table 3.4, as can be read from the manufacturer's datasheet [59].

$\boldsymbol{d_{31}}$	[m/V]	-320E-12
Young modulus	[GPa]	63
Capacitance	[nF]	100
Density	[Kg/m^3]	7800

Table 3.4 Properties of a PZT 5H layer

Piezoceramics performance comparison

In this simulation, the second region length is kept constant while the first region varies according to the piezo length, different in the two cases, so that the final prototype is shorter in case a PPA1001 is used, but almost the same modal shape is obtained. From Table 3.5 it is observed that there is a slight difference in the first mode frequency and therefore the onset speed is almost the same, as all the other parameters in the onset speed formula are constant, see Equation (3.5)(3.5), as represented in Figure 3.8. The integrations for different resistances and wind speeds shown in Figure 3.9 (a) (b) and Figure 3.10 (a) (b) determine that the piezo PPA1011 is the one that can harvest the biggest amount of energy and shows the higher efficiency as reported in Table 3.5. Depending on the power level needed the appropriate piezoceramic can be selected, considering also economic constraints since this is the main contribution.

Parameter: Piezo model	PPA1011	PPA1001
Frequency [Hz]	18,87	18,24
U_g min. [m/s]	11,43	11,05
U_g/U_r	1,85	1,85
χ	5,11E-04	4,67E-04
Max. efficiency [%] range 10 : 35 m/s	0,51	0,46

Table 3.5 Effect of piezoceramic characteristics: summary results

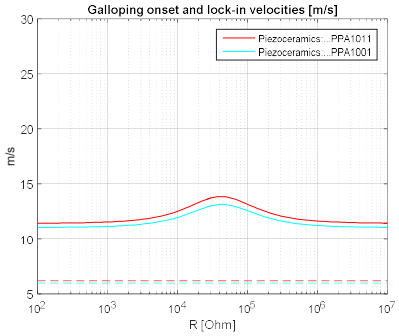

Figure 3.8 Effect of piezoceramic characteristics: galloping onset speed (continuous line) and lock-in speed (dashed line)

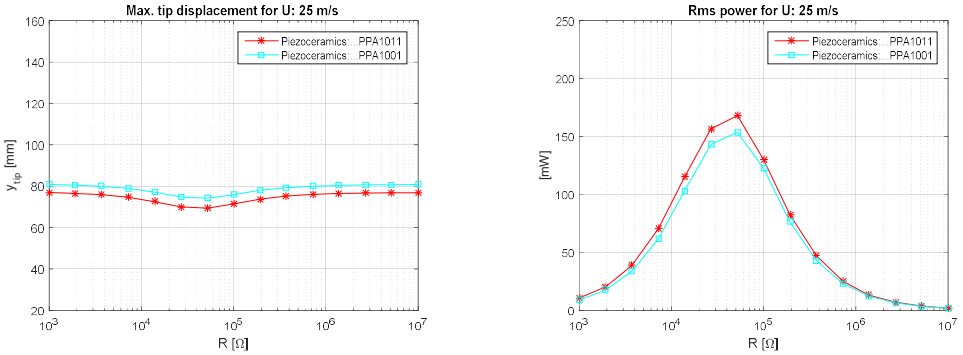

(a) (b)

Figure 3.9 Effect of piezoceramic characteristics: for the set of various resistances (a) Tip bluff body maximum displacement (b) rms power harvested during the limit cycle oscillations

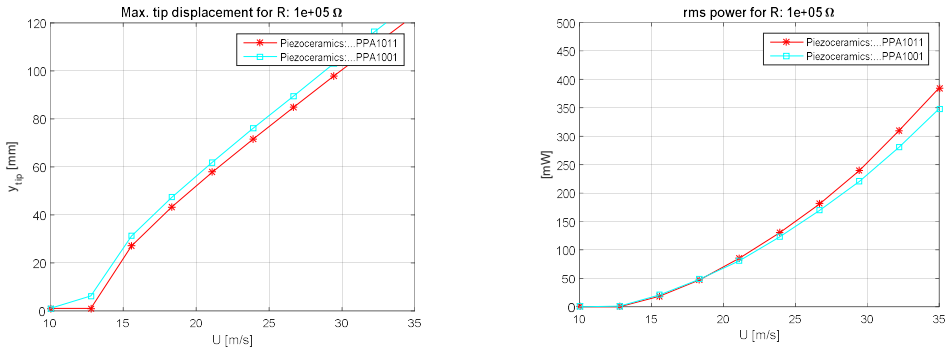

(a) (b)

Figure 3.10 Effect of piezoceramic characteristics: for the range of wind speeds considered (a) Tip bluff body maximum displacement (b) rms power harvested during the limit cycle oscillations

Clamping position

As the manufacturer normally indicates different positions at which the clamping is recommended the objective of this analysis is to evaluate the possible advantage of each of the three possible conditions named “clamp -6” “clamp 0” and “clamp +6”. The length of the second region is kept constant, so that even in this case the overall axial dimension of the prototype is indirectly changed by varying the clamping. For what concern the onset speeds these are not modified by the clamp variations as reported in Figure 3.11, because the frequency negligibly changed among the variations. By comparing the modal shapes obtained in each case it is possible to see that a longer piezoelectric area (longer first region) involves a higher strain over the PZT patch so that the electromechanical coupling is higher, see Table 3.6. The derivative of the modal shape in correspondence to the end of the first region is in fact higher as the ratio between L1 and L2 (see Figure 3.1) is incremented (no difference would be obtained having the second region equal to zero). A small difference is noticed in Figure 3.12(a) and Figure 3.13(b) on the maximum tip displacement even if the power harvested is significantly higher for a “clamp -6” configuration as attested in Figure 3.12(b) and Figure 3.13(b) and also by the efficiency level.

Parameter: Clamp position	clamp-6	clamp+0	clamp+6
Frequency [Hz]	18,31	18,87	19,42
U_g min. [m/s]	11,11	11,43	11,75
U_g/U_r	1,85	1,85	1,84
χ	5,64E-04	5,11E-04	4,44E-04
Max. efficiency [%] range 10 : 35 m/s	0,63	0,51	0,37

Table 3.6 Effect of clamping positions: summary results

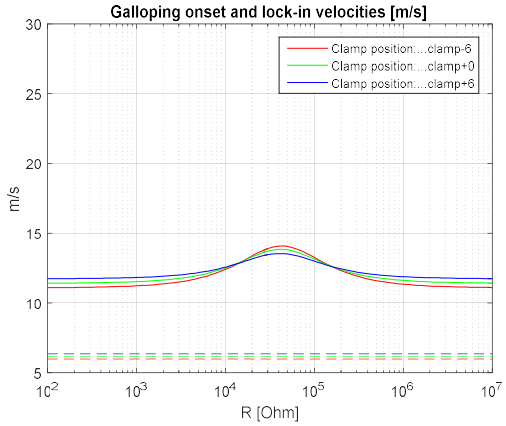

Figure 3.11 Effect of clamping positions: galloping onset speed (continuous line) and lock-in speed (dashed line)

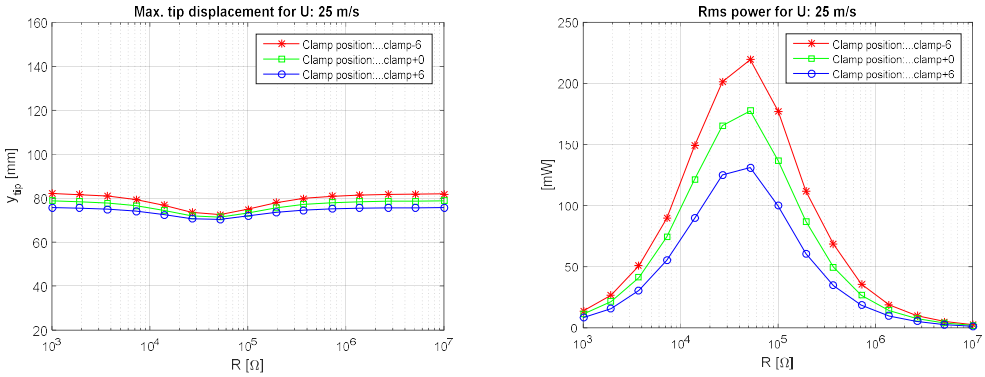

(a) (b)

Figure 3.12 Effect of clamping positions: for the set of various resistances (a) Tip bluff body

maximum displacement (b) rms power harvested during the limit cycle oscillations

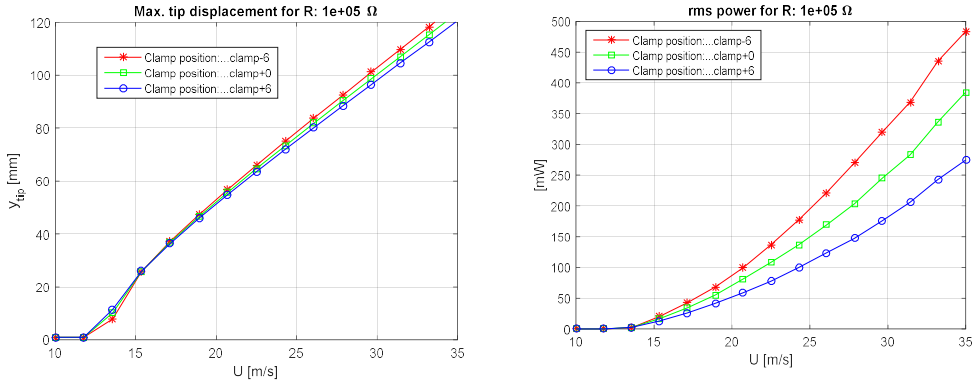

(a) (b)

Figure 3.13 Effect of clamping positions: for the range of wind speeds considered (a) Tip bluff body maximum displacement (b) rms power harvested during the limit cycle oscillations

Piezoelectric connection

The advantage of a parallel connection in terms of harvested power is clearly described in this simulation, in which the two connections are obtained using proper parameters for the electromechanical coupling and piezo capacitance. Not much difference can be noticed for what concerns the onset galloping speed since the minimum Vg, as in Equation (3.5), has no relation with the electrical part of the apparatus, see Figure 3.14. The tip displacements obtained for different resistances and wind speeds are very similar as shown in Figure 3.15(a) and Figure 3.16(a). On the other side the power levels are higher for the parallel configuration as reported in Figure 3.15(a) and Figure 3.16(b). The parameter that is mainly varied is in fact the electromechanical coupling and consequently the overall efficiency, as reported in Table 3.7; the other mechanical parameters remain almost the same.

Parameter: Connection type	parallel	series
Frequency [Hz]	18,87	18,87
U_g min. [m/s]	11,43	11,42
U_g/U_r	1,85	1,85
χ	5,11E-04	2,56E-04
Max. efficiency [%] range: 10 : 35 m/s	0,51	0,28

Table 3.7 Effect of piezoelectric connection: summary results

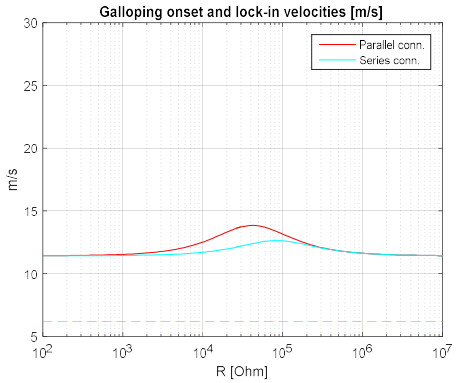

Figure 3.14 Effect of piezoelectric connection: galloping onset speed (continuous line) and lock-in speed (dashed line)

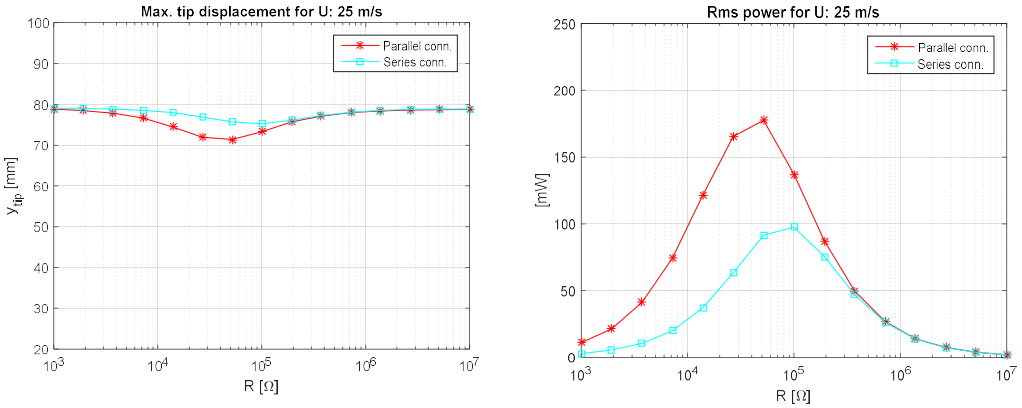

(a) (b)

Figure 3.15 Effect of piezoelectric connection: for the set of various resistances (a) Tip bluff

body maximum displacement (b) rms power harvested during the limit cycle oscillations

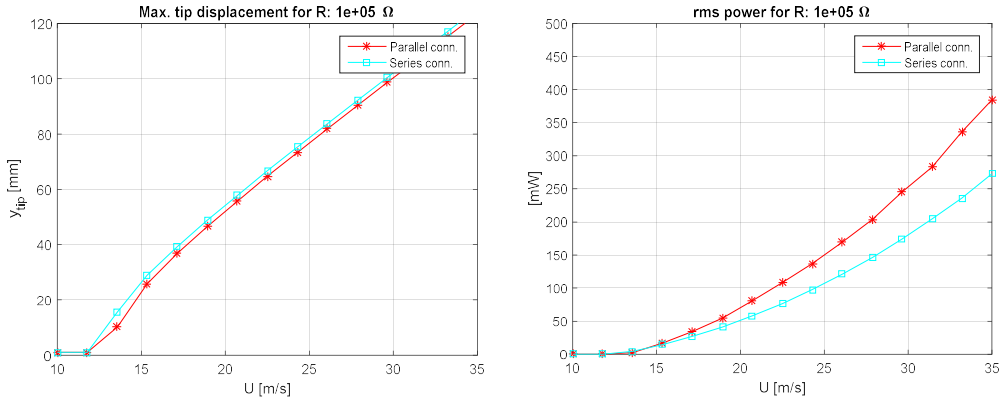

(a) (b)

Figure 3.16 Effect of piezoelectric connection: for the range of wind speeds considered (a) Tip bluff body maximum displacement (b) rms power harvested during the limit cycle oscillations

3.4.2 Aerodynamic parameters sensitivity

In this section the parameters concerning the aerodynamic force are changed so that the effects of an increased or decreased galloping force are studied. This is done by changing the cross-section geometry, the length or the side dimension of the bluff body. It is obvious that in a practical case these modifications imply also a change in the mechanical properties of the model that will have a different modal mass and frequency.

Cross-section geometry

The main impact on the aerodynamic force that the design of a GPEH has is given by the choice of the cross-section geometry. This in fact highly affects the critical onset speed as well as the power efficiency performances. In this case the variations are simply done by changing the aerodynamic coefficients a_1 and a_3 according to the shape selected: in such a way, it is assumed that the bluff body mass, stiffness and side width are the same among the cases simulated, while the aerodynamic force will result in a different contribution. The aerodynamic coefficients are the one described in section 2.3.2, with reference to the work by Barrero-Gil et al. [3].It is shown in Figure 3.17 that the highest onset speed is given by a D-section profile, which has on the other side the advantage to offer a great separation between lock-in and galloping. These results are dependent upon a_1 only, coherently with the

simplified formula presented in equation (3.5), where the first aerodynamic coefficient is a denominator. The other profiles considered have an onset speed located in a more convenient range, with the triangular 30° configuration having the lowest value. With the simulation at different wind speeds, Figure 3.19(a) (b), it is confirmed that the maximum power is generated thanks to the triangular 30° configuration, even if the limit cycle oscillations reached are to be considered critical for the prototype. From this point of view an advantage of the square section is that it has a reasonable onset speed and, at the same time, the LCO amplitudes are below the limit for almost all the range of interest when the optimal resistance is applied, see Figure 3.18 (a) (b). The summary in Table 3.8 shows that the mechanical parameters are not changed, while the overall efficiency varies according to the cross-section applied.

It is important to notice that the present simulation is not to be intended as a comparison of the efficiency that can be gathered with the different cross section. For a result of that kind the analysis should be carried out for a different range of fluid speeds, so that every prototype is well beyond its galloping onset speed. An experimental study by Yang et al [32] showed that the galloping onset speed for the D-section is the highest with respect to the others (square, equilateral triangle, rectangular were considered in a T-layout GPEH). The same trend for the galloping speed is found in Abdelkefi et al. [58]. The same conclusions can be drawn even in the latter study for what concern the LCO reached and the power output achieved by the different cross-section geometries.

Parameter: Cross-section	**square**	**triangle 30°**	**triangle 53°**	**D-sect**
Frequency [Hz]	18,868	18,868	18,868	18,868
U_g min. [m/s]	11,427	9,067	13,837	33,267
χ	5,11E-04	5,11E-04	5,11E-04	5,11E-04
Max. efficiency [%] range: 10 : 35 m/s	0,508	2,330	0,824	na

Table 3.8 Effect of cross-section geometry: summary results

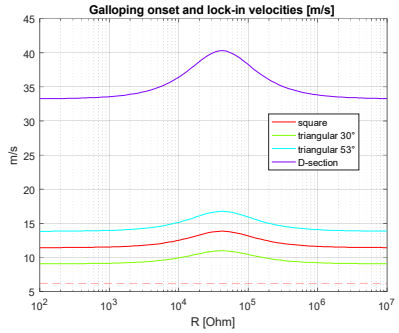

Figure 3.17 Effect of cross-section geometry: galloping onset speed (continuous line) and lock-in speed (dashed line)

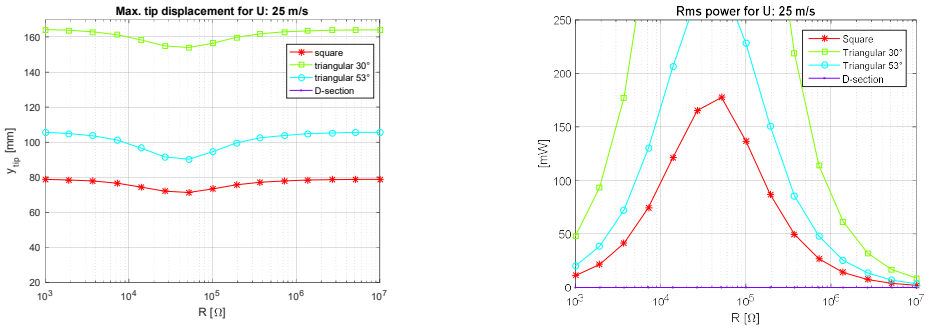

(a) (b)

Figure 3.18 Effect of cross-section geometry: for the set of various resistances (a) Tip bluff body maximum displacement (b) rms power harvested during the limit cycle oscillations

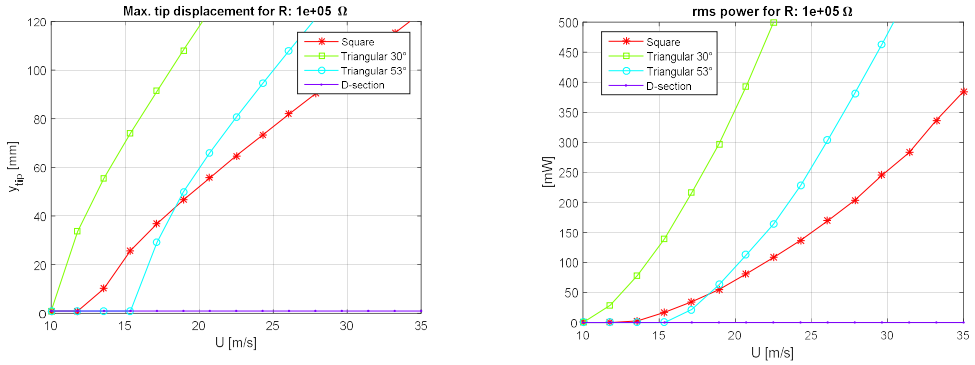

(a) (b)

Figure 3.19 Effect of cross-section geometry: for the range of wind speeds considered (a) Tip bluff body maximum displacement (b) rms power harvested during the limit cycle oscillations

Bluff body length

As the bluff body is extended a major aerodynamic force is exerted on the prototype and therefore a bigger power is converted into mechanical vibrations, but on the other side the electromechanical coupling is decreased since the strain is less on the PZT patch. If the extension has a non-negligible weight the modal mass will increase and therefore the frequency will be lowered as it is clearly described in Table 3.9. The onset speed in Figure 3.20 is lowered as the length is increased, confirming the trend predicted by equation (3.5). On the other side the ratio U_g/U_r is kept constant, meaning that the bluff body length can be used to tune the onset speed but not to reduce the interaction with VIV. Major differences are found in the limit cycle characteristics with a high impact on the amplitudes that are limited only for a short bluff body as seen in Figure 3.21(a) and Figure 3.22(a). It should be noticed that the critical value for the maximum amplitude is different for each case and increases with the parameter under investigation. The power harvested grows with the bluff body length even if there is only a minimal difference between the last two values considered as described by Figure 3.22(b) and Figure 3.22(b). In conclusion, for this parameter two main effects are recognized as the length is increased:

- the electromechanical coupling is reduced due to the different modal shape
- the vibrational power increases because the integral of the aerodynamic force over the bluff body length is higher.

Parameter: L3 length	**75 mm**	**100 mm**	**150 mm**	**200 mm**
Frequency [Hz]	23.09	18.87	13.74	10.76
U_g **min. [m/s]**	18.69	11.43	5.54	3.25
U_g/U_r	2.47	1.85	1.23	0.92
χ	6.89E-04	5.11E-04	3.30E-04	2.41E-04
Max. efficiency [%] range 10 : 35 m/s	0.40	0.51	0.37	0.33

Table 3.9 Effect of bluff body length: summary results

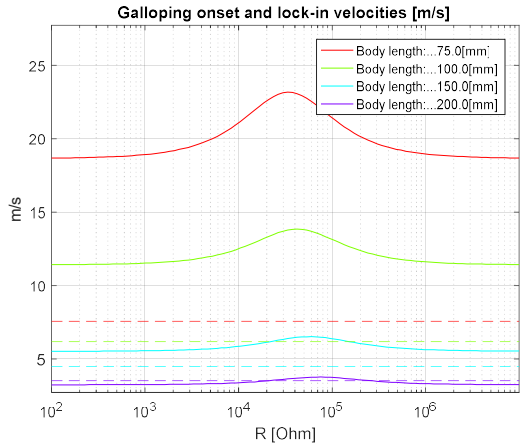

Figure 3.20 Effect of bluff body length: galloping onset speed (continuous line) and lock-in speed (dashed line)

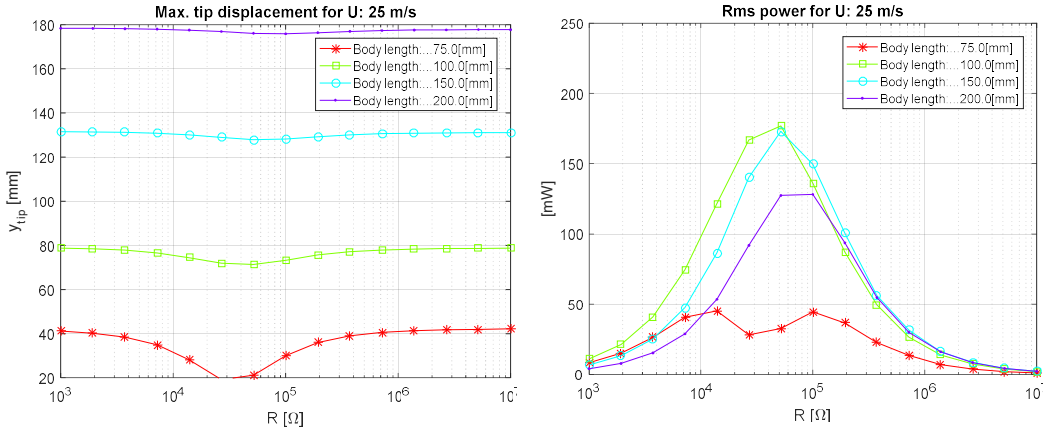

(a) (b)

Figure 3.21 Effect of bluff body length: for the set of various resistances (a) Tip bluff body maximum displacement (b) rms power harvested during the limit cycle oscillations

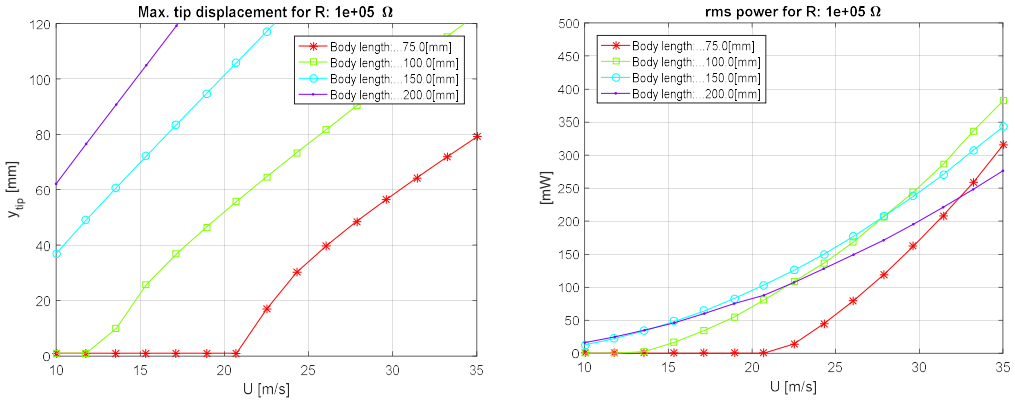

(a) (b)

Figure 3.22 Effect of bluff body length: for the range of wind speeds considered (a) Tip bluff body maximum displacement (b) rms power harvested during the limit cycle oscillations

Side length sensitivity

The side dimension of the bluff body is modified from a minimum value of 20 mm up to a maximum dimension of 60 mm. Since the density of the bluff body is constant the modal mass and frequency is changed according to the variation of this parameter as reported in Table 3.10. The onset speed is related to the side dimension as shown in Figure 3.23(a), while Figure 3.23(b) represents the capability of the parameter investigated to separate the galloping from VIV since the reduced onset speed is significantly greater for a small side length. Through the simulations at various resistances and wind speeds shown in Figure 3.24(a) (b) and Figure 3.25(a) (b) it is clear that a higher side length increases both the power harvested and the maximum tip body oscillation. Once the proper material is chosen, and a certain maximum length fixed, it is then sufficient to select the correct side dimension in order to tune the desired power output. The only dangerous implication is that a high side dimension will also result in more critical oscillation amplitudes. In Table 3.10 it can be noticed a small change of the electromechanical coupling which is given by the fact that, as the side length grows, the third region is stiffer. This effect yields to a higher modal shape derivative at the end of the piezoelectric patch and therefore, see equation (2.79), to a higher electromechanical coupling.

Parameter: Side length	**20 mm**	**30 mm**	**40 mm**	**50 mm**	**60 mm**
Frequency [Hz]	36.07	24.95	18.87	15.14	12.63
U_g **min. [m/s]**	11.02	11.36	11.43	11.44	11.45
U_g/U_r	1.86	1.85	1.85	1.84	1.84
χ	4.65E-04	5.03E-04	5.11E-04	5.13E-04	5.14E-04
Max. efficiency [%] range 10 : 35 m/s	0.47	0.50	0.50	0.51	0.51

Table 3.10 Effect of side length sensitivity: summary results

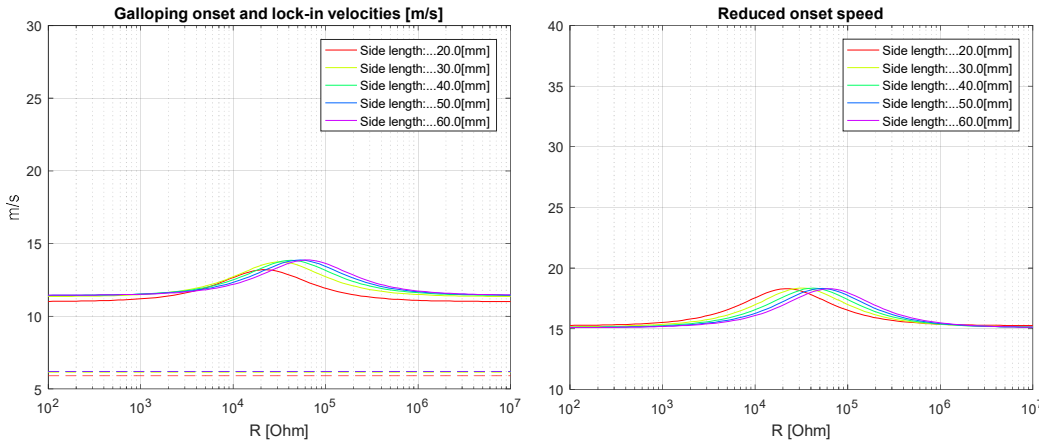

(a) (b)

Figure 3.23 (a) Effect of side length sensitivity: onset speed (continuous line) and lock-in speed (dashed line) in m/s (b) reduced onset speed expected for galloping

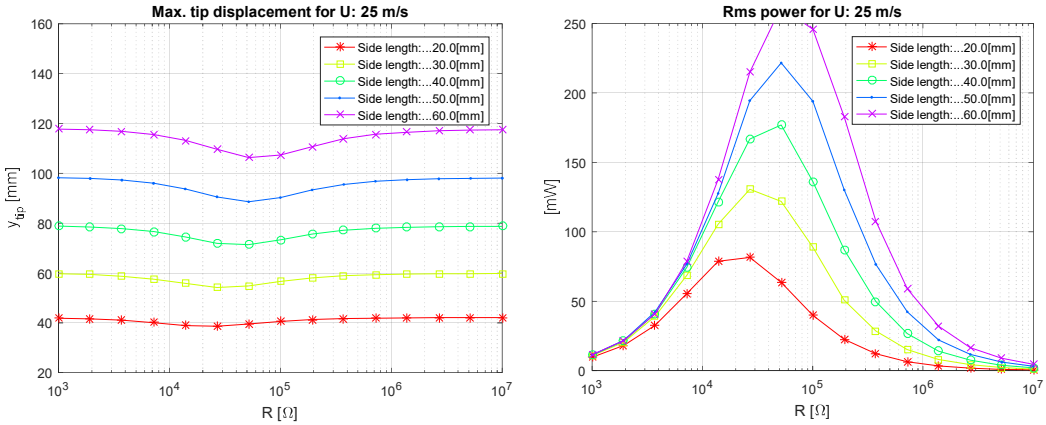

(a) (b)

Figure 3.24 Effect of side length sensitivity: for the set of various resistances (a) Tip bluff body maximum displacement (b) rms power harvested during the limit cycle oscillations

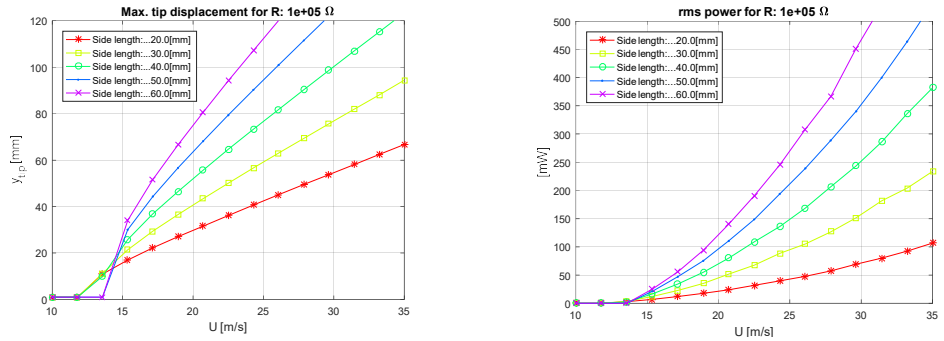

(a) (b)

Figure 3.25 Effect of side length sensitivity: for the range of wind speeds considered (a) Tip bluff body maximum displacement (b) rms power harvested during the limit cycle oscillations

3.4.3 Electro-mechanical parameters sensitivity

In this section, various parameters are considered that mainly affects the electromechanical coupling. This result is obtained by forcing the distance between the PZT layer and the neutral axis or by altering the modal shape.

Beam thickness

The supporting beam is simulated with different thicknesses in the range 0.3 - 0.7 mm. The main effect is that the strain level on the PZT is higher as the piezoceramic is farther from the neutral axis. The results in term of electromechanical coupling are reported in Table 3.11 with a clear advantage for the thicker solution. As a trade-off, Figure 3.26 shows that the onset speed is deeply increased with the thickness, so that a thick beam will not allow the energy harvesting at all the considered speeds. The limit cycle is completely different both in terms of power harvested and tip displacements as shown in Figure 3.27 and Figure 3.28. In particular, it is clear from Figure 3.28(a) that the beam thickness may be adjusted in order to have a wider range of efficiency of the GPEH, since almost the same area is described by the different curves in terms of power over the range of wind velocities.

Parameter: beam thickness	**0.3 mm**	**0.4 mm**	**0.5 mm**	**0.6 mm**	**0.7 mm**
Frequency [Hz]	10,86	15,04	18,87	22,34	25,54
U_g **min. [m/s]**	5,50	8,36	11,43	14,66	18,05
U_g/U_r	1,54	1,69	1,85	2,00	2,16
χ	1,77E-04	3,34E-04	5,11E-04	6,89E-04	8,57E-04
Max. efficiency [%] range 10 : 35 m/s	0,23	0,38	0,51	0,44	0,40

Table 3.11 Effect of beam thickness: summary results

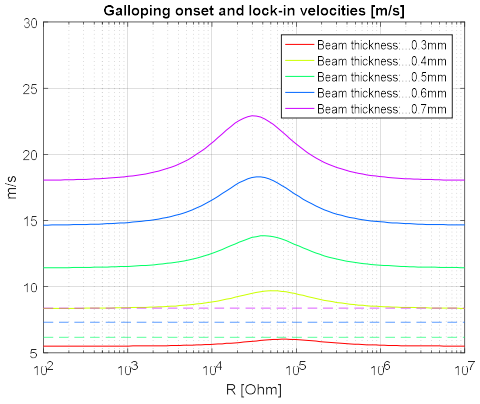

Figure 3.26 Effect of beam thickness: galloping onset speed (continuous line) and lock-in speed (dashed line)

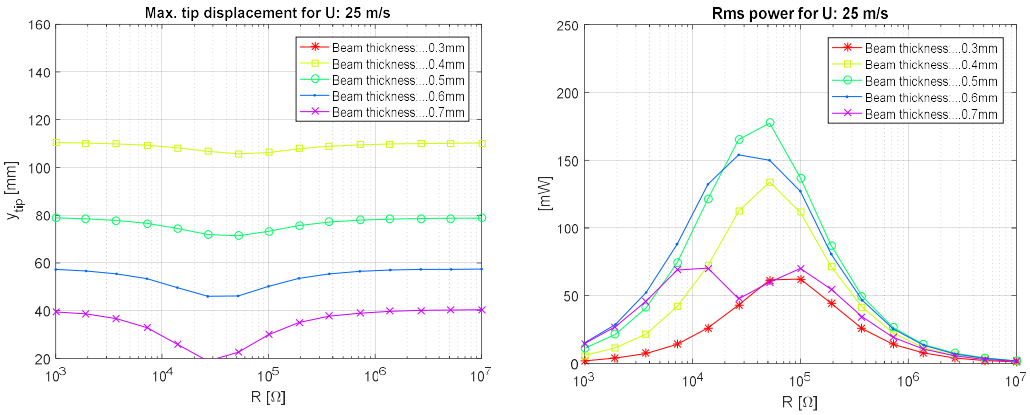

(a) (b)

Figure 3.27 Effect of beam thickness: for the set of various resistances (a) Tip bluff body maximum displacement (b) rms power harvested during the limit cycle oscillations

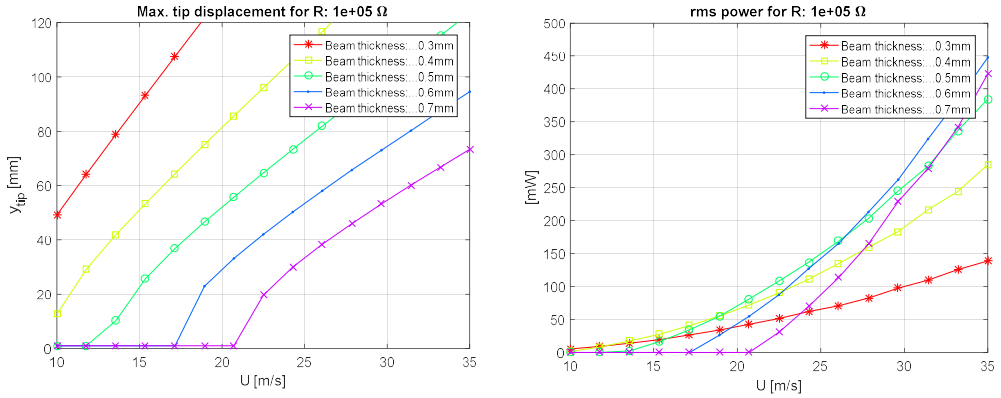

(a) (b)

Figure 3.28 Effect of beam thickness: for the range of wind speeds considered (a) Tip bluff body maximum displacement (b) rms power harvested during the limit cycle oscillations

Second region length

In this case the length of the second region is changed, so that the modal shape and frequency are modified. The considered cases range from a null second region to a maximum length of 40 mm. The modal shape is significantly changed with the extension of the second region, that lowers the modal shape derivative at the end of the PZT. It is clear from Table

3.12 that the electromechanical coupling is consequently modified, with a maximum value reached when the second region is minimum. The impact of the second region is meaningful also on the frequency. Therefore, the onset speeds are higher as L_2 is decreased as shown in Figure 3.29. Even if the highest electromechanical coupling is obtained for a null second region it is apparent that the optimal power harvesting is found for an intermediate value of L_2. It is shown in Figure 3.31(b) that the power optimization, by varying the second region length, is not univocal: one should choose whether it is preferable to have higher peak of power for a short range of wind speeds or lower average power for a wider range of fluid speeds. On the other hand, the tip displacement can become critical for too high values of the parameter varied as found in Figure 3.30(a) and Figure 3.31(b).

An analysis similar to the one carried out in this paragraph was done by Zhao and Yang [30], who claimed that the use of a beam stiffener helps granting higher power, if the length of this tool is appropriately dimensioned. The results obtained by this research are in agreement with the conclusions drawn by the present analysis, with the main difference that the alteration of the second region length has a deep impact on the galloping onset speed.

Parameter: L2 length	**0.1 mm**	**10 mm**	**25 mm**	**40 mm**
Frequency [Hz]	39,92	27,75	18,87	14,28
U_g **min. [m/s]**	24,38	16,83	11,43	8,67
U_g/U_r	1,86	1,85	1,85	1,85
χ	1,80E-03	9,41E-04	5,11E-04	3,43E-04
Max. efficiency [%]	0,29	0,44	0,51	0,41
range 10 : 35 m/s				

Table 3.12 Effect of second region length: summary results

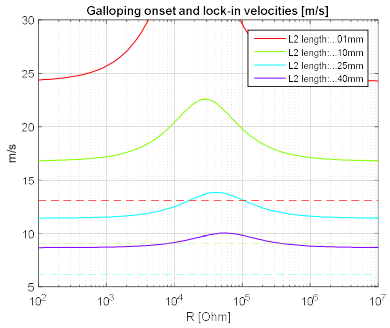

Figure 3.29 Effect of second region length: galloping onset speed (continuous line) and lock-in speed (dashed line)

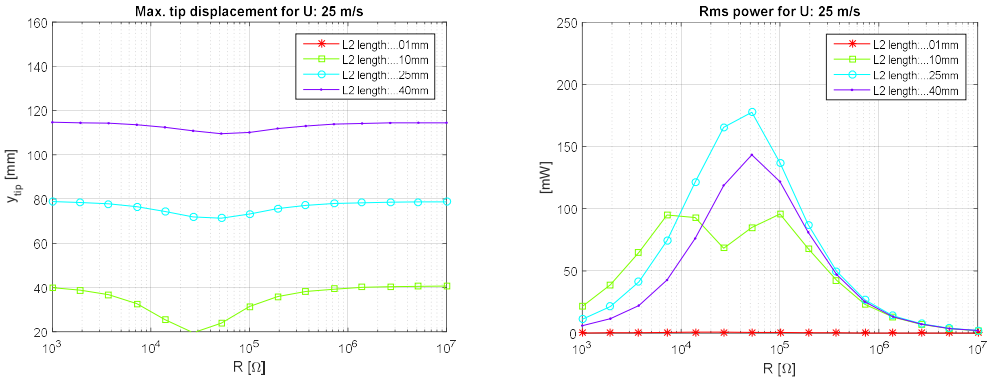

(a) (b)

Figure 3.30 Effect of second region length: for the set of various resistances (a) Tip bluff body maximum displacement (b) rms power harvested during the limit cycle oscillations

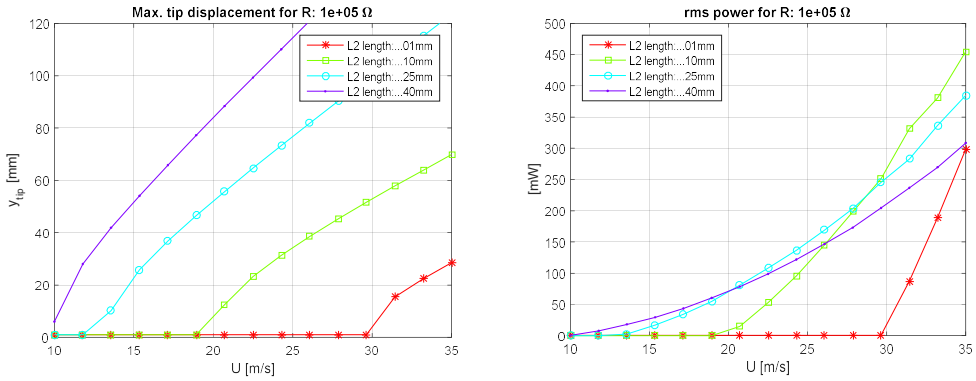

(a) (b)

Figure 3.31 Effect of second region length: for the range of wind speeds considered (a) Tip bluff body maximum displacement (b) rms power harvested during the limit cycle oscillations

Beam material

Two materials are considered in the simulations, that are the ones most used in the available prototypes: aluminum and steel. They differ both in density and stiffness and therefore a variation on this parameter yields in particular to a different frequency and electromechanical coupling. The effects are quantitively listed in Table 3.13, where it is seen that these are the main modifications introduced on the model. For what concerns the onset

speed, this is clearly lower for the aluminum case in Figure 3.32, where the overall system is less stiff. It is also apparent that for the beam thickness selected the case of a steel beam presents greater advantages both in terms of limited tip oscillations and harvested powers as described in Figure 3.33(a) (b) and Figure 3.34(a) (b).

Parameter: Beam material	**steel**	**aluminum**
Frequency [Hz]	18,87	13,79
U_g min. [m/s]	11,43	6,08
U_g/U_r	1,85	1,34
χ	5,11E-04	2,10E-04
Max. efficiency [%]	0,51	0,22
range 10 : 35 m/s		

Table 3.13 Effect of beam material: summary results

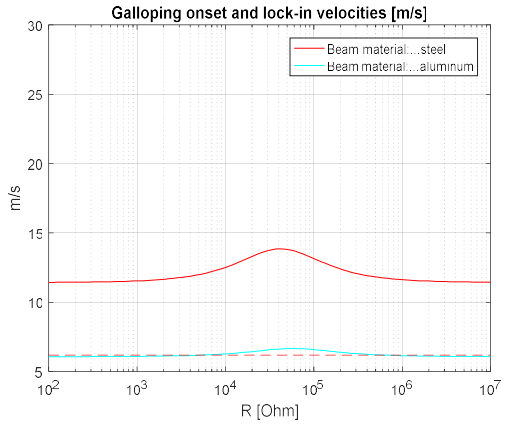

Figure 3.32 Effect of beam material: galloping onset speed (continuous line) and lock-in speed (dashed line)

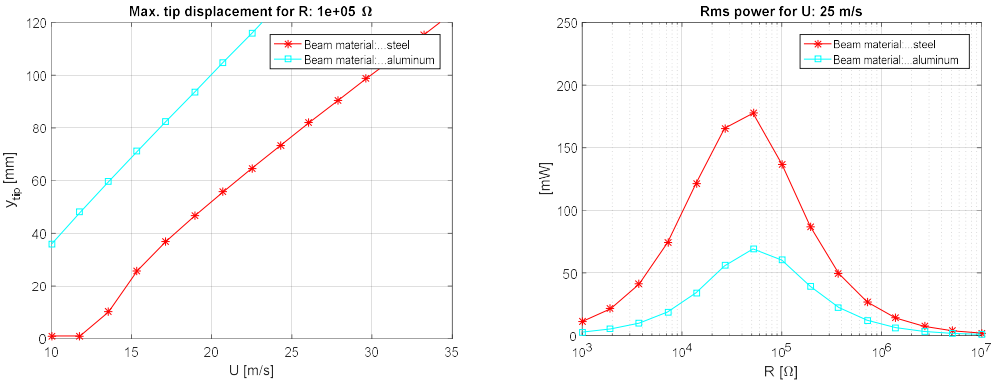

(a) (b)

Figure 3.33 Effect of beam material: for the set of various resistances (a) Tip bluff body maximum displacement (b) rms power harvested during the limit cycle oscillations

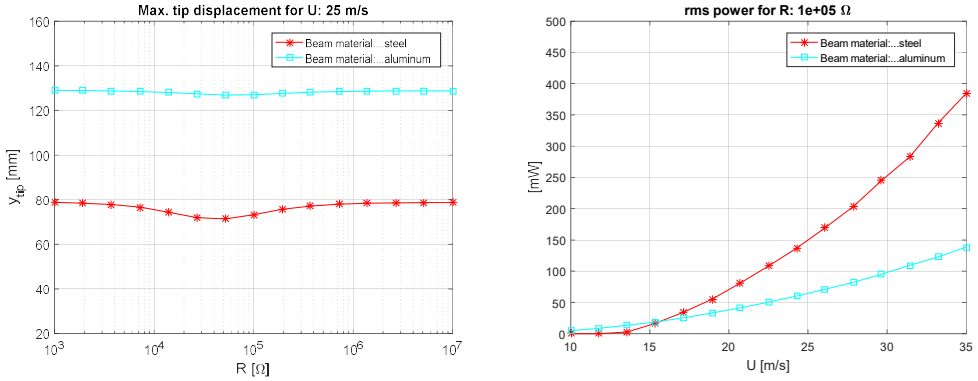

(a) (b)

Figure 3.34 Effect of beam material: for the range of wind speeds considered (a) Tip bluff body maximum displacement (b) rms power harvested during the limit cycle oscillations

Beam width

The beam side dimension may be changed in particular to change the modal shape, so that the strain exerted on the PZT is higher. In Table 3.14 it is apparent that a widener beam gathers a slightly higher frequency, but yields an increase of around +25% on the electromechanical coupling. The consequences on the onset speed can be seen in Figure 3.35, where the widener beam shows a higher galloping critical velocity. A comparison between

Figure 3.36 (a) and (b) brings to the conclusion that for the same power output a lower tip displacement is required for the widener beam which means that the efficiency in the latter case is higher. From Figure 3.37(a) (b) it is noticed that the power level reached by the wider beam case is better, but has a lower range of working wind speeds.

Parameter: Beam width	**28 mm**	**40 mm**
Frequency [Hz]	18,87	19,66
U_g min. [m/s]	11,43	14,01
U_g/U_r	1,85	2,17
χ	5,11E-04	6,30E-04
Max. efficiency [%]	0,51	0,47
range 10 : 35 m/s		

Table 3.14 Effect of beam width: summary results

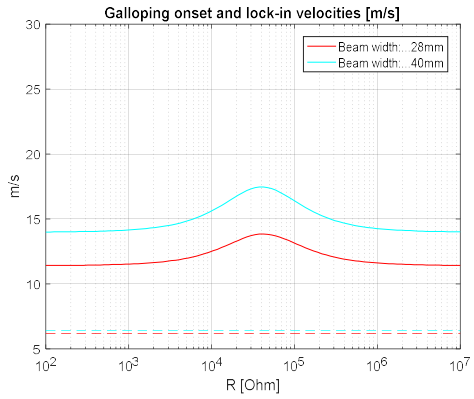

Figure 3.35 Effect of beam width: galloping onset speed (continuous line) and lock-in speed (dashed line)

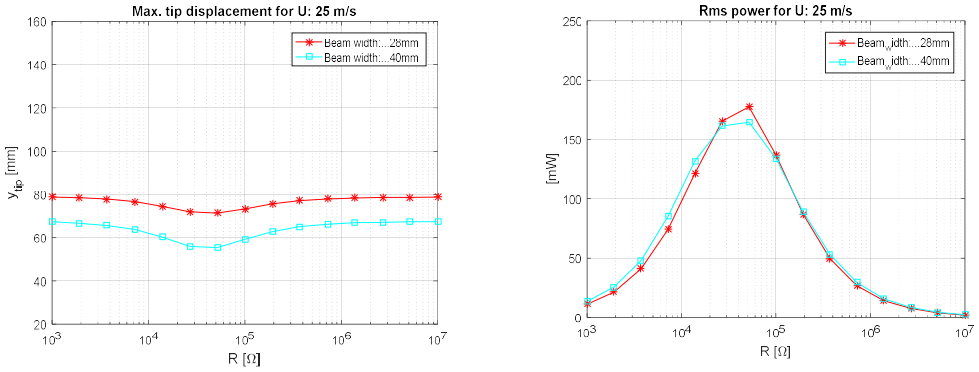

(a) (b)

Figure 3.36 Effect of beam width: for the set of various resistances (a) Tip bluff body maximum displacement (b) rms power harvested during the limit cycle oscillations

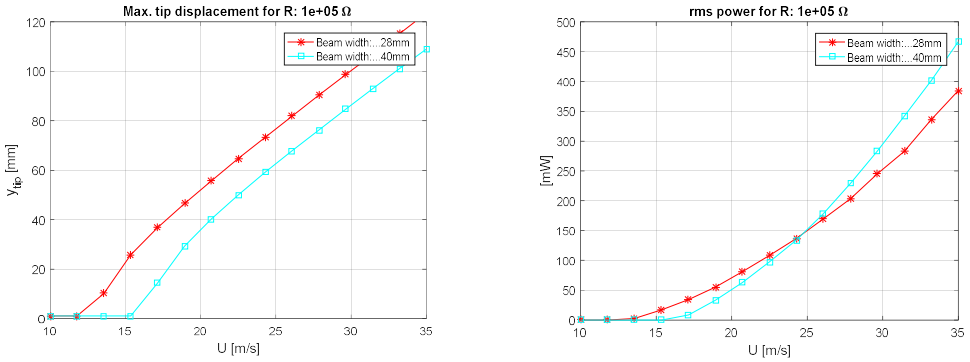

(a) (b)

Figure 3.37 Effect of beam width: for the range of wind speeds considered (a) Tip bluff body maximum displacement (b) rms power harvested during the limit cycle oscillations

3.4.4 Mechanical parameters sensitivity

In this last section, the varied parameters are the ones that gather different modal mass and frequency without altering the electromechanical coupling: these are for instance the tip mass obtained varying the bluff body density and the overall non-dimensional damping of the system.

Bluff body density

The modal mass can effectively be modified by varying the bluff body material, so that at higher densities the mass contribution grows significantly. The range of densities considered in this paragraph varies from a polystyrene bluff body to a low density synthetic resin. As already stated by looking at the first order approximation of the galloping force in equation (3.5), the onset speed grows as the tip mass is increased: a graphical representation is given in Figure 3.38(a). It is interesting to notice also that a greater mass helps detaching the lock-in region from the galloping onset as proved by Figure 3.38(b). There is no effect on the electromechanical coupling as can be seen in Table 3.15, but one can notice also that a very low density material may also involve a very poor Young modulus and therefore it may affect the modal shape, lowering the value of χ. For the present simulation, however the Young modulus was kept constant in order to evaluate only the implication of a different tip mass. Looking again at Table 3.15 one can see that the mass has a deep impact on the first mode frequency, so that the bluff body density is a key design parameter for the frequency tuning. The power harvested and the amplitude of oscillation at high wind speeds grow meaningfully as the tip mass is increased as reported in Figure 3.40(a) (b). By looking at Figure 3.39(a) (b) it is possible to conclude that for the same flow speed the LCO maximum amplitude is much greater for the heavier tip mass.

Parameter: Rho bluff [Kg/m^3]	**30**	**70**	**100**	**150**	**200**
Frequency [Hz]	24,58	20,79	18,87	16,59	14,98
U_g **min. [m/s]**	8,78	10,38	11,43	13,00	14,40
U_g/U_r	1,09	1,52	1,85	2,39	2,93
χ	5,13E-04	5,12E-04	5,11E-04	5,10E-04	5,10E-04
Max. efficiency [%] range 10 : 35 m/s	0,50	0,51	0,51	0,47	0,44

Table 3.15 Effect of bluff body density: summary results

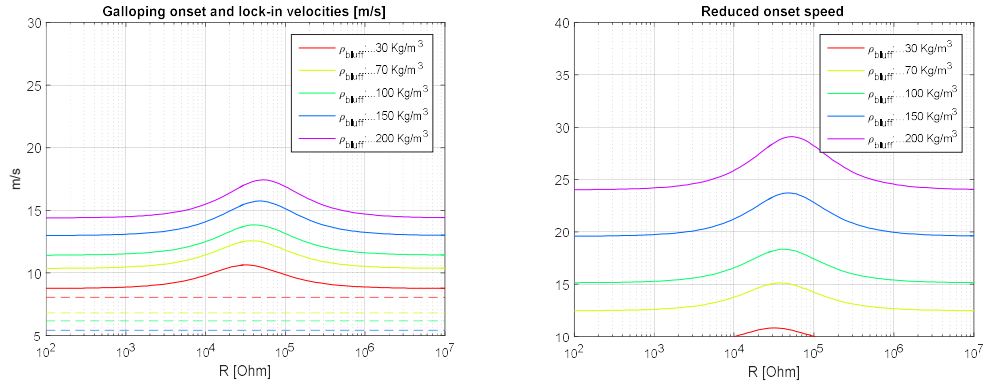

(a) (b)

Figure 3.38 (a) Effect of bluff body density: Onset speed (continuous line) and lock-in speed (dash line) in m/s (b) reduced onset speed expected for galloping

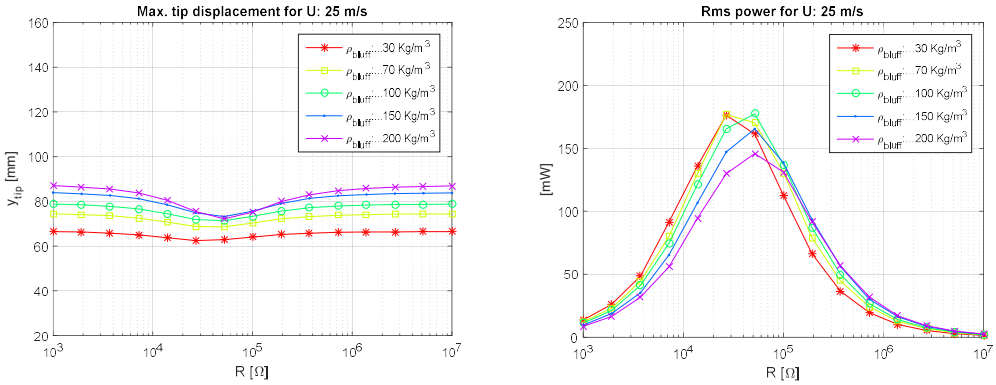

(a) (b)

Figure 3.39 Effect of bluff body density: for the set of various resistances (a) Tip bluff body maximum displacement (b) rms power harvested during the limit cycle oscillations

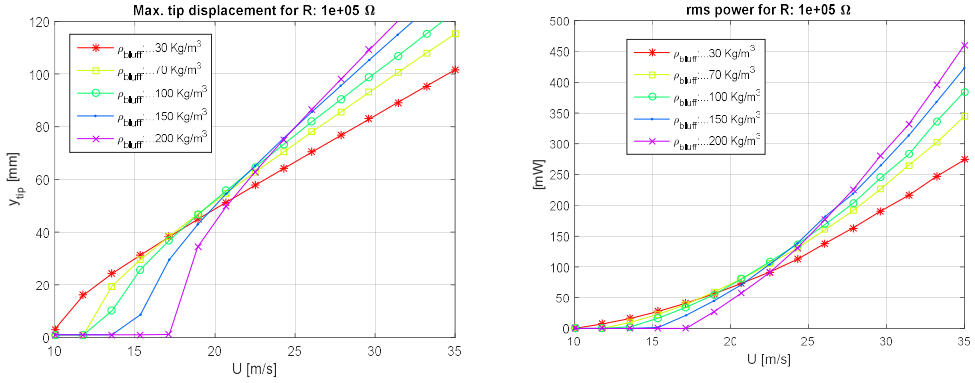

(a) (b)

Figure 3.40 Effect of bluff body density: for the range of wind speeds considered (a) Tip bluff body maximum displacement (b) rms power harvested during the limit cycle oscillations

Mechanical damping

In this simulation, the non-dimensional damping parameter is varied between 0,5 and 2%, which is a reasonable range with respect to the values found in the prototypes reviewed in the first chapter. It is important to notice that this parameter is the only one that cannot be achieved in the realization of the final prototype, therefore its role is crucial for the overall results. The present simulation is to be intended as analysis of the possible effects that are predicted if this parameter is overestimated or underestimated with respect to the reference value selected. As can be seen from the graphics shown in Figure 3.41 a higher non-dimensional damping with respect to the one expected results in an onset speed higher than the one reached by the application. When the non-dimensional damping is underestimated, main disadvantages are involved also in terms of harvested power at all wind velocities and resistances applied, with an almost linear relation as depicted in Figure 3.42(a) (b) Figure 3.43(a) (b). It may also be noticed that an overestimated damping will result in higher power harvesting capabilities, but on the other side with a consequent possible limitation due to the higher tip displacement produced. As illustrated also in Table 3.16 the efficiency is highly compromised when the structure is highly damped and less prone to gallop, while frequency and coupling are not changed since they do not depend upon the non-dimensional damping.

Parameter: non-dimensional damping	**0,5%**	**1,0%**	**1,5%**	**2,0%**
Frequency [Hz]	18,87	18,87	18,87	18,87
U_g min. [m/s]	5,73	11,43	17,14	22,85
U_g/U_r	0,93	1,85	2,77	3,69
χ	5,11E-04	5,11E-04	5,11E-04	5,11E-04
Max. efficiency [%] range 10 : 35 m/s	0,78	0,51	0,27	0,18

Table 3.16 Effect of mechanical damping: summary results

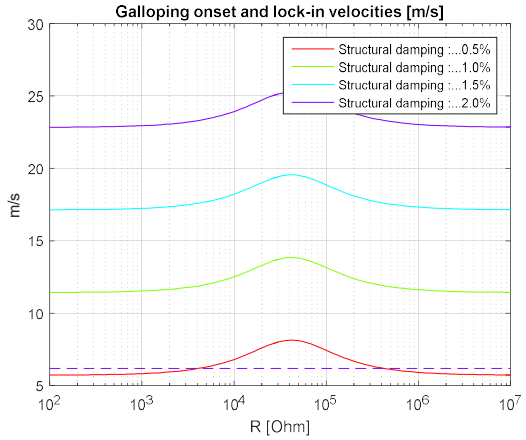

Figure 3.41 Effect of mechanical damping: galloping onset speed (continuous line) and lock-in speed (dashed line)

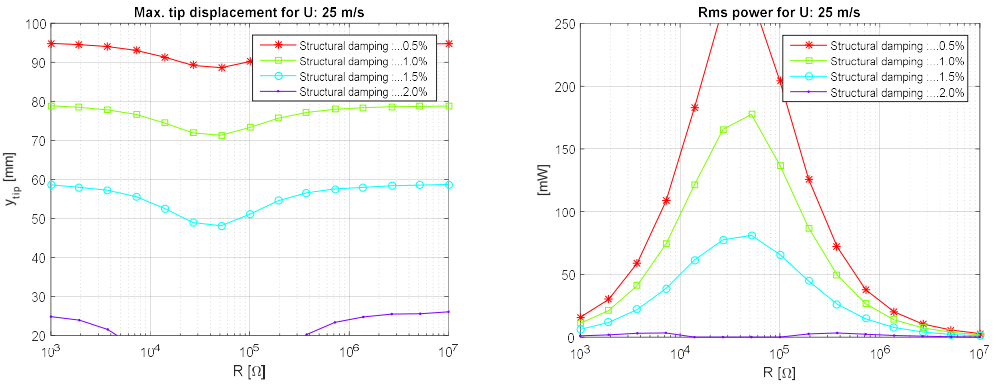

(a) (b)

Figure 3.42 Effect of mechanical damping: for the set of various resistances (a) Tip bluff body maximum displacement (b) rms power harvested during the limit cycle oscillations

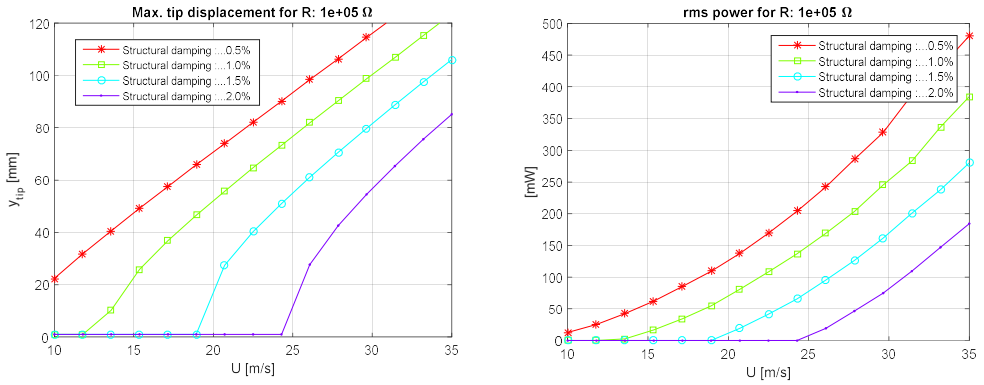

(a) (b)

Figure 3.43 Effect of mechanical damping: for the range of wind speeds considered (a) Tip bluff body maximum displacement (b) rms power harvested during the limit cycle oscillations

3.5 Optimization of the GPEH

By means of the critical analysis developed throughout this chapter it is then possible to design an optimized model of a prototype GPEH. According to the purpose of the present application it is clear that it is not sufficient to obtain the highest peak power, but to

guarantee a sufficient average power generation for a broader range of fluid velocities, where the device does not oscillate over its critical amplitude.

The onset speed is proved to be dependent upon the simplified formula in equation (3.5). Moreover, a significant role is to be related to the second region length, that lowers the onset speed as it is increased.

In order to guarantee a high electromechanical coupling for control purposes it is needed:

- a thick supporting beam, that produces an increased distance of the PZT from the neutral axes;
- a rigid bluff body and a rigid second region, by means of a short second region length and a proper material for the tip body;
- if a second region is present, the beam material should be as stiff as possible and the beam width increased in order to prevent the modal shape from being deformed mainly on the second region;
- to decrease the bluff body length, that gathers a high derivative of the modal shape at the end of the first region;
- to choose the clamping position that leave the longest part of the PZT patch exposed to vibrations;
- to select the piezoelectric model that shows the highest distance of the PZT layer from its base, and the highest volume of the piezoelectric layer volume;
- to adopt the parallel connection that has a coupling coefficient doubled with respect to the series configuration.

To obtain the highest electrical power it is needed:

- the proper bluff body length, so that the aerodynamic force is appropriately dimensioned and the electromechanical damping is not too low;
- to have a high tip mass, obtained both using a long side length ratio or a high-density material;
- to use the piezoelectric device and the clamp location and to prefer the parallel connection, that guarantee the highest electromechanical coupling;
- to choose the most efficient cross-section geometry;
- to guarantee the lowest possible structural non-dimensional damping;
- to identify the appropriate beam thickness, so that the range at which it is possible to harvest energy is kept within the application environment and the electromechanical conversion has a suitable efficiency;
- to choose a stiff material for the supporting beam

- to connect the piezoceramic to the resistance that shows the highest electrical damping.
- to appropriately increase the beam width so to have a higher conversion factor and a suitable onset speed.

In conclusion, based on the present model, it is possible to design an optimized GPEH device for the application described, that is valid as long as the quasi-steady theory is guaranteed.

4 EXPERIMENTAL VALIDATION

This chapter describes how the experimental tests were carried out in order to make a valuable comparison between measured and analytical data. First, a sequence of objectives with the relative tests is illustrated, that explains how it is possible to validate the model in all its aspects. The setups used for the tests are then described in details and the prototypes built are illustrated. The mechanical distributed model parameters are identified through free decays and sinusoidal tests with imposed motion to the base by a shaker. A validation of the electromechanical model adopted is shown with comparison of the transfer functions obtained by numerical simulations and by imposed motion tests. The aerodynamic model is then considered and the coefficient describing the galloping force are experimentally identified. The interaction with vortex shedding is studied on different prototypes and compared with other studies. Final results of a corrected model of the galloping force are shown, that prove the validity of the present work.

4.1 Objectives

The experiments presented in this chapter are aimed at the validation of the GPEH model according to the following steps:

1 - the natural frequency and the modal mass are identified from free. moreover, for same cases of interest, the experimental modal shape is obtained by tests with a shaker imposing a sinusoidal input at the first natural frequency to the base of the prototypes;

2 – the electromechanical model of the GPEH is validated through a comparison between the numerical and experimental transfer functions, giving a frequency sweep as excitation input to the base by an electromechanical shaker;

3 – the aerodynamic force model is evaluated through an experimental test campaign in a wind tunnel facility. The limit cycle oscillations at steady state are compared with the LCO characteristics predicted by the model for each prototype and for the different wind speeds. The aerodynamic coefficient a_1 is estimated by build-up tests. Moreover, a more robust estimation for both $a_1$and a_3 coefficients is set by evaluating the energy introduced by the aerodynamic force per cycle during the steady state oscillations;

4 - the obtained aerodynamic force model is then used to validate the values of power, voltage and displacement obtained for a working GPEH prototype.

According to the above-listed objectives the theory behind a galloping piezoelectric energy harvester is divided into different parts, tested almost independently, that yield to the validation of the total model proposed in this work.

4.2 Experimental setups

In this section the experimental setups used for the identification and validation procedure the facilities and tools used for testing purposes are described in details.

4.2.1 Shaker setup

The first experimental campaign is aimed at the validation of the electromechanical model presented by means of an excitation force set on the clamped base of the GPEH as depicted in Figure 4.1. In this configuration, the device has its base mounted over an electromechanical shaker. This instrument is capable of producing a sinusoidal force that acts as the input to the system and its force output depends on the voltage set at its terminals. The shaker adopted for these tests is an open-loop controlled model, meaning that no feedback law is set to control the base oscillation. In order to give a constant amplitude harmonic force the reference is divided by the square of the signal frequency. In general, the tests are carried out in a narrow range of frequencies around the first natural frequency, that represents the part of the transfer function where the other modes are less meaningful and the first mode distributed model applies. This is done by using as a reference a sweep signal, with an amplitude that changes according to the frequency applied at each time instant.

Since the voltage levels required to operate the shaker are considerably high, an amplifier is adopted in order to transform the voltage reference into a usable signal.

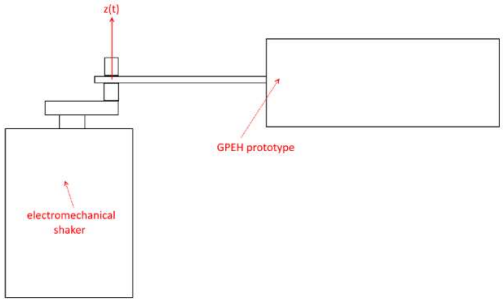

Figure 4.1 Schema for the base excitation setup

The measurements evaluated for the system are given by two accelerometers and a couple of lasers. The same model for the accelerometers A1 and A2 is chosen for its wide range and high resolution, which grant useful information up to the maximum level of oscillations of the GPEH. The lasers L1 and L2 are also installed in order to be able to reconstruct the device modal shape at various locations, without interfering with the system: the same model for both sensors is chosen so that a maximum amplitude of 10 mm can be measured for the oscillations An accelerometer would not fit for this application because its weight would alter the modal shape as it is moved along the device. Notice that the limited range for the laser sensors makes them suitable only for short tip displacements. All the main characteristics for these two types of sensor are listed in Table 4.1. The location of each sensor is shown in Figure 4.2.

	Accelerometer A1 - A2	**Lasers L1 - L2**
Manufacturer	PCB-PIEZOTONICS©	MIKROELEKTRONIK©
Family model	352A24	M7L/20
Range	±50 g	20 mm
Resolution	0.0002 g	0.9 µm
Max. output	±5 V	±10 V

Table 4.1 Main characteristics of the sensors used

The mechanical quantities of interest are measured by means of two shear accelerometers and two of laser sensors. The accelerometers are placed on the base and on the tip locations of the GPEH so that the transverse acceleration is measured. The lasers are located at the

nominal working distance from the device so that the base and the tip displacements are measured, being the lasers orthogonally incident with respect to the base and the bluff body surfaces. In order to achieve such precise positioning magnetic bases were used as shown in Figure 4.3(c). The voltage produced by the piezoelectric beam is also acquired by the DAQ. Since the voltage measured directly across the piezoceramics is predicted to be well beyond the maximum voltage measurable by the board, a voltage partitioner is implemented. The latter acts using two resistances of well separated values that are connected in series to the voltage produced by the piezoelectric patches. The voltage drop produced on the smaller resistance is then measured by the DAQ so that, depending on the ratio between the two resistances, it is possible to reconstruct the voltage original value. For the purpose of this research a ratio of 1:100 is found sufficient to cover all possible cases under investigation, without any apparent loss in accuracy.

As for the setup presented, the following acquisition chain exists:

- inputs and outputs cables are linked to the acquisition board;
- a PC is used to read and store the data from the DAQ, as well as to provide the appropriate reference signal for the electromechanical shaker;
- the reference signal for the shaker is sent from the DAQ to the amplifier;
- the amplified signal is connected to the electromechanical shaker terminals, to provide adequate input force.

The acquisition system inputs are the voltages produced on the piezoceramics, the acceleration and the displacements of the tip and base locations. The only output is instead the reference signal for the shaker. The sensors are cabled with PCB wires that are secured to steady locations in order to avoid damping effects. These measures together with the input to the amplifier are logged to or from an acquisition system board that communicates with a PC.

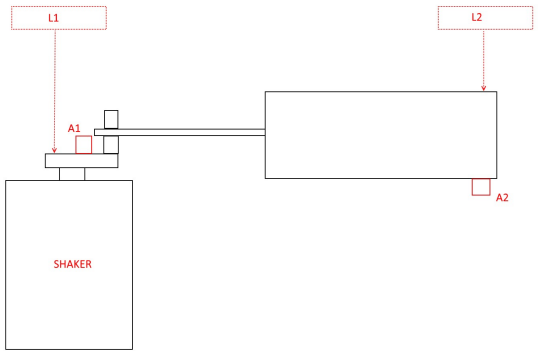

Figure 4.2 Schema of sensors locations

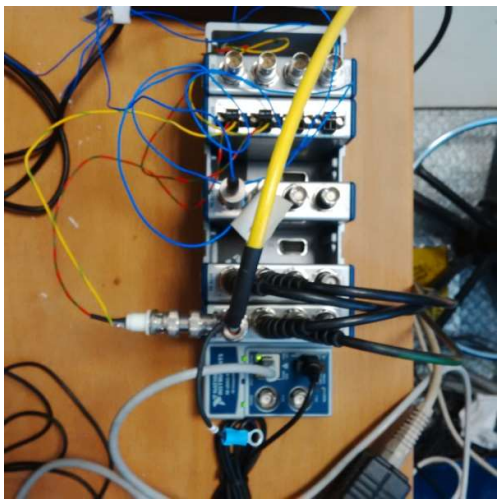

(a)

(b)

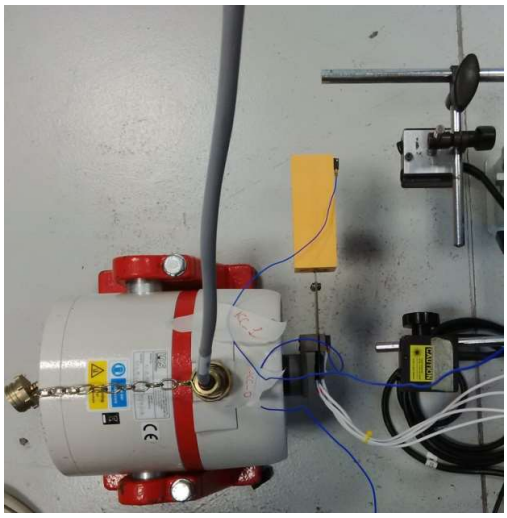

(c)

(d)

Figure 4.3 Base vibration setup: (a) Data Acquisition System (b) Amplifier (b) Electromechanical shaker and instruments(d) Personal Computer

4.2.2 Wind tunnel setup

The wind tunnel is the environment aimed at reproducing the galloping behavior under study. This objective is achieved by producing different wind speeds in a proper facility, where the fluid characteristics are uniform and under control. Two wind tunnels are used during the following experiments that were chosen according to the specific dimensions of each prototype. The main characteristics are reported in Table 4.2, where W1 represents the smaller facility and W2 the bigger wind tunnel. For this configuration, the GPEH prototype is clamped on the floor or ceiling of the wind tunnel section and the tip acceleration is accessed by means of a shear accelerometer. The voltage produced by the piezoelectric patches is measured using the same technique described for the shaker excitation setup. The photograph in Figure 4.4(a) shows the small wind tunnel, with the clamped prototype, while picture in Figure 4.4(b) depicts the larger wind facility adopted.

	Wind tunnel W1	**Wind tunnel W2**
Type	open-jet	closed-jet
Section width x height	150 x 200 mm	1.5 x 1 m
Max wind speed [m/s]	40	55
Boundary layer [mm]	na	35
Control	open-loop	open-loop
Clamp position	ceiling	floor
Location	*Politecnico di Milano,* *Dipartimento di Ingegneria Aerospaziale (DIA)*	

Table 4.2 Properties listed for the wind tunnel facilities used

(a)

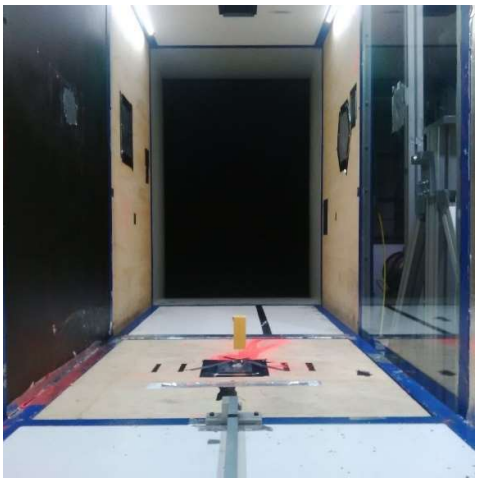

(b)

Figure 4.4 (a) wind tunnel W1 (b) wind tunnel W2

Both the wind tunnels are controlled in open loop by means of the power given to the rotor and the wind velocity obtained is measured using a pair of pitot tubes, with proper application of the blockage correction explained in paragraph 0. The data are logged to and the wind speed controlled by a PC connected to an acquisition board as shown in Figure 4.5(a). The differential pressure is measured using the pressure sensor in Figure 4.5(b), from which the wind tunnel speed measure is achieved.

(a)

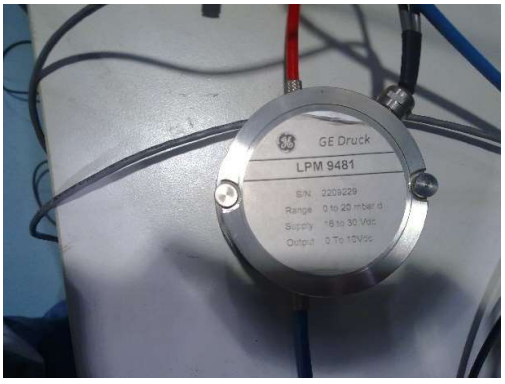

(b)

Figure 4.5 (a) Acquisition system used (b) pressure sensor employed

4.3 Prototypes realized

In this section the prototypes realized to validate the model are presented with the geometrical details of their construction and the illustration of the main characteristics. All the prototypes were realized with a harmonic steel supporting beam and a resin square bluff body with side dimension equal to 40 mm, as shown in Figure 4.6(a). The bluff body is made up of two parts that are glued on the supporting beam as depicted in Figure 4.6 (b). The clamping system is mainly composed of two steel parts that secure the device with screws.

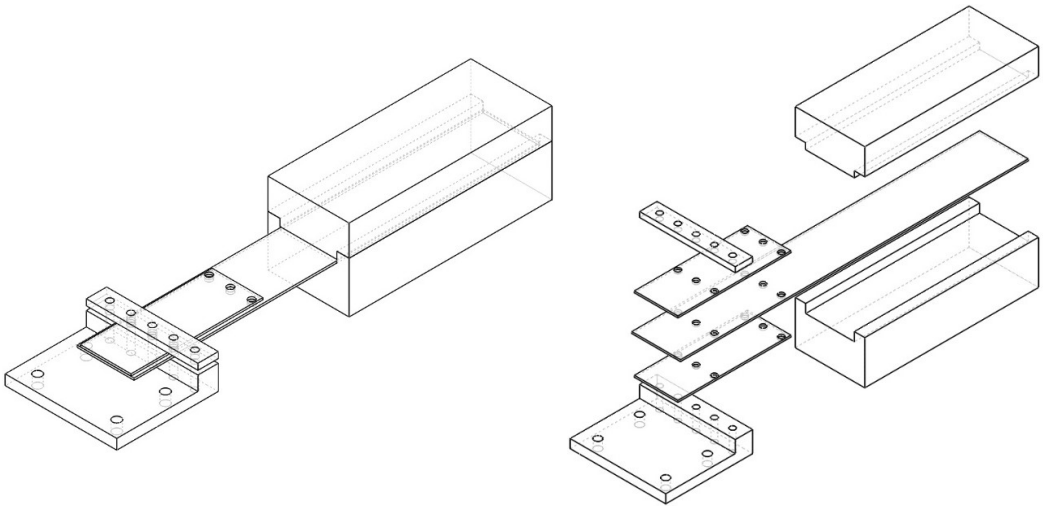

(a) (b)

Figure 4.6 General structure of the prototypes realized (a) assembled prototype view (b) exploded view

The first prototype realized (prot. B) is found not to undergo the galloping instability. Other versions of this model are then compared, so that it is discovered that the instability can be triggered for a lower non-dimensional damping or a longer bluff body. Since the assumption of a bi-dimensional flow stream is not consistent with this first prototype, a second device is built, with a longer bluff body (prot. D). In this way, it is to compare the meaningfulness of the three-dimensional effects. The main characteristics are reported in Table 4.3; notice that the non-dimensional damping is derived from an estimation procedure that will be further explained.

Prototype B

This GPEH is made of a supporting steel beam of thickness 0.5 mm and width 28 mm, that goes along the entire device. A bluff body is realized with a total length of 100 mm and a side

dimension of 40 mm. The bluff body material adopted is a very low density resin and gives the body a total tip mass of 21 g. Two piezoceramics are screwed on the supporting beam and the model PPA1011 is used for both sides in a "clamp 0" configuration. A picture of the model is shown in Figure 4.9(a). The technical drawings are shown in Figure 4.7 and Figure 4.8.

Prototype B-

This variant of prototype B is realized simply detaching the piezoelectric patches from the supporting beam.

Prototype B+

This prototype is realized from prototype B thanks to the use of a special damping patch that is attached to both sides of the supporting beam instead of the piezoceramics. In this way the same device can be tested as if it had a major damping.

Prototype B++

As in B+ there is a special damping patch attached, but this time the thickness of this layers is doubled with an increased damping effect on the system with respect to the previous case.

Prototype B++ext.

The prototype B++ is modified with the attachment of an extension to the bluff body. The latter is realized with a polystyrene extension of length equal to 100 mm as depicted in Figure 4.9(c).

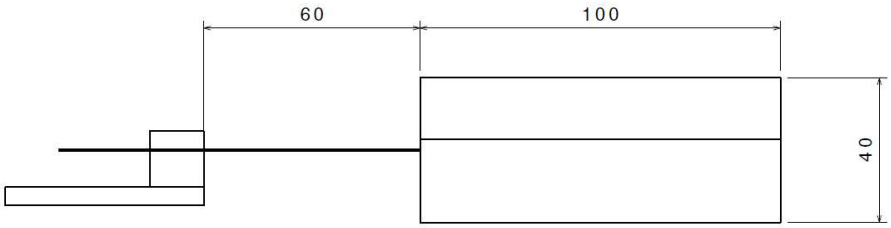

Figure 4.7 Prot. B: lateral view (dimensions in mm)

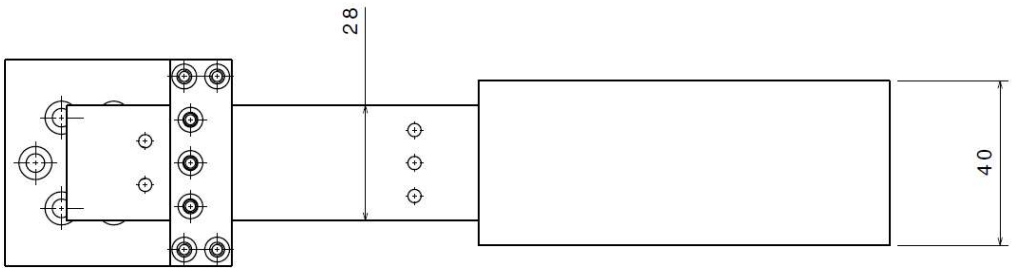

Figure 4.8 Prototype B: top view (dimensions in mm)

Prototype C

The results obtained for this prototype are shown in the following only in support to the conclusions drawn. It is represented in picture Figure 4.9(b), even if the data are not reported for the sake of brevity.

Prototype D

The realized model is represented in Figure 4.9(d). It employs a beam such as the one of prot. B, over which only one PPA1001 piezoceramic is glued. The bluff body is composed of two parts: a 100 mm long part which is made of the same material of prot. B body and a long extension in polystyrene of length 300 mm. The overall prototype is 440 mm long. The clamp adopted for the piezoceramic is “clamp 0”.

Prototype D+m

In this case a tip mass is attached to the model described as prot. D. in order to achieve a higher Scruton number. The additional tip mass used is a coin which weights 7.5 g and is shown in Figure 4.9(e).

Clamping system

The clamping system is composed of two steel plates that secures the piezoelectric patches and the supporting beam at the appropriate clamp location by means of screws. A representative clamping is shown in Figure 4.9(f).

	B	**B-**	**B+**	**B++**	**B++ext**	**D**	**D+m**
modal mass [g]	12.9	14.7	14.7	14.7	8.4	7.5	16.5
h	0.7 – 1.3	0.2%	0.6%	1.3%	1.8%	2.3%	2.3%
L_2 **[mm]**	25	25	25	25	25	20	20
L_3 **[mm]**	100	100	100	100	100	100	100
L_4 **[mm]**	no	no	no	no	100	300	300
D **[mm]**	40	40	40	40	40	40	40
U_g **[m/s]**	18.7	1.6	4.5	10.0	2.9	1.73	2.27
U_r **[m/s]**	6.0	2.9	2.9	2.9	2.28	2.56	1.49
U_g/U_r	3.0	0.5	1.5	3.29	1.29	0.6	1.5
Scruton number	29.0	5.1	14.1	30.9	12.1	3.3	7.6

Table 4.3 Main characteristics for the prototypes realized

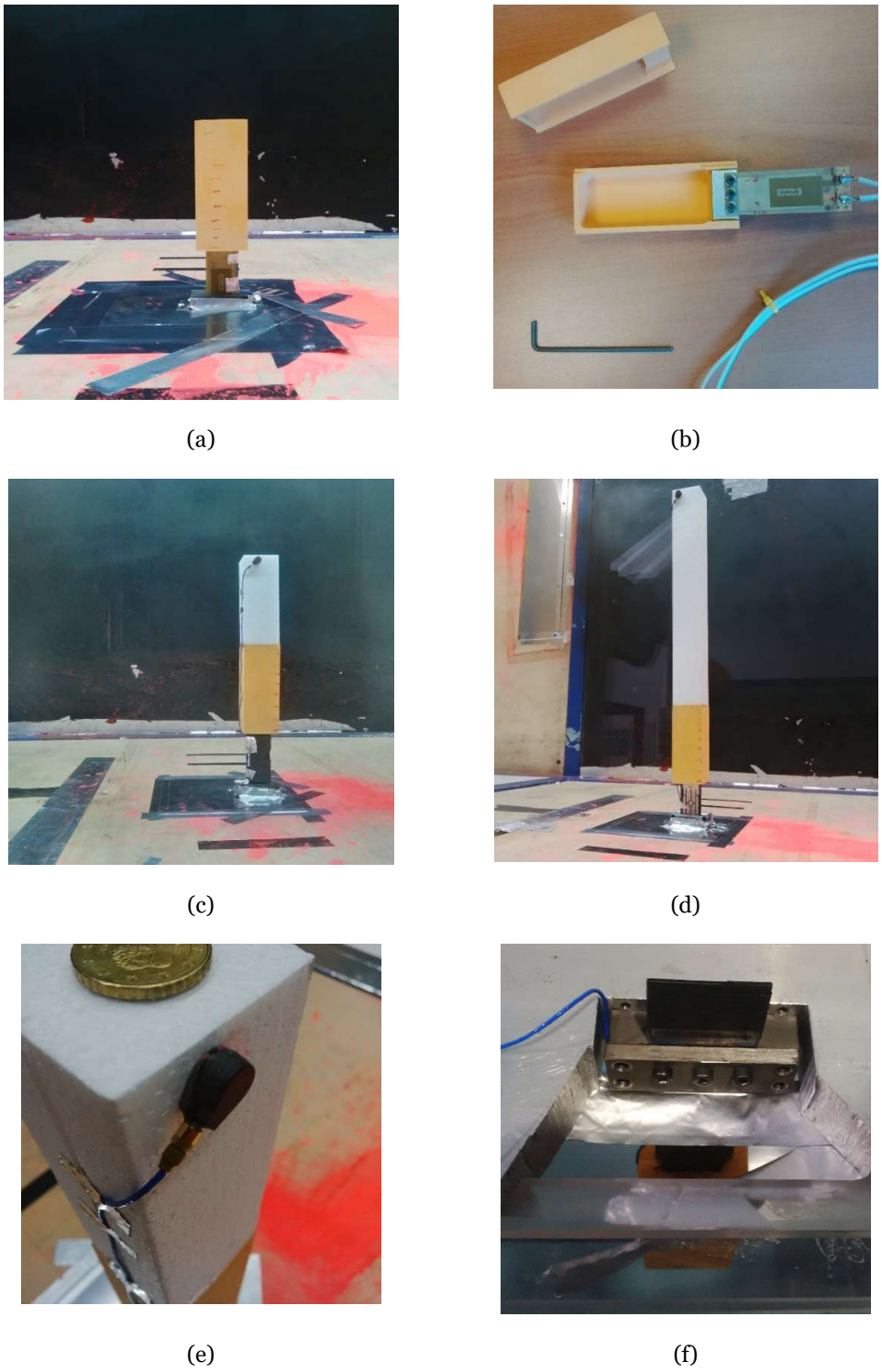

(a) (b)

(c) (d)

(e) (f)

Figure 4.9 Prototypes realized (a) Prototype B (b) Prototype C (c) Prototype B++ext. (d) Prototype D (e) Prototype D+m (f) Clamping system for W1

4.4 Numerical transfer functions for the imposed motion tests

This section explains how to obtain the transfer functions needed to describe the model from a mechanical and electrical point of view. The starting point is the system of equations obtained at the end of Chapter 2. These transfer function are important for the successive validation of the model with the experimental results.

The system of equations (2.108) obtained for the non-linear coupled distributed model is here recalled for the parallel case, written according to Laplace:

$$\begin{cases} M^* s^2 q + R^* s q + K^* q + \chi_p V_p = F^* \\ \dfrac{V_p}{R} + C_p s V_p - \chi_p s q = 0 \end{cases} \tag{4.1}$$

where the force due to the aerodynamic effect F^* is null and the only contribution is due to the forced motion. When the input force is derived from a base excitation one can assume that there is a superimposition of the first mode of vibration of the beam and one forced translation given by the amplitude and frequency of the shaker input. The translational displacement, see Figure 4.10, can therefore be rewritten for each region as:

$$\begin{aligned} y_{1_{new}}(x,t) &= y_1(x,t) + z(t) \\ y_{2_{new}}(x,t) &= y_2(x,t) + z(t) \\ y_{3_{new}}(x,t) &= y_3(x,t) + z(t) \\ y_{4_{new}}(x,t) &= y_4(x,t) + z(t) \end{aligned} \tag{4.2}$$

where $z(t)$ is the forced oscillation of the base that in the case considered takes the following form:

$$z(t) = \mathrm{Z}_0 \cos(\Omega t) \tag{4.3}$$

where Ω is the frequency and Z_0 the amplitude of the harmonic motion. The

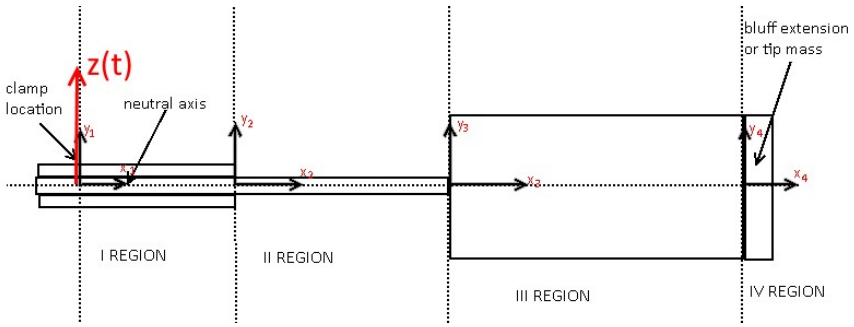

Figure 4.10 Regions considered in the GPEH model and forced motion by the shaker

The kinetic energy computed in equation (2.54) is then rewritten with the use of the new variables as in:

$$E_k = \frac{1}{2}\int_{V_{s1}} \dot{y}_{1_{new}}{}^T \rho_s \dot{y}_{1_{new}} dV + 2\frac{1}{2}\int_{V_{p1}} \dot{y}_{1_{new}}{}^T \rho_p \dot{y}_{1_{new}}\, dV + \frac{1}{2}\int_{V_{s2}} \dot{y}_{2_{new}}{}^T \rho_s \dot{y}_{2_{new}}\, dV + \int_{V_{s3}} y_{3_{new}}{}^T \rho_s \dot{y}_{3_{new}}\, dV + \frac{1}{2}\int_{V_{b3}} \dot{y}_{3_{new}}{}^T \rho_b \dot{y}_{3_{new}}\, dV \quad \frac{1}{2}\int_{V_e} \dot{y}_{4_{new}}{}^T \rho_e \dot{y}_{4_{new}}\, dV \tag{4.4}$$

With a similar procedure to the one described in the second chapter the integrals are simplified and the kinetic energy is derived with respect to $\delta\ddot{q}$, so to obtain:

$$\delta E_c = \delta\dot{q} M^* \dot{q} + \delta\dot{q} m^* \dot{z} \tag{4.5}$$

where the first term is the same as the one obtained in the previous case, while the second term is the result of the forced motion and m^* is represented by the following integrals:

$$m^* = \int_0^L m_1\phi_1\, dx_1 + \int_0^{L_2} m_2\phi_2\, dx_2 + \int_0^{L_3} m_3\phi_3\, dx_3 + \int_0^{L_4} m_3\phi_4\, dx_4 \tag{4.6}$$

The overall system is then described by the following equations:

$$\begin{cases} M^*\ddot{q} + R^*\dot{q} + K^* q + \chi_p V_p = -m^*\ddot{z} \\ \dfrac{V_p}{R} + C_p\dot{V}_p - \chi_p\dot{q} = 0 \end{cases} \tag{4.7}$$

The relation between the modal coordinate and the voltage can be obtained by the second equation in system (4.1) as:

$$V_p = \frac{s\chi_p}{\frac{1}{R} + C_p s} q \tag{4.8}$$

that is represented in Figure 4.11(a). The transfer function from the base acceleration to the tip acceleration is obtained by substituting the relation (4.8) in the first equation of system (4.7) and it is obtained:

$$\frac{\ddot{y_{tip}}}{\ddot{z}} = \frac{-m^* s^2 \left(\frac{1}{R} + C_p s\right) \phi_3(L_3)}{M^* \left[\left(\frac{1}{R} + C_p s\right)(s^2 + 2h\omega_0 s + {\omega_0}^2) + \frac{s{\chi_p}^2}{M^*}\right]} \tag{4.9}$$

This transfer function is illustrated in Figure 4.12(b). Another mechanical transfer function that can be evaluated in a similar way is the one from the base acceleration to the tip displacement and it is shown in Figure 4.12(a). The transfer function from the base acceleration to the output voltage is similarly obtained as:

$$\frac{V_p}{\ddot{z}} = \frac{-s\chi_p m^*}{M^* \left[\left(\frac{1}{R} + C_p s\right)(s^2 + 2h\omega_0 s + {\omega_0}^2) + \frac{s{\chi_p}^2}{M^*}\right]} \tag{4.10}$$

and it is represented in Figure 4.11(b) for the case of prototype B (the non-dimensional damping is assumed to be 1%).

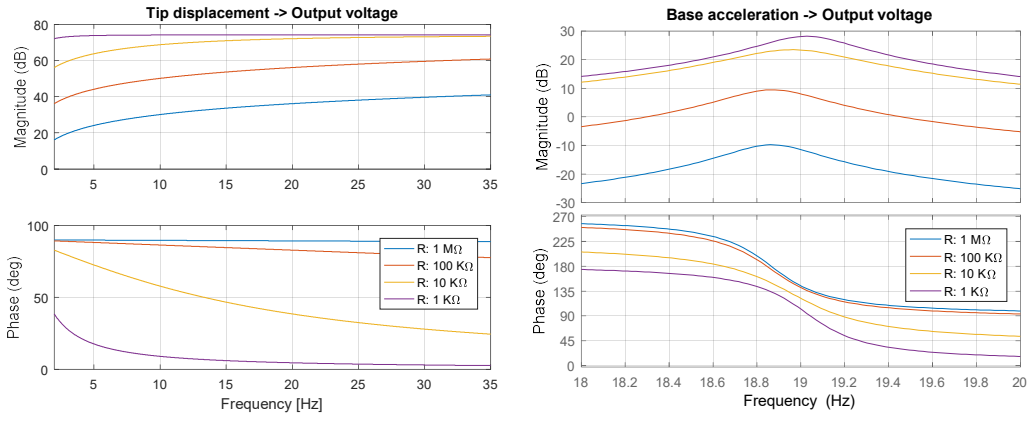

(a) (b)

Figure 4.11 Transfer function (a) Tip displacement to output voltage (b) Base acceleration to output voltage

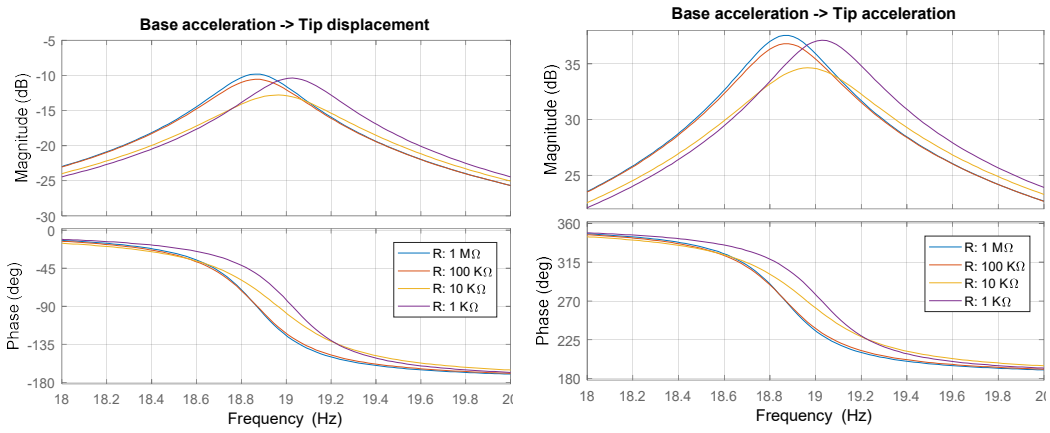

(a) (b)

Figure 4.12 Transfer function for (a) Base acceleration to tip displacement (b) Base acceleration to output voltage

4.5 Electromechanical model validation

The parameters that describe the electromechanical part of the model are estimated and compared with the predictions. An identification procedure is first set for the non-dimensional damping, considering the possible non-linearity due to the resistances connected or the amplitude of oscillations by motion imposed tests. The electromechanical coupling parameter is experimentally identified from the frequency obtained in free decay tests for short circuit and open circuit connections. The capacitance is retrieved from the analysis of the experimental transfer functions from tip displacement to output voltage for different resistances. With the identified parameters, the experimental and predicted transfer functions are compared to provide the validation of the model, in terms of output voltage over acceleration input. Notice that with this approach, once the connected resistance R is known, all the parameters C_p, χ_p, h, ω and M^* that describe the model in system of equations (2.108) are separately identified.

4.5.1 Modal distributed parameters model validation

The first verification of the model is done by comparing the frequency obtained by a numerical model and the one resulting in a free decay oscillation of the clamped model. These tests are carried out having a short-circuit connection, so that the coupled electrical

term in the first equation of system (2.108) is null; the frequency detected is therefore related only to the mechanical part of the system. For the low levels of electromechanical damping considered in the various prototypes, the effect that a different resistance has on the natural frequency is microscopic, as it will be proven by the experimental transfer functions. The results of the identification are shown in Table 4.4. It is found that the accuracy of the estimations is reduced for the prototypes D and D+m, as the assumption of an infinitely rigid body is no longer verified for the polystyrene extension attached.

Prototype	**B**	**B-**	**D**	**D+m**
Numerical frequency (I mode) [Hz]	18.5	9.4	6.5	5.5
Experimental frequency (I mode) [Hz]	18.4	9	7.9	4.5

Table 4.4 Comparison between experimental and numerical frequency

An ulterior proof is given by the modal mass verification. This test was carried out using an added mass on the top of the bluff body. By assuming that the stiffness k of the device is not changed by the mass increase, one can identify the modal mass M^* of the prototype from the following relations:

$$\omega = \sqrt{\frac{k}{M^*}} \tag{4.11}$$

$$\tilde{\omega} = \sqrt{\frac{k}{M^* + \Delta m}} \tag{4.12}$$

where $\tilde{\omega}$ and ω are respectively the measured frequencies of the device with and without the added tip mass, which is defined as Δm. Since the modal mass is the only unknown for the latter equations, it is easy to obtain it as:

$$M^* = \frac{\Delta m\, \tilde{\omega}^2}{\omega^2 - \tilde{\omega}^2} \tag{4.13}$$

Coins were used in all cases of a weight appropriate to the prototype selected. Results are listed in Table 4.5 for the main cases treated. It is noticed that the percentage errors of the estimation are bigger for the prototypes where the frequency predicted was more mismatched (prot.s D and D+m).

Prototype	B-	D	D+m
Numerical modal mass [Kg]	0.0147	0.0075	0.0165
Model mass identified [Kg]	0.0163	0.0060	0.0135

Table 4.5 Modal mass comparison between numerical simulation and experimental tests

As can be seen from both the comparison of modal mass and frequencies the simulations are in good agreement with the experimental data, meaning that the simulations can predict the actual mechanical behavior of the device.

The second mode of vibration can be verified by evaluating the FRF from base acceleration to tip acceleration, performing an imposed motion test with a long frequency sweep. As expected from the theory, the second mode appear at a frequency very high with respect to the first one as depicted in Figure 4.13. The numerical values predicted with the model are compared with the ones identified from the transfer functions as reported in Table 4.6. Poor agreement is found and even if the second mode appears at a lower frequency than expected, this is sufficiently high with respect to the first one to conclude that it has no direct influence on the rest of the model, so that the hypothesis can be verified.

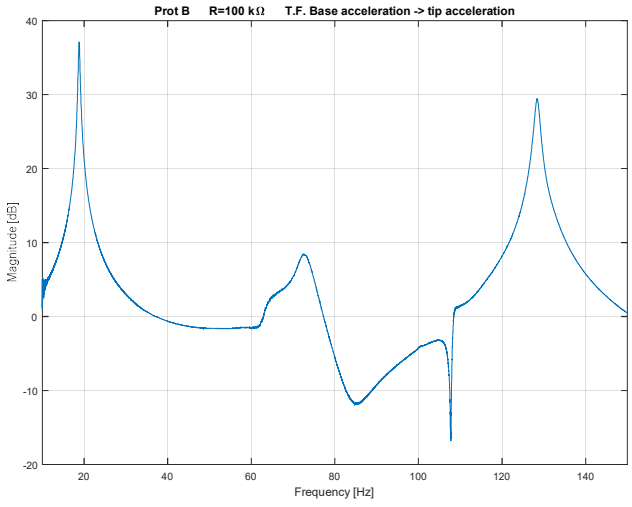

Figure 4.13 Prototype B, resistance 100 kΩ: magnitude of the FRF from base acceleration to tip acceleration

Prototype	**B**
Numerical II mode frequency [Hz]	183.76
Experimental II mode frequency [Hz]	128.20

Table 4.6 Comparison of numerical and identified second mode frequencies

The error that is more relevant, both for the first and second modal frequencies, is for the case of prototype C, for which an ulterior analysis has been carried out during the base vibrations campaign by means of a verification of the modal shape. The numerical modal shape is compared with the experiments in which the displacement is measured at different locations along the axial coordinate of the beam. The peaks of the transfer function from base to tip displacement for the different locations are then considered as the first mode of vibration response of the system and are therefore mapping the modal shape along the axial direction. Therefore, these values, normalized with respect to the highest and multiplied for the value of the modal shape in the location of the highest measure are compared to the numerical modal shape as in Figure 4.12. The agreement is sufficiently good to conclude that each region has a behavior similar to the one expected.

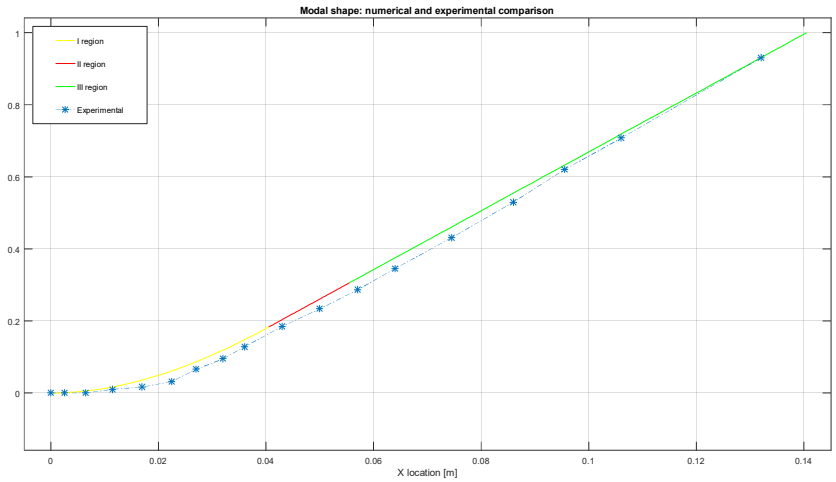

Table 4.7 Experimental and numerical modal shape comparison for prototype C

4.5.2 Electromechanical coupling parameter

If the case of a short circuit and an open circuit are analytically considered for the system presented, an experimental expression can be found in order to identify the electromechanical coupling. Going back to system of equations (2.108) one can write the first equation using the polar representation for the mechanical poles, obtaining:

$$\begin{cases} M^*(\ddot{q} + 2h\omega_0\dot{q} + {\omega_0}^2 q) + \chi_p V_p = F^* \\ \dfrac{V_p}{R} + C_p\dot{V}_p - \chi_p\dot{q} = 0 \end{cases} \tag{4.14}$$

If the short circuit case, with empirical frequency ω_{sc}, is considered, one can solve the first equation neglecting the coupling term since the voltage is constrained to zero:

$$M^*(\ddot{q} + 2h\omega_0\dot{q} + {\omega_0}^2 q) = F^* \tag{4.15}$$

and it is seen that the frequency of the GPEH is identical to the natural frequency $\omega_{sc} = \omega_0$

In the open circuit case, instead it is more convenient to start from the set of equations (2.105), that are rewritten for the parallel connection as in:

$$\begin{cases} M^*(\ddot{q} + 2h\omega_0\dot{q} + {\omega_0}^2 q) + \chi_p V_p = F^* \\ -C_p V_p + \chi_p q = Q_{el} \end{cases} \tag{4.16}$$

Since the current is forced to be zero in this configuration one can state that $Q_{el} = 0$ and the second equation becomes:

$$V_p = \frac{\chi_p q}{C_p} \tag{4.17}$$

If the latter expression is substituted in the first equation it is obtained:

$$M^*(\ddot{q} + 2h\omega_0\dot{q} + {\omega_0}^2 q) + \chi_p \frac{\chi_p q}{C_p} = F^* \tag{4.18}$$

It is then possible to state that the overall frequency of the open circuit configuration is:

$${\omega_{oc}}^2 = {\omega_0}^2 + \frac{\chi_p}{C_p M^*} \tag{4.19}$$

And the final expression for the identified electromechanical coupling is:

$$\chi_p = \sqrt{({\omega_{oc}}^2 - {\omega_0}^2) C_p M^*} \tag{4.20}$$

The expression coincides with the one used also by Zhao et al. [4].

As the open circuit and short circuit frequencies are retrieved from a free decay on the opportunely connected system the identified electromechanical coupling can be calculated. The matching between empirical and numerical values for this parameter are shown in Table 4.8, where a good agreement can be found for prot. B and C, which proves the validity of the method used for the evaluation of the electromechanical coupling. The huge discrepancy found in prototype D is given by two main reasons. The first is that the assumption of a perfectly rigid bluff extension is not achieved using a polystyrene body and therefore the modal shape is changed, diminishing the level of strain at the end of the piezoelectric layer. A second reason is that, after curing, the glue employed for this prototype formed a non-negligible layer with thickness 0.1 mm, that shortened the distance between the neutral axis and the PZT layer. For the combination of both these effects, the power harvested from prot. D and D+m are well below the predicted values.

Prototype	**B**	**C**	**D**
Empirical χ	6.19E-4	2.80E-4	1.0E-5
Numerical χ	5.99E-04	2.20E-04	1.7E-4

Table 4.8 Comparison between numerical and empirical values for the electromechanical coupling

4.5.3 Non-dimensional damping

Before being able to make a comparison with the experimental data, the non-dimensional damping for the prototype under study must be identified, in order to complete the model parameters. This estimation is first carried out by looking at the free decay of the system. From this test a first insight is given on the damping behavior, that is found to be highly dependent on the amplitude of oscillation considered, being higher for the biggest oscillations. The non-dimensional damping is then evaluated from the transfer function from base acc. to tip acc. at the first resonance using the forced motion setup. Various tests are repeated at different acceleration levels of the forced input and the resulting FRFs are similar to the one reported in Figure 4.14 for prototype B. The results are estimated according to the phase derivative method reported in equation (8.31) in [60], according to which the non-dimensional damping is:

$$h = -\frac{1}{\omega_n \left|\frac{\partial \phi(\Omega)}{\partial \Omega}\right|} \tag{4.21}$$

where $\frac{\partial \phi(\Omega)}{\partial \Omega}$ is the phase derivative (expressed in rad) of the transfer function from base acceleration to tip acceleration in correspondence to the resonance frequency ω_n. The identified non-dimensional damping for this prototype varies in the range 0.71 – 1.13 %. To provide an ulterior evidence, the resulting identified non-dimensional damping is shown also for another prototype realized (prot. C), for which a more detailed estimation has been carried out at various resistances and amplitudes, see Figure 4.15. Prot. C was realized with a single piezoelectric layer and a bluff body with comparable dimensions to prot. B. It is meaningful to notice that the highest damping is in correspondence to the resistance that shows the best electrical power conversion. The trend can be in first approximation be assumed linear with the level of oscillation.

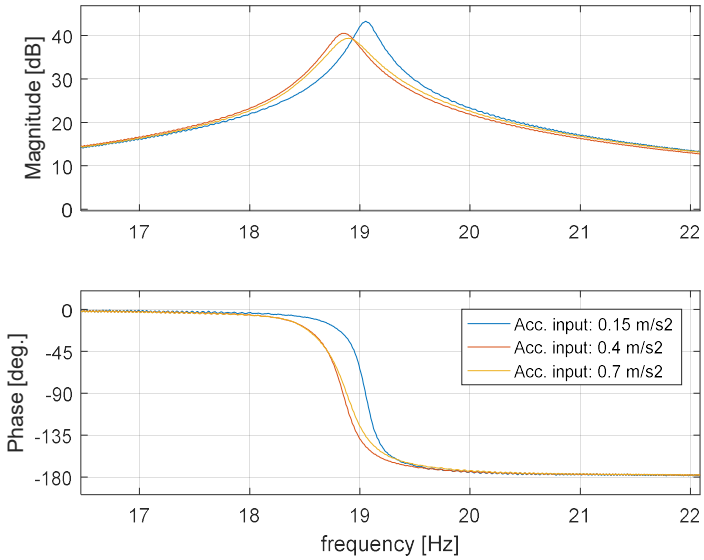

Figure 4.14 Prototype B, resistance 1 MΩ: transfer function from base acceleration to tip acceleration

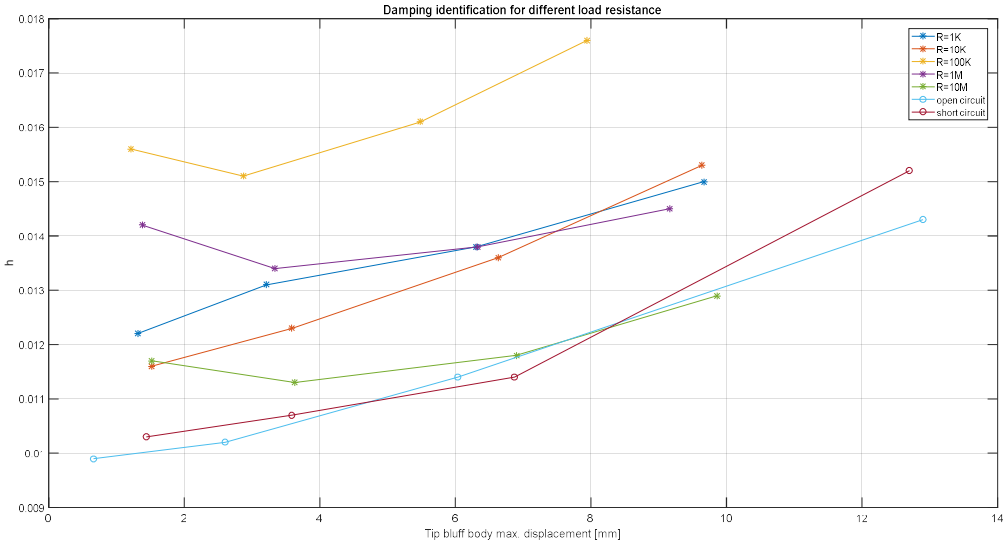

Figure 4.15 Prototype C: results of the non-dimensional damping for at different tip displacement and for various resistances connected to the PPA1011

In order to explain the origin of the nonlinear behavior of the system, an ulterior test campaign is dedicated to a single PPA1011 device, clamped on the same vibrational setup and provided with an end mass of weight approximately 14 g. The same procedure is followed for this configuration and the results for the short circuit connection are reported in Figure 4.16. The graph clearly prove that the non-linearity is related to oscillation level reached by the piezoceramic and that a very high non-dimensional damping can be found for the highest amplitude reached. Notice that in this case the PZT layer was subject to oscillations amplitude much higher than the that can be experienced if it is fixed on the GPEH prototypes realized. Another remark is that the real damping of the system is given by the relation $r = h2M^*\omega$, so that it strictly depends on the modal mass and frequency of the system.

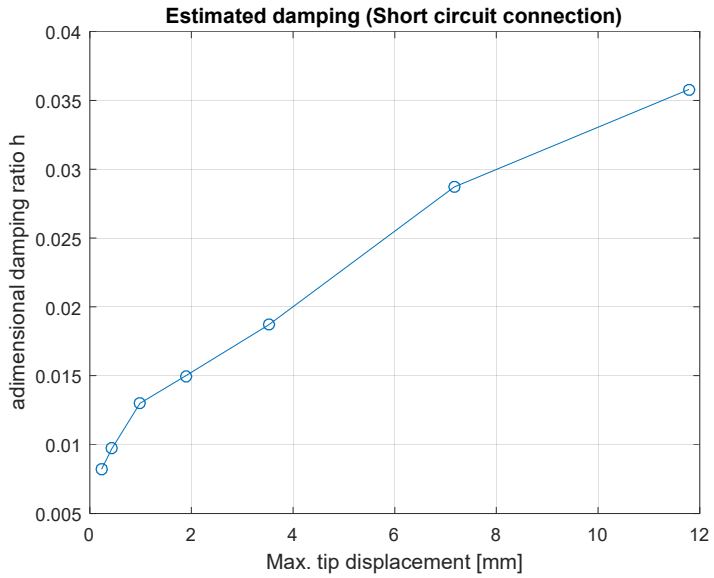

Figure 4.16 PPA1011 device, short circuit connection, non-dimensional damping estimated

As the model developed for the GPEH does account for a constant non-dimensional damping, the results obtained in this preliminary phase are used to retrieve an average value for the level of oscillation considered. The validation presented in the following section is developed by means of average values of the non-dimensional damping selected for each prototype. It is also meaningful to notice that the researches cited in this work did not develop a model able to consider the structural non-linearity. For the aerodynamic simulation proposed in the next section, a different model is implemented, that accounts for a linear dependence of the non-dimensional damping over the amplitude reached.

4.5.4 Capacitance parameter

As stated with relation (4.8), the transfer function from tip displacement to output voltage is described by a 1-pole 1-zero transfer function. Therefore, it is simple to identify the parameter C_p (capacitance), for different known resistances R, as the pole is located in $s = -\frac{1}{RC_p}$. Tests are performed with forced motion input for a short range of frequency centered on the natural frequency for a set of resistances. The piezoceramics are acquired separately and connected to the same load. From the experimental measures a numerical transfer function is estimated, having one pole and one zero. The identified value of the capacitance is retrieved from the denominator and results are listed in Table 4.9. It is noticed that the estimation has a better approximation as the resistance applied moves the pole closer to the range of frequencies tested. The capacitance identified for the test that has the best fit is in perfect correspondence to that declared by the manufacturer.

Resistance	Identified T.F.	Pole [Hz]	Identified C
1 kΩ	$\frac{-23.68s + 2.07E5}{s + 6402}$	1019.1	1.6E-07
10 kΩ	$\frac{3832s + 1.21E4}{s + 1328}$	211.8	7.5E-08
100 kΩ	$\frac{3973s + 479.2}{s + 99.92}$	15.8	1.0E-07
1 MΩ	$\frac{3943s + 90.77}{s + 13.29}$	2.1	7.5E-08
10 MΩ	$\frac{3673s + 50.4}{s + 6.27}$	1.0	1.6E-08

Table 4.9 Transfer function identified from tip displacement to output voltage for different resistances connected

4.5.5 Prot. B: validation results

Test results for the experimental-numerical validation of prototype B are shown in the following figures for different resistances applied. First, the mechanical transfer function from base acceleration to tip acceleration is shown in Figure 4.17. The matching is very good for the phases of the experimental and numerical data, with a small gap between the two lines that is caused by the different frequency derived via analytical methods. The transfer function magnitudes are well matched in the narrow range of the first resonance, while before and after the difference grows as the frequency is far from the first mode one. This is in agreement with the fact that the numerical mode describes only the first mode behavior of the system, while the experimental mode is subject to the cumulative action of all the modes. The other modes are present at higher frequencies than that of the first mode and therefore they act in phase with the first mode until the first resonance is exceeded. After this point the first mode has a phase opposite to that of the others and therefore the contributions of the other modes are to be subtracted from the first mode. This phenomenon is observed in the magnitude of the graphs presented: the numerical transfer function underestimates the real motion before the first resonance, while it overestimates it beyond the first mode frequency.

The transfer function between the tip displacement and the voltage output is shown in Figure 4.18. The agreement between the numerical and experimental phases is very good for all the resistances considered. The experimental phase is also used to estimate the value of the piezoelectric capacitance. In fact, as found in expression (4.8), the transfer function considered has only one pole located in $s = -1/RC_p$. If the experimental data are used to

identify the pole location with an identification procedure, then it is directly estimated the value of the piezoelectric capacitance for each resistance. This method provides a perfect agreement with the capacitance declared by the manufacturer. For what concerns the magnitude of the transfer function, this presents a significant mismatch for the range of frequencies below the first resonance.

As a last validation, the transfer functions between base excitation amplitude and voltage output are described in Figure 4.19. As for the other cases, the phases are well lined up for the experimental and numerical results: the effect of the third pole is clear especially in Figure 4.19**Errore. L'origine riferimento non è stata trovata.**(d), where the initial phase is decreased by 90° more with respect to the other configurations. The magnitude of this transfer function appears to be overestimated by 10 dB for all frequencies and resistances.

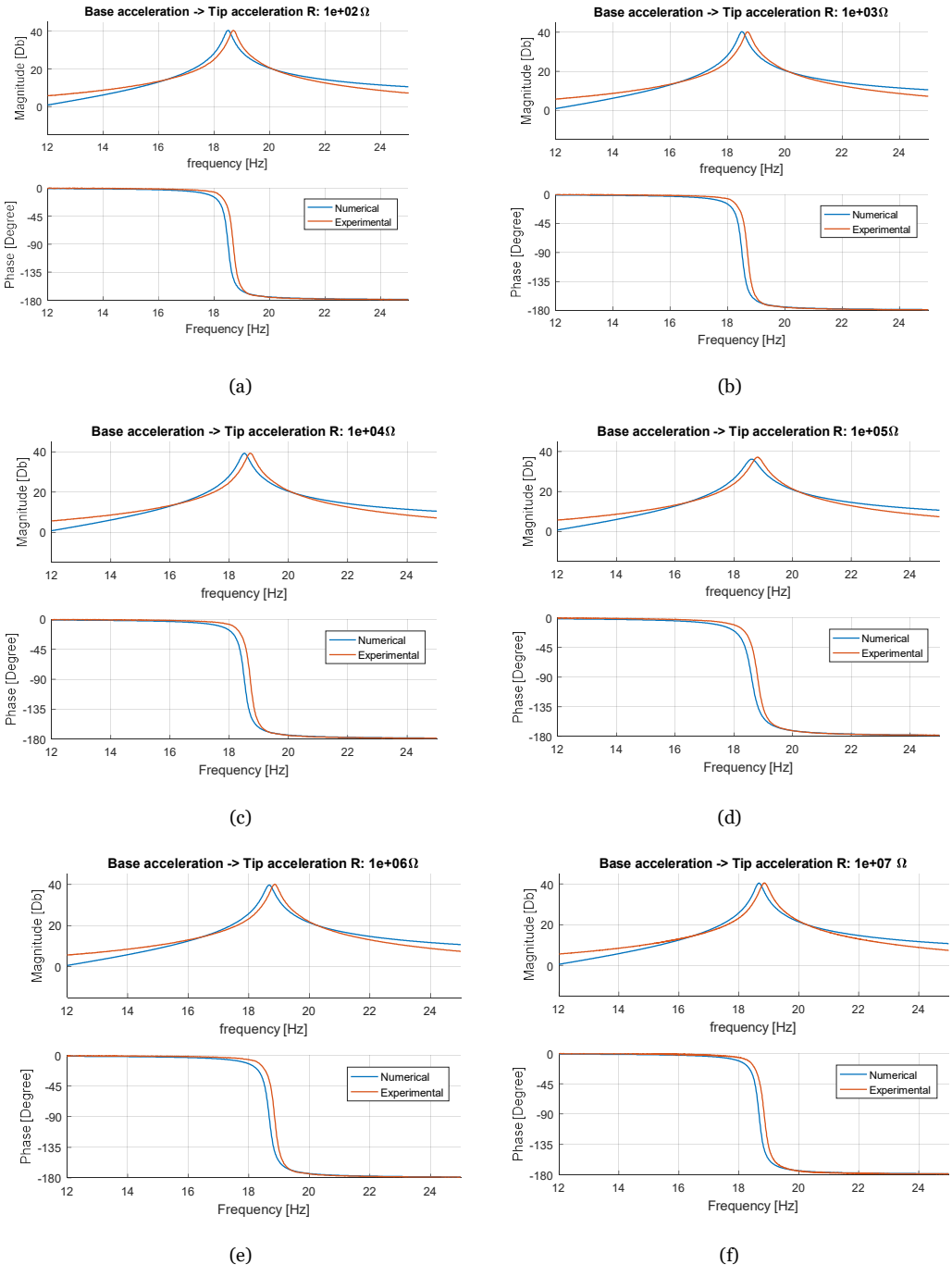

Figure 4.17 Prot. B: transfer functions from base acceleration to tip acceleration compared with experimental results for (a) R=10 Ω (b) R=1 kΩ (c) R=10 kΩ (d) R=100 kΩ (e) R=1 MΩ (f) R=10 MΩ

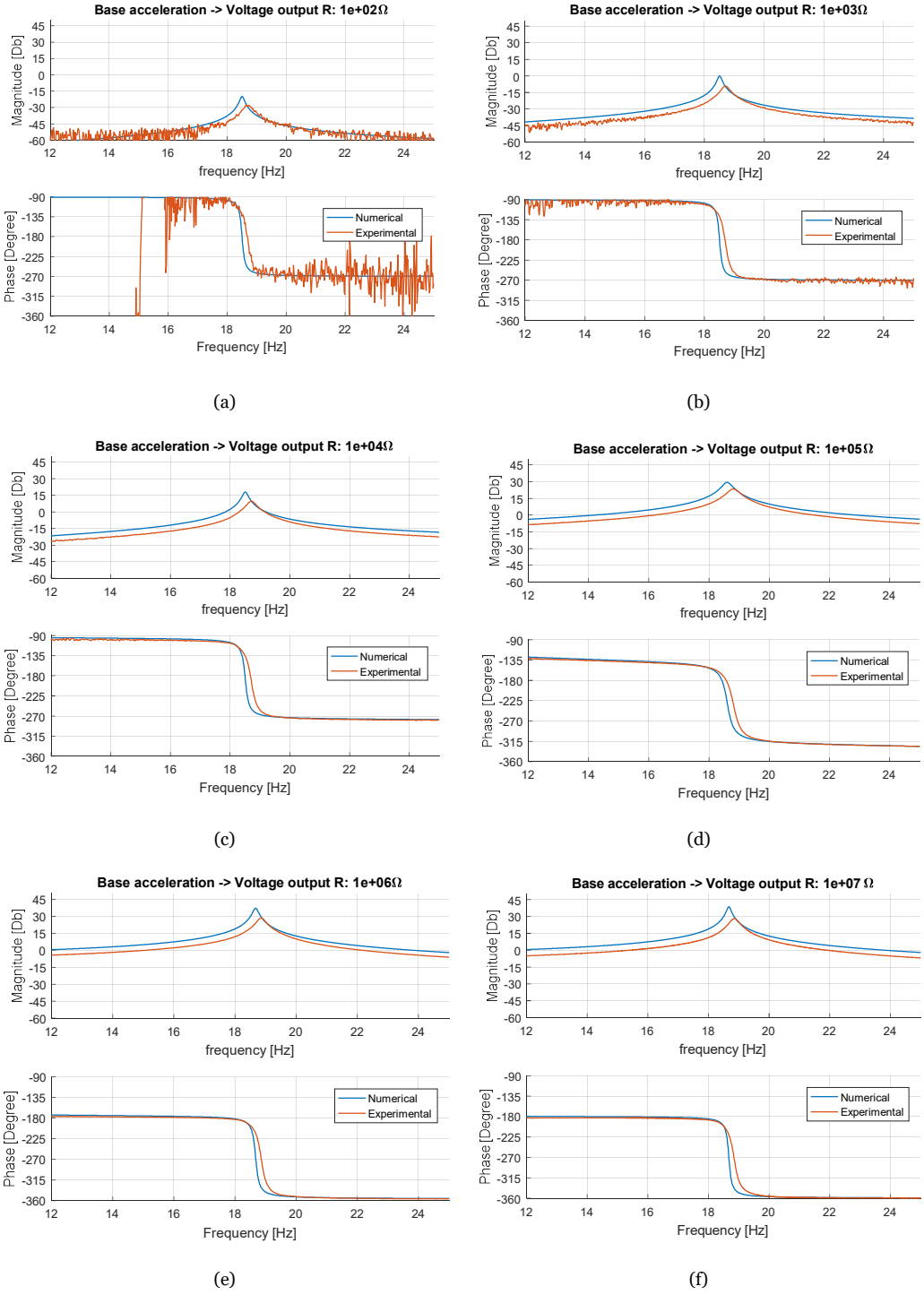

Figure 4.18 Prot. B: transfer functions from base acceleration to voltage output compared with experimental results for (a) R=10 Ω (b) R=1 kΩ (c) R=10 kΩ (d) R=100 kΩ (e) R=1 MΩ (f) R=10 MΩ

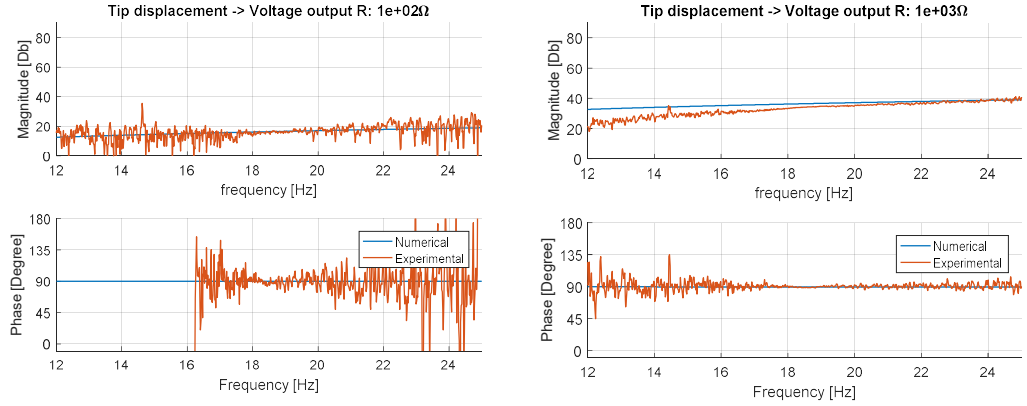

(a)

(b)

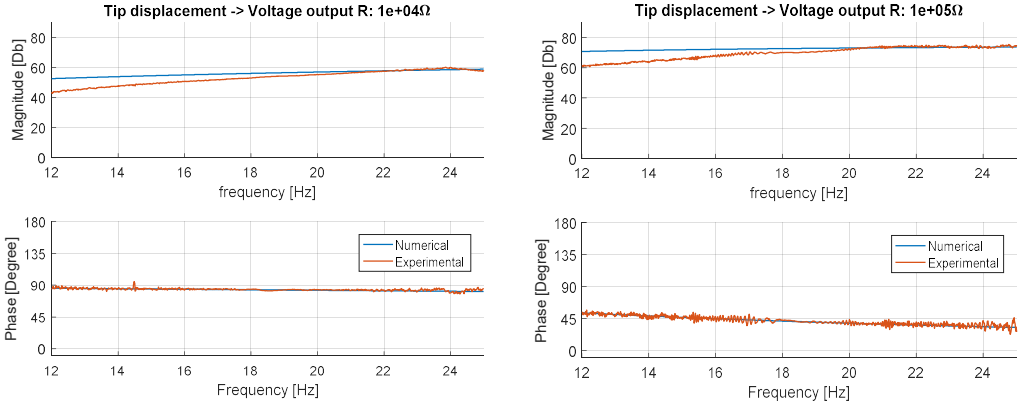

(c)

(d)

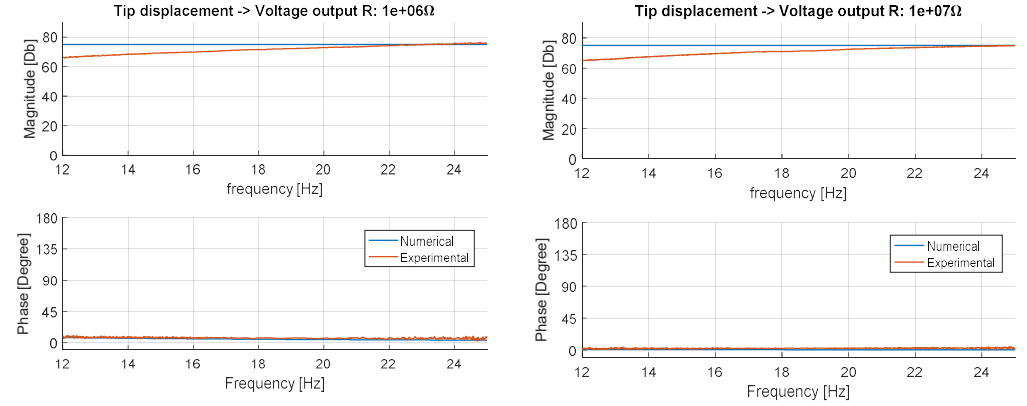

(e)

(f)

Figure 4.19 Prot. B: transfer functions from tip displacement to voltage output compared with experimental results for (a) R=10 Ω (b) R=1 kΩ (c) R=10 kΩ (d) R=100 kΩ (e) R=1 MΩ (f) R=10 MΩ

4.6 Validation of the aero-electro-mechanical model

Wind tunnel test are performed to validate the aero-electro-mechanical model with both prototypes at different wind speeds. First, experimental results obtained for the prototypes are illustrated, with explanations for the discrepancies found with respect to the predictions. Before being able to compare numerical and experimental data, the two main parameters of the aerodynamic force, a_1 and a_3, are identified according to two proposed methods. Finally, a full validation is shown for the output power and voltage produced by a working prototype for different resistances connected and wind speeds applied.

4.6.1 Experimental tests results

The wind tunnel tests are reported with reference to the limit cycle oscillation reached by the prototype for a constant wind speed. The graphs reported are inclusive of the theoretical galloping and lock-in wind speed, respectively U_g and U_r (according to the values reported from literature. Prot. B shows a big discrepancy with respect to the theory, as can be observed in Figure 4.20: the LCO amplitudes grows in correspondence to the lock-in frequency, but as the galloping onset speed is overpassed, no instability is triggered. Moreover, the LCO are clearly visible only for the VIV effect; beyond the lock-in range the motion of the system is highly irregular as the one reported in Figure 4.21.

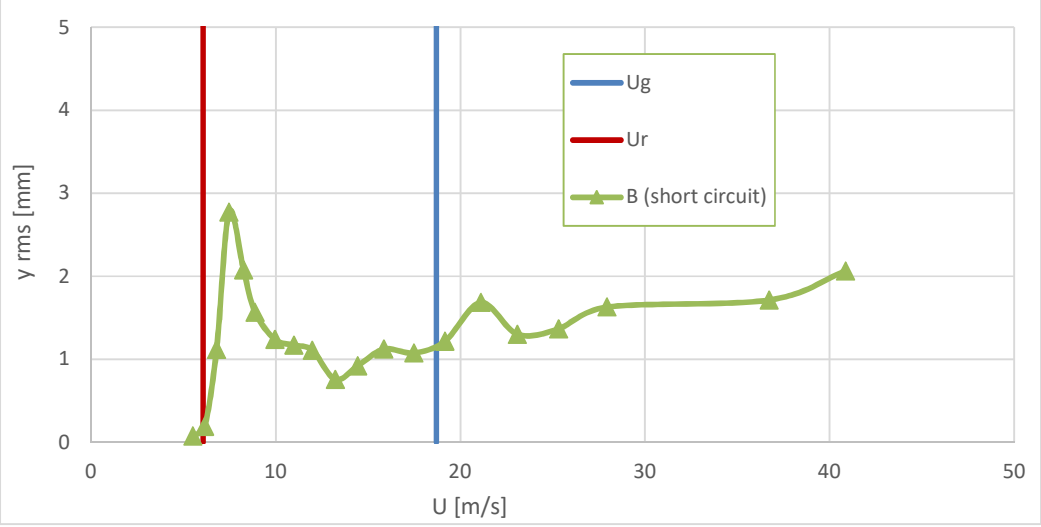

Figure 4.20 Prot. B, short circuit connection: LCO amplitudes (rms) for different wind speed

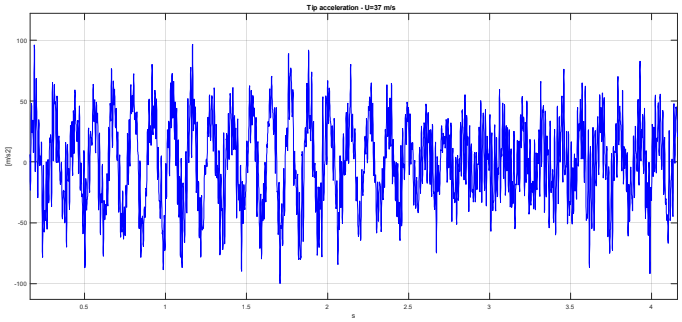

Figure 4.21 Prototype B, short circuit, tip acceleration for U=37 m/s

The fact that the instability is not triggered up to a wind speed twice higher than the one predicted brings to the assumption that the highly non-linear damping is interfering with the galloping instability, or that non-negligible three-dimensional effects are effectively changing the aerodynamic force model. In order to prove the first hypothesis other tests are carried out on the various versions realized from prototype B. Without the piezoceramics in particular, prototype B- is able to gallop even if the experimental onset speed is not that predicted for galloping, but the lock-in speed, see Figure 4.23(a). In this case the non-dimensional damping is found to be linear and not dependent upon the level of oscillations, as for all the others prototypes without the piezoceramics. In particular, the non-dimensional damping (h=0.2%) is inferior to that of Prot. B, meaning that the predicted galloping speed will be lower. Notice that, since $U_g < U_r$, this test confirms what it is observed in other studies under the name of quenching effect. It is also proven that, even for prot. B+, which has a higher non-dimensional damping (h=0.6%), the instability is still triggered for the lock-in frequency (in this case $U_g > U_r$), see Figure 4.23(b). This fact seems to confirm that at low reduced speeds the galloping force model developed according to the quasi-steady aerodynamics is not reliable.

The next improvement in the non-dimensional damping. achieved with prot. B++ (h=1.3%), brings to results similar to that found for prot. B, see Figure 4.23(c). In the lock-in range the limit cycles are clearly visible, but out of the synchronization range an irregular motion characterizes the response of the system. The galloping instability is not triggered up to wind speed four time higher than the predicted onset speed, proving that a sufficiently high damping for this configuration can prevent the instability from happening. It is confirmed that the comparable non-dimensional damping of prot. B is preventing it from undergoing galloping.

According to the sensitivity analysis performed in Chapter 3, the possibility to obtain a lower galloping speed is achieved by means of a longer bluff body, which is achieved with prot. B++ext. In the latter case, the plot in Figure 4.23(d) shows a similar behavior to that of prot. B- and prot. B+: the instability is triggered again for the lock-in speed and the LCO amplitudes continue to grow with the wind speed.

In order to evaluate the importance of three-dimensional effects, prototype D is tested and the results are reported in Figure 4.23(e). In the plot, despite a significantly higher non-dimensional damping (h=2.3%), the galloping phenomenon is observed in a way similar to the results obtained with prot. B-, B+, B++ext. In all those cases, it is observed an almost linear relationship between the LCO amplitude and the wind speed beyond the lock-in range, as claimed by Parkinson and Smith [2].

As a final example, prototype D+m is considered, which shows a greater modal mass and lower frequency due to the effects of the tip mass added, see in Figure 4.23(f). As a consequence, the galloping onset speed is moved outside the range of the lock-in frequency and the effects of the two instabilities are observed in separate regions. The lock-in instability is found to be significant only in a small range of wind speeds as in the cases of prot. B and prot. B++, where the galloping instability is not triggered and the same phenomenon is clearly observed. Beyond the synchronism region there is a region where no oscillations are perceived. At higher wind speeds, instead, the galloping region begins with a different behavior. A hysteresis is in fact found in the plot as the wind speed is increased or decreased in a quasi-static way. This result is not in disagreement with the theory presented, but it shows the limit of a third order approximation for the galloping speed, when this effect is decoupled from VIV. A hysteresis would be in fact predicted in the numerical model, using a 7-th order polynomial for the galloping force. Experimental results on the presence of hysteresis are found in several works, starting from the paper by Parkinson and Smith [2], but, to the Author's knowledge, no other example is found in the GPEH literature. An example of the galloping motion is reported in Figure 4.22 for a wind speed equal to 5.5 m/s.

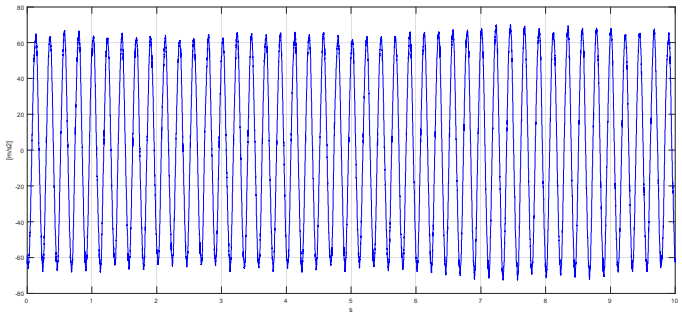

Figure 4.22 Prototype D+m, R=10 MΩ: LCO tip acceleration for U=5.5 m/s

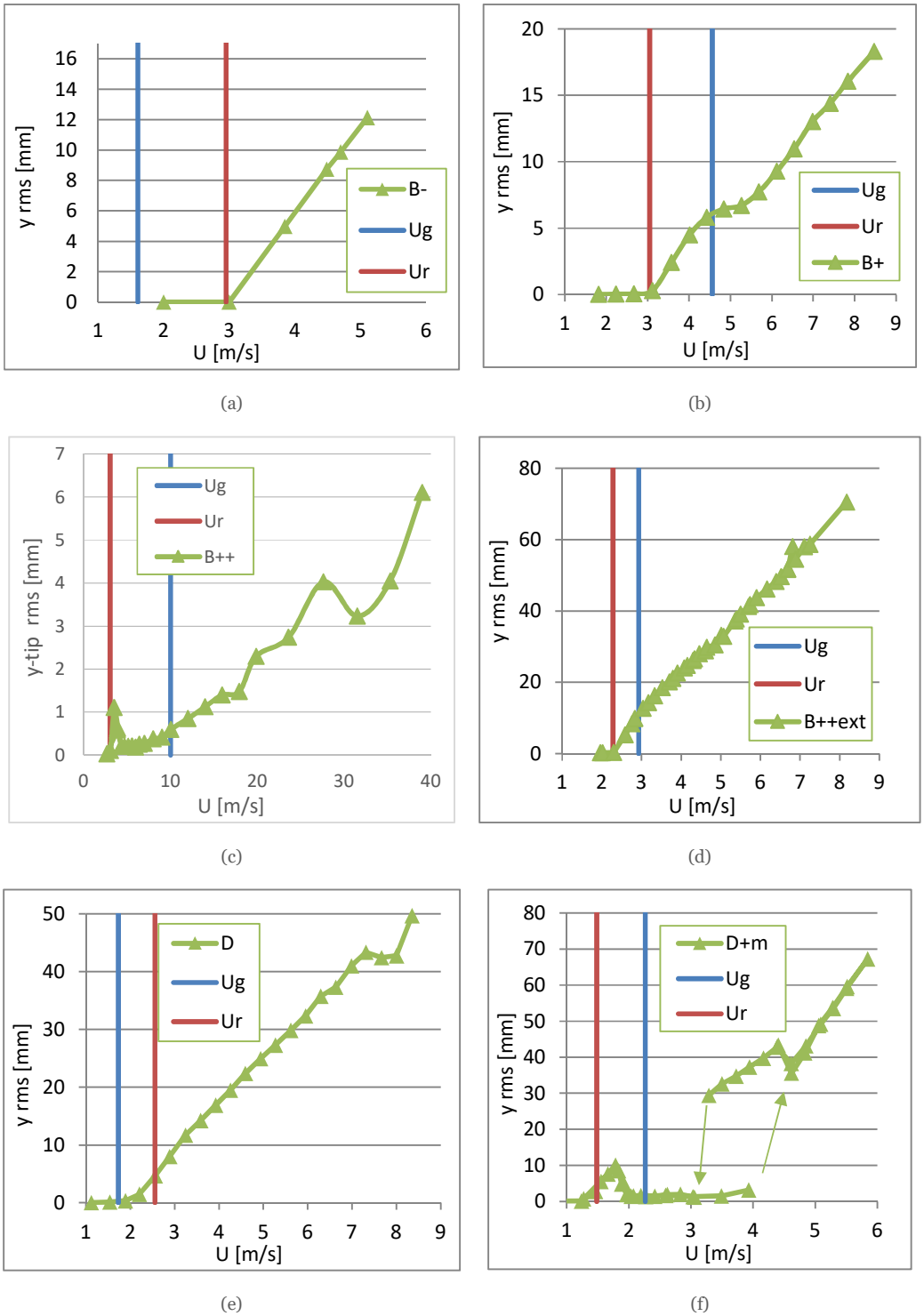

Figure 4.23 Limit cycle rms oscillation amplitudes reached by (a) prot. B- (b) prot. B+ (c) prot. B++ (d) prot. B++ext (e) prot. D, R=10 MΩ (f) prot. D+m, R=10 MΩ

4.6.2 Identification of the aerodynamic parameter

The aerodynamic force model is evaluated through experiments: the first conclusions are drawn with respect on the interaction with the VIV instability for various Scruton number. The theoretical aerodynamic coefficients are then proved to be inaccurate to describe the real behavior of the GPEH prototypes and therefore an identification procedure is set up. The final model is applied in order to validate the displacement, voltage and power levels obtained for prototype D+m.

Build-ups

The build-ups are tests in which the wind speed is kept constant at a value higher than the onset galloping speed, so that the oscillation cycles reached galloping instability are clearly visible. At the beginning of each test, the device is blocked at its equilibrium position and then left free to oscillate, so that the measurements obtained represent the forced motion transient of the system. As an example, three buildups are shown in Figure 4.24, each showing a different behavior for a different wind speed.

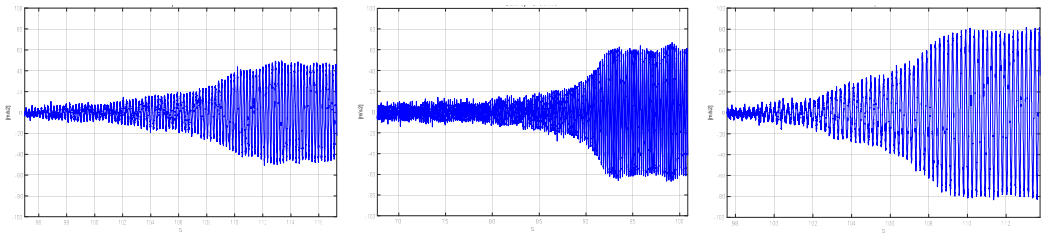

(a) (b) (c)

Figure 4.24 prototype D, R=10 MΩ: tip acceleration measured over time during build-up tests for with (a) U=4.1 m/s (b) U=6.0 m/s (c) U=6.8 m/s

As far as the oscillation amplitude is limited, it is also possible to neglect the effect of the third order part of the aerodynamic force. As can be recalled from the first chapter, the aerodynamic force can be consequently expressed as an equivalent damping action. It can then be stated that the overall damping is:

$$h_{tot} = h - \frac{\frac{1}{2} a_1 \rho D U \int_0^{L_3} \phi^2 dx}{2 m \omega_0} \tag{4.22}$$

where the contribution of mechanical and aerodynamic damping are added. Thus, the motion of the system is assumed to be described by the free motion solution:

$$y(t) = e^{-\alpha t}(A\cos(\omega t) + B\sin(\omega t)) \tag{4.23}$$

where $\alpha = \omega h_{tot}$. The overall non-dimensional damping can be retrieved from the build-up tests, once the logarithmic decrement technique has been applied to identify the value of α.

Therefore, as the value of the total non-dimensional damping acting on the system is known, it is then directly obtained the value of a_1 that corresponds to the measured non-dimensional damping at a certain wind speed U:

$$a_1 = \frac{2m\omega_0(h - h_{tot})}{\frac{1}{2}\rho DU\int_0^{L_3}\phi^2 dx} \tag{4.24}$$

In order to estimate the overall non-dimensional damping acting on the system, the transients, measured in acceleration, are filtered with a pass-band filter around the first mode of vibration. Results for the prototypes that showed an unstable behavior are shown in Figure 4.25, where almost the same trend is found between the different devices tested. In particular, it is evident that for the smallest ratio of wind speed over lock-in speed a very different value of a_1 is found. This higher value can be explained with the fact that the quasi-steady theory is not reliable in such range of velocities and therefore the more meaningful values for the coefficient are to be looked for at high reduced wind speed.

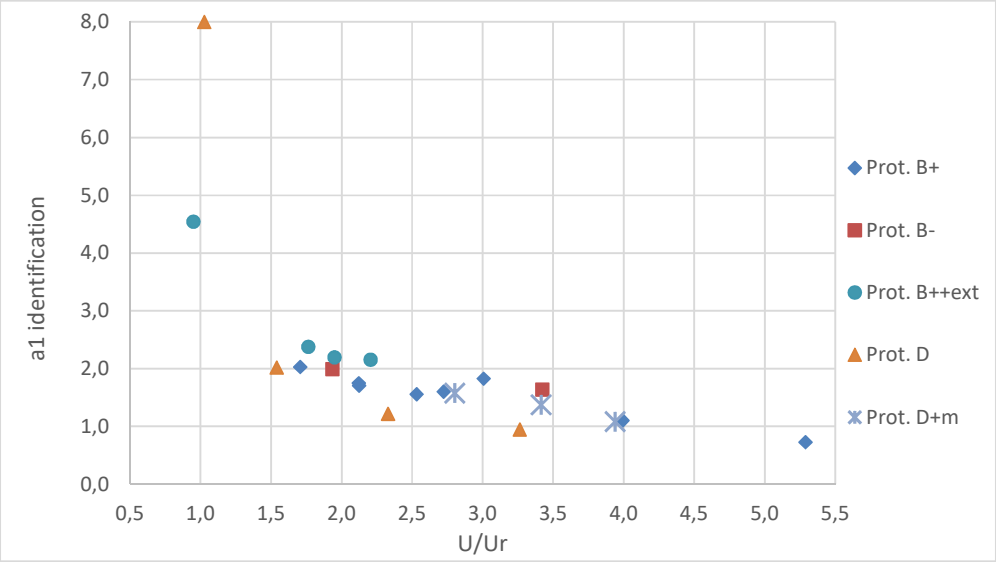

Figure 4.25 Estimation of a1 for different prototypes using build-ups

A more detailed investigation is set in order to define the reliability of this identification procedure. The hypothesis of a negligible third order contribution in the galloping force

approximation is re-examined in Figure 4.26: the identification method described is applied on the same prototype B+ analyzing sets of data for different wind speeds with a common amplitude of oscillation. The results show that there is a greater disagreement in the estimation as the amplitude grows, and therefore, as the contribution of the term in a a_3 becomes more meaningful. The only valid sets of data should be, in principle, the ones with the smallest level of oscillation. It is clear from the plot however, that the smallest level of amplitudes presents also the major scattering and are not usable. A different and more reliable procedure for the identification of the aerodynamic coefficient is needed.

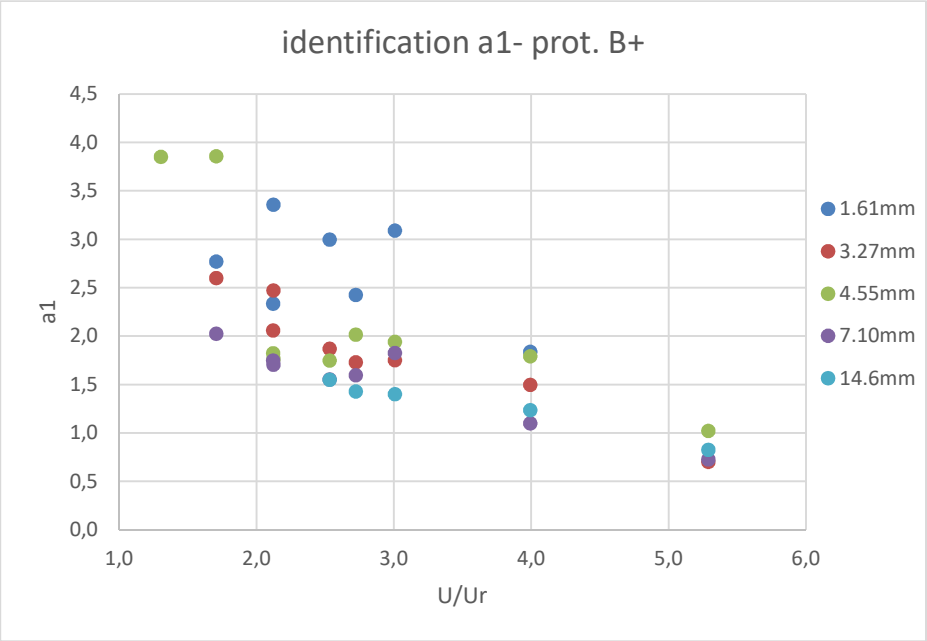

Figure 4.26 Prot. B+: comparison of identified values of a_1 for different level of oscillation amplitudes

Analytical LCO prediction and LS identification

The steady state response of a GPEH under galloping instability is, as known, a sinusoidal motion with constant frequency. Under the assumption that the transient is expired and that the frequency of the LCO cycles is the I mode frequency, it is possible to write:

$$y(t) = Y_0 \cos(\omega t) \tag{4.25}$$

where ω is the first mode frequency, Y_0 is the amplitude of the harmonic and y the tip body displacement considered during the LCO. The velocity of such motion in time will be therefore:

$$\dot{y}(t) = -Y_0\omega \sin(\omega t) \tag{4.26}$$

The cycle of oscillation is also characterized by a time period $T = \frac{2\pi}{\omega}$. During a period of the oscillation a balance of energies can be written in the form:

$$\Delta E_{aero} + \Delta E_{ele} + \Delta E_{dis} + \Delta E_k \tag{4.27}$$

being E_{aero} the energy produced by the flow on the body, E_{ele} the electrical energy dissipated by the piezoelectric conversion, E_{dis} the energy dissipated through mechanical damping and E_k the kinetic energy. If one considers that the variation of kinetic energy is constant among one cycle and if the effect of the electric dissipation of energy are neglected, expression (4.27) reduces to:

$$\Delta E_{aero} = \Delta E_{dis} \tag{4.28}$$

The energy dissipated through mechanical losses is equal to:

$$\Delta E_{dis} = -\int_0^T r\dot{y}^2(t)\, dt \tag{4.29}$$

where the damping action is supposed proportional to the speed and equal to $r = 2h\omega M^*$. If the expression assumed for the speed in equation (4.26) is substituted, it is found:

$$\Delta E_{dis} = -\int_0^T r(-Y_0\omega \sin(\omega t))^2\, dt \tag{4.30}$$

That can be solved as:

$$\Delta E_{dis} = -(Y_0\omega)^2 r\frac{T}{2} \tag{4.31}$$

The aerodynamic energy introduced during a period of oscillation can be evaluated as the wind power integrated over the cycle time as:

$$\Delta E_{aero} = \int_0^T F_{aero}\dot{y}(t)dt \tag{4.32}$$

Once the aerodynamic force F_{aero} is substituted it is found:

$$\Delta E_{aero} = \int_0^T \frac{1}{2}\rho D U^2 \left[a_1 \frac{\dot{y}}{U} \int_0^{L_3} \phi^2 dx + a_3 \left(\frac{\dot{y}}{U}\right)^3 \int_0^{L_3} \phi^4 dx \right] \dot{y} dt \tag{4.33}$$

Again, the expression (4.26) for the speed $\dot{y}$ is substituted, thus obtaining:

$$\Delta E_{aero} = \int_0^T \frac{1}{2}\rho D U^2 \left[a_1 \frac{(-Y_0\omega \sin(\omega t))^2}{U} \int_0^{L_3} \phi^2 dx + a_3 \frac{(-Y_0\omega \sin(\omega t))^4}{U^3} \int_0^{L_3} \phi^4 dx \right] dt \tag{4.34}$$

Constant terms are taken out of the integral that is split in the following two parts:

$$\Delta E_{aero} = \frac{1}{2}\rho D \left[a_1 U (Y_0\omega)^2 \int_0^{L_3} \phi^2 dx \int_0^T \sin^2(\omega t)\, dt + a_3 \frac{(Y_0\omega)^4}{U} \int_0^{L_3} \phi^4 dx \int_0^T \sin^4(\omega t) dt \right] \tag{4.35}$$

The integrals are then solved as:

$$\Delta E_{aero} = \frac{1}{2}\rho D \left[a_1 U (Y_0\omega)^2 \int_0^{L_3} \phi^2 dx \frac{T}{2} + a_3 \frac{(Y_0\omega)^4}{U} \int_0^{L_3} \phi^4 dx \frac{3T}{8} \right] \tag{4.36}$$

By equating the final expressions obtained for the aerodynamic energy in (4.36) and the dissipation of energy due to mechanical losses in (4.31) the following equation is obtained:

$$(Y_0\omega)^2 2h\omega M^* \frac{T}{2} = \frac{1}{2}\rho D \left[a_1 U (Y_0\omega)^2 \int_0^{L_3} \phi^2 dx \frac{T}{2} + a_3 \frac{(Y_0\omega)^4}{U} \int_0^{L_3} \phi^4 dx \frac{3T}{8} \right] \tag{4.37}$$

This equation may be simplified by dividing for the common terms, thus obtaining the following analytical expression for the harmonic motion:

$$Y_0{}^2 = \frac{2hM^*\omega - \rho D\, a_1 U \int_0^{L_3} \phi^2 dx}{\frac{3}{8}\rho D a_3 \frac{\omega^2}{U} \int_0^{L_3} \phi^4 dx} \tag{4.38}$$

This expression is equivalent to the one developed by Barrero-Gil et al. [3] according to the Krylov-Bogoliuvov method. Clearly this prediction is meaningful as long as the electrical power produced by the piezoceramics is negligible and as far as the structural damping can be assumed constant for the oscillation cycle.

Based on the experimental limit cycle amplitudes for various wind speeds a linear regression is set in order to retrieve empirical values of a_1 and a_3 according to the analytical formula in equation (4.38). The latter is re-written with focus on the aerodynamic coefficients:

$$a_1\left(\rho DU\int_0^{L_3}\phi^2 dx\right)+a_3\left(Y_0{}^2\frac{3}{8}\rho D\frac{\omega^2}{U}\int_0^{L_3}\phi^4 dx\right)=2hM^*\omega \tag{4.39}$$

The equation can then be stated in the form:

$$f(a_1,\ a_3)=X \tag{4.40}$$

If a set of maximum tip displacement $\overline{Y_0}$ and a vector of the relative wind speeds $\overline{U}$ are known, it is possible to estimate the values of the aerodynamic coefficients according to a Least Square procedure. It is important to observe that the hypothesis on a negligible level of power consumption can be easily achieved on any prototype by means of a short-circuit connection, so that this method can be applied to any prototype.

The procedure is applied for the wind speeds that have a ratio U/Ur sufficiently higher than unity, so that the steady LCO considered are to be related with the galloping instability only and not with the VIV. This means that the identified parameters are assumed to be a valid approximation only where the reduced velocity is high enough to reduce the effect of vortex resonance. Results are presented into families according to the prototype category.

The identified parameters with LS for prototype B+ and B++ext are reported in Table 4.10, where it is observed that the first order coefficient is similar to the theoretical one. The coefficient a_3 shows instead a great discrepancy with respect to the theory, but this could be justified since the short bluff body adopted gave raise to important three dimensional effects. Thus, a third order coefficient with a smaller value than expected, produces smaller LCO amplitudes with respect to the galloping theoretical force model as described in Figure 4.27(a) (b) (c). In particular, it is meaningful to observe that the estimation gives an insight on the importance of three-dimensional effects: the weight of the third order contribution for the galloping force is in fact significantly lower as the bluff body length is increased. This consideration, which is not in agreement with the bi-dimensional flow assumption, brings to the conclusion that a shorter bluff body will exhibit a different galloping force. The higher a_3, the smaller is expected to be the aerodynamic force acting on the body for the same level of body speed. The latter remark confirms that three-dimensional effects are non-negligible for the slenderness ratio considered and can be interpreted as a loss in the generation of mechanical energy from the galloping instability, that is more evident as the ratio $\frac{L}{D}$ is lowered.

Prototype	B+	B++ext	Theoretical [3]
a_1	2.242	2.362	2.3
$\pm\sigma$ (estimated)	$\pm$ 0.039	$\pm$ 0.077	
a_3	-67.353	-45.262	-18
$\pm\sigma$ (estimated)	$\pm$ 3.438	$\pm$ 2.962	

Table 4.10 Aerodynamic coefficients identified for prototypes A-, B-,B++ext with respect to the theoretical values

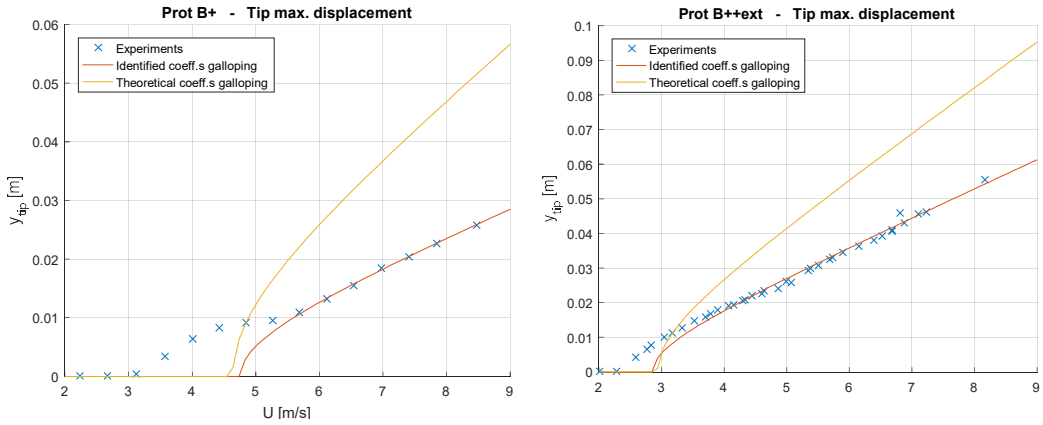

(a) (b)

Figure 4.27 Comparison between the theoretical and identified galloping force model with the experimental results for (a) Prot. B+ (b) B++ext

The case-comparison for prototypes D and D+m is instead illustrated in Table 4.11, where again the coefficient a_1 is around the range of the theoretical value, but the third order coefficient is well below the theoretical value. The decrease of the second aerodynamic coefficient is in agreement with the hypothesis of meaningful three-dimensional effects. It is to be noticed however that, despite having the same bluff body length, the coefficients a_3 identified from the two prototypes are different from one another. It is observable from the experimental LCO obtained that the case of prototype D shows an important interaction with VIV instability as observed in the previous section. The matching between the theoretical and the estimated galloping force model is shown in Figure 4.28(a) for prototype D, where a good agreement is found for all the wind velocities using the identified parameters. The case of prototype D+m, where the VIV-galloping interaction is almost null, does not predicts any

motion for the lock-in frequency as depicted in Figure 4.28(b). The identified force model is instead well matched by the experiments only beyond the critical galloping speed. Furthermore, the hysteretic jump is not described, since it would require a higher order polynomial as the theory developed by Parkinson and Smith predicted [2].

Prototype	D	D+m	Theoretical [3]
$a_1 \pm \sigma$ **(estimated)**	2.676 ± 0.025	2.192 ± 0.030	2.3
$a_3 \pm \sigma$ **(estimated)**	-9.710 ± 0.190	-2.848 ± 0.156	-18

Table 4.11 Aerodynamic coefficients identified for prototypes D and D+m with respect to the theoretical values

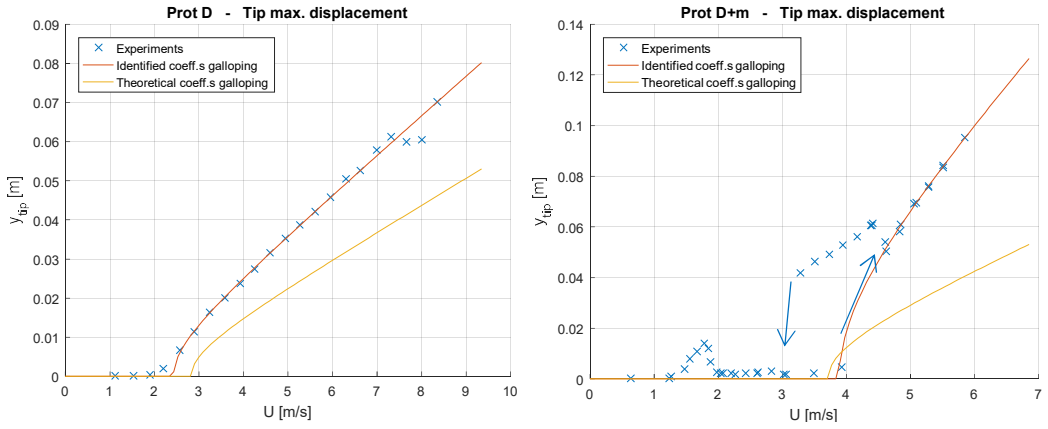

(a) (b)

Figure 4.28 Comparison between the theoretical and identified galloping force model with the experimental results for (a) Prot D (b) Prot. D+m

4.6.3 VIV-galloping interference

With the use of the identified models for the galloping force acting on each prototype, this section analyzes the effects of the VIV-galloping interference as the model parameters are changed. The power spectral densities of the experimental results are commented at various wind velocities, in order to highlight the effects of the lock-in resonance. The main effect that this interference has on the present research is that it represents a problem in terms of aerodynamic validation: the galloping force modeled is in fact valid only outside the range of lock-in speeds. Thus, if the GPEH is found to undergo an unstable motion right beyond the lock-in speed, it is not possible to identify the wind speed of incipient galloping instability.

For the latter reasons, before proceeding with the validation of the prototypes, this interaction needs to be studied.

Lock-in frequency

As known from theory, the vortex shedding phenomenon changes its frequency proportionally to the wind speed as stated in the expression $f_s = \frac{c_S U}{D}$. This property is verified for instance on the prototype B++, as depicted in Figure 4.29, where the excited frequency follows the expression of the Strouhal frequency and, for a value close enough to the fundamental frequency, the lock-in resonance raises up. It is interesting to notice that, for a very short range of synchronism, the VIV is induced also on the second mode of vibrations, as the Strouhal frequency is close to the second resonance.

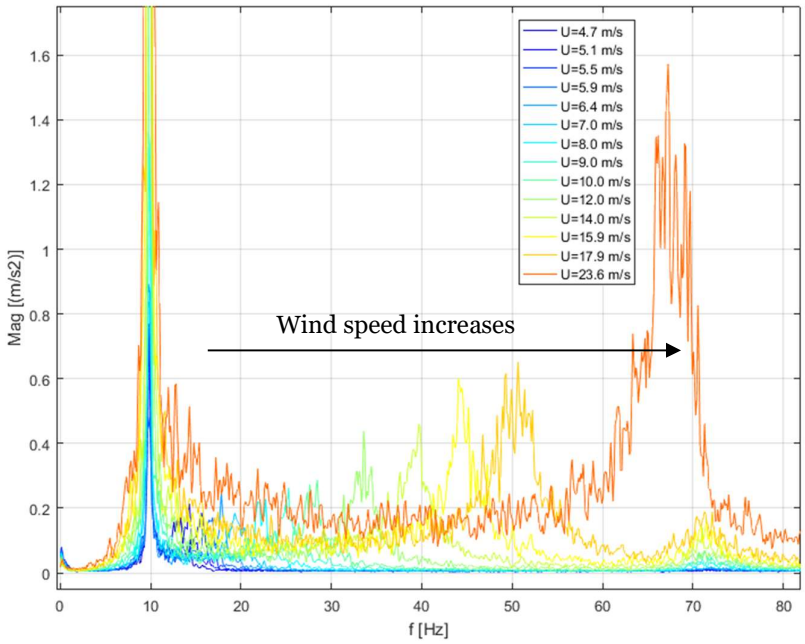

Figure 4.29 Prototype B++: Fourier spectrum for tip acceleration

Considering a prototype such as prot. D, that showed an unstable behavior right beyond the lock-in speed, a spectrum such as the one described in Figure 4.30 can be observed in this case. It is noticed that the only frequency excited is the natural frequency and therefore the galloping and vortex shedding effects are perfectly coupled, even for the considered range of wind speeds, slightly higher that the lock-in speed. For the latter reason, it is not possible to validate the model in this case, where the instabilities are superimposed.

Prototype D+m is then considered, since this prototype has the property to separate the two instabilities. In particular, looking at Figure 4.31, one can notice that, as the wind speed is increased, a clear contribution of the vortex-shedding frequency is present at growing frequencies (even when galloping is triggered). On the other hand, the lock-in effect is found only for a short range of frequency, beyond which the contribution on the first mode of vibration is minimum up to the galloping onset. Beyond this second threshold, the power spectral density is collected again on the natural frequency of the GPEH, due to the effects of a galloping instability.

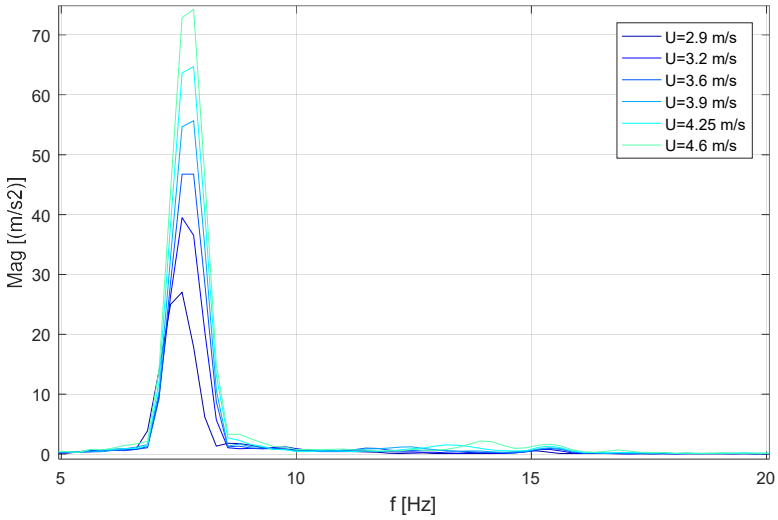

Figure 4.30 Prot. D: Fourier spectrum for tip acceleration

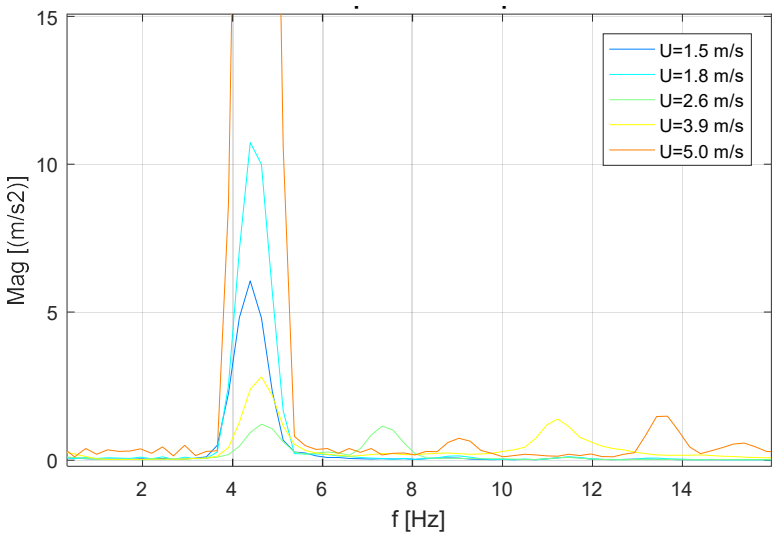

Figure 4.31 Prototype D+m, R=10 MΩ: Fourier spectrum for tip acceleration

Notice that the possibility to separate the range of interest of the galloping and VIV instability depends on the ratio U_g/U_r. The latter was already shown to depend upon the Scruton number and therefore it is easily increased by increasing the modal mass or the non-dimensional damping. These two possibilities are considered in the following sections.

Tip mass variation

The addition of a mass implies an increase in the Scruton number and therefore brings to the separation between VIV and galloping. The prototypes considered in this case are two prototypes, D and D+m, with the same bluff body dimension and a comparable non-dimensional damping. Prototypes D and D+m constitute a valuable example where the higher mass yields to the total separation of the galloping instability from the VIV range as described in Figure 4.32. This phenomenon has been attested with detailed experiments in the work by Mannini et al. [36], who claimed that a sufficient Scruton number can isolate the galloping instability from that of vortex shedding.

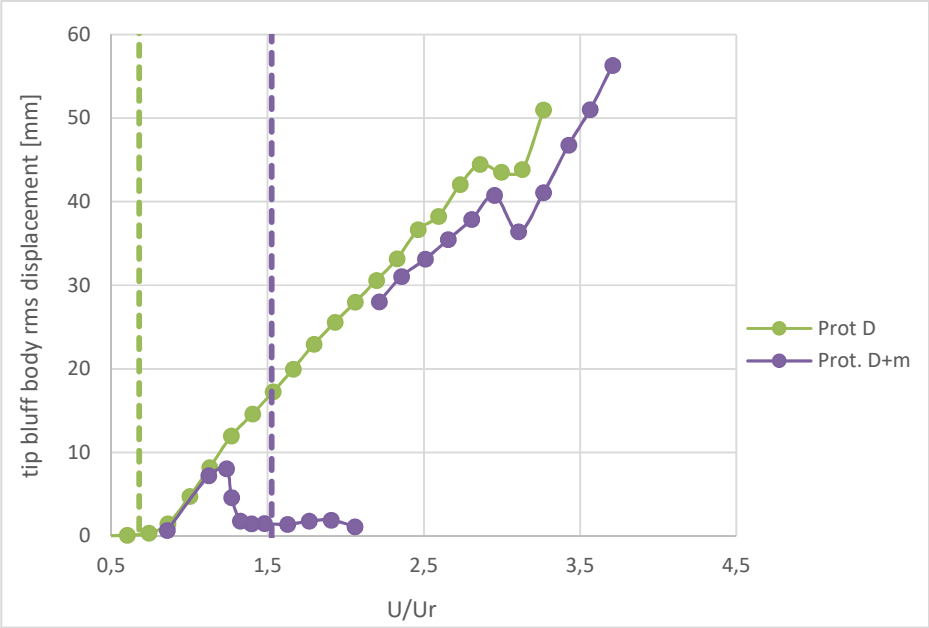

Figure 4.32 Std tip displacement for Prot. D and D+m for various wind speeds

Mechanical damping variation

The damping ratio sensitivity is illustrated in Figure 4.33, where prototypes B-,B+, B++ are compared. These three prototypes show a different damping ratio, while all the other properties are kept constant. The increase of such parameter results in an increased ratio U_g/U_r, that, at high values, stops the so-called VIV-galloping interference. This effect can be observed in Figure 4.33 for prot. B++, where the onset instability is no longer triggered at U_r, as is the case for the lightly damped prototypes B- and B+.

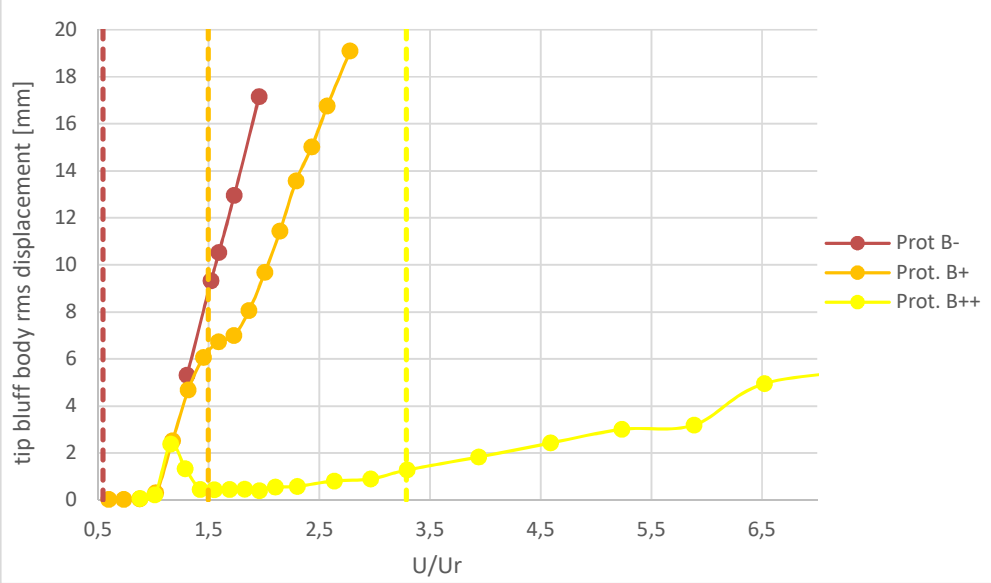

Figure 4.33 Comparison of std amplitudes of oscillation for Prot. B- B+ and B++

Bluff body length variation

The addition of an extension to the bluff body increases the area over which the galloping force is exerted and therefore lowers the galloping onset speed. This observation is sustained by the comparison between the experimental results obtained for prot. B++ and prot. B++ext. It is shown in Figure 4.34 that while the shorter bluff body does not reach the onset speed for galloping, the extended version is subject to a VIV-galloping instability starting from U_r.

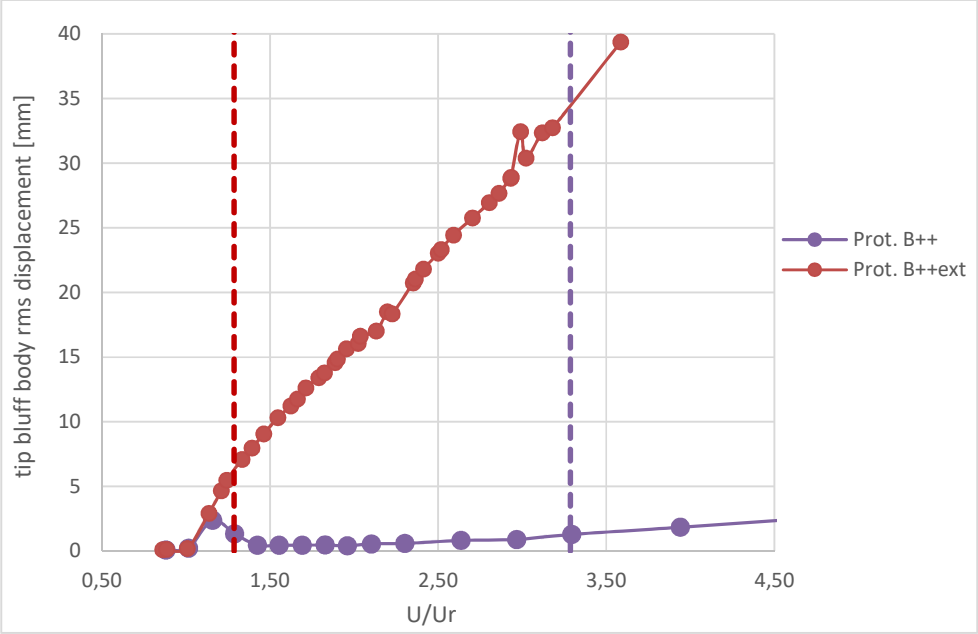

Figure 4.34 LCO amplitudes (std) for Prot. B++ and B++ext and galloping onset speeds (dashed lines)

4.6.4 Experimental validation of a complete GPEH

The validation procedure is completely presented for the case of prototype D+m: this model is in fact chosen for having a very good separation between VIV and galloping instabilities. The numerical model is fit with the identified galloping force coefficients and the modal mass and frequency experimentally retrieved from the base vibration setup. The experimental tests at different wind speeds are carried out for three resistances. Results for the tip displacement reached during the LCO are reported in Figure 4.35, with good agreement for all the resistances used. The voltage produced on the piezoceramic is reported in Figure 4.36, while the power generated is compared in Figure 4.37. Both these last two graphs show a moderate accuracy in comparison to the experiments. The optimal power is given by the 100 kΩ resistance, as predicted by the simulations, while the highest voltage level is given by the highest resistance applied. No significant difference is found on the amplitudes reached as the resistance is varied since the percentage of mechanical energy converted into electrical energy is very low in all cases. The highest power level reached is around 16 μW, which is a very low value and due to the small value of the electromechanical coupling.

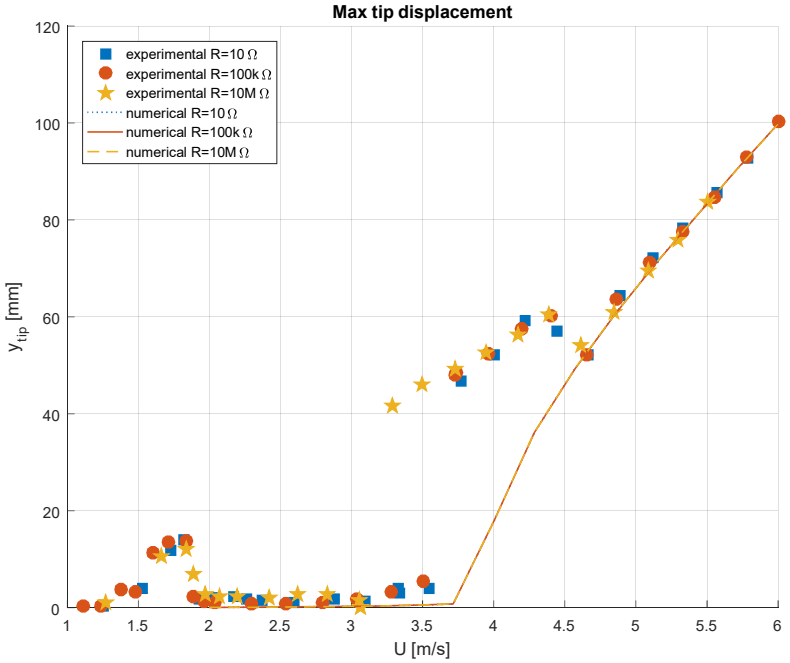

Figure 4.35 Max. tip displacement from experiments (asterisks) and predicted (dashed line)

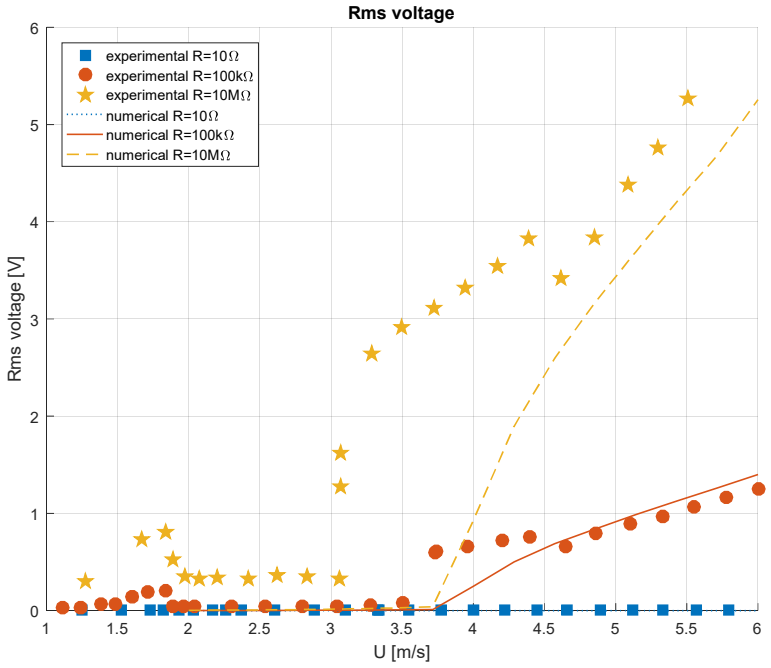

Figure 4.36 Rms voltage from experiments (asterisks) and predicted (dashed line)

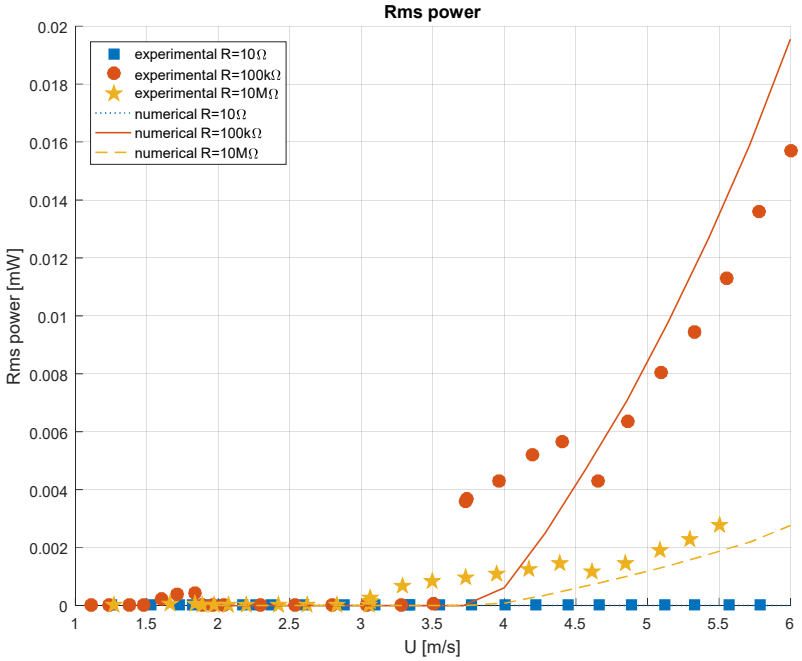

Figure 4.37 Rms power from experiment (asterisks) and predicted (dashed line)

4.7 Results

The model realized is proved capable to predict with good accuracy the modal mass and frequency of the first mode of vibration and its modal shape. The electromechanical part of the numerical model is also validated with detailed observations on the transfer functions obtained for three different prototypes and the first mode distributed model is found capable of providing a good matching with the tests. Under the aerodynamical point of view, the prototypes realized confirm the main results of the sensitivity analysis developed in Chapter 3. In particular, as the bluff body length is increased, or equivalently, as the damping ratio is decreased, the GPEH can gather an unstable behavior thanks to galloping at a lower onset speed. The observations on the VIV-galloping interaction are proved to be dependent on the ratio U_g/U_r as other studies predicted. The increase of this ratio by means of a higher damping or modal mass is proved to be able to separate the two instabilities. As the two phenomena are split into different ranges of wind speeds, a hysteresis is found to interest the galloping instability. This result brings to a limitation of the third-order approximation adopted and shows that a 7-th order polynomial is required to describe the two branches of LCO found. Meanwhile, the quasi-steady hypothesis is found to be reliable for a high-enough reduced velocity, while the initial assumption of negligible three-dimensional effects is found to be wrong, especially for low values of the slenderness ratio. For the latter reason, a specific identification procedure is set in order to retrieve the proper polynomial approximation of the galloping force model, substituting the theoretical aerodynamic coefficients. A final validation of the power output and displacements obtained demonstrates the accuracy of the overall model for the region of high wind speeds.

CONCLUSIONS

This work develops a coupled non-linear distributed model for a longitudinal configuration of a GPEH. A sensitivity analysis is performed by integrating the model equations with numerical methods. It is stated that the objective in the optimization of a GPEH are: a sufficiently high average power generation for the range of wind speeds considered, an electromechanical coupling that is sufficient to guarantee control regulation of the limit cycle amplitudes and oscillation below the critical level. It is found that the electromechanical coupling is increased, by increasing the thickness of the beam, by using a clamp position that leave the largest area of the PZT exposed to strain, to increase the distance between the neutral axis and the PZT layer, or by achieving a high stiffness for the regions where the PZT layer is not involved. The power output is increased only for an optimal bluff body length and beam width and thickness, for a high mass, by means of a proper side length or density. The galloping onset speed is found to be dependent on the simplified relation based on a first order approximation of the aerodynamic force. The latter highlights the fact that the side dimension does not influence the galloping onset speed, but that a proper cross-section geometry and a longer bluff body length helps decreasing it, as well as having a lightly damped system.

The experimental campaign carried out in this research demonstrates the validity of the model developed. In particular, the electromechanical system is verified by forced base motion using a shaker: very good approximation of the experimental behavior is proven in correspondence to the natural frequency. However, the tests show a significant non-linearity in the damping coefficient of the piezoelectric element for the range of oscillation of interest, with deep consequence on the model assumed and the galloping onset speed. The aerodynamic force is evaluated in a wind tunnel facility on a wide range of wind speeds. An ad hoc identification procedure is set in order to retrieve empirical values for the aerodynamic coefficients of the galloping model. The estimated galloping force applied to the complete coupled non-linear model is able to match very well the results obtained by the various prototypes for what concern the limit cycle oscillations and the power output. The sensitivity analysis results are confirmed using different prototypes and tests for what concerns the non-dimensional damping, the bluff body length and the bluff body density.

Three dimensional effects are found to be meaningful especially for the smallest ratios of L/D. The interaction between vortex shedding and galloping is proven to be a significant effect that does not respect the quasi-steady theory applied. This effect is found to be dependent on the mass-damping parameter and it is proven that the two phenomena can be studied separately by means of an appropriate added tip mass. The present model is therefore shown to be valid only for a certain range of wind speed, which is an important consequence for the galloping energy harvesting technique since it shows the limit of applicability of the hypothesis adopted. It is also shown that if the reduced speeds are not sufficiently high in the region in which galloping is expected to occur, no instability may arise if the interaction with vortex shedding is not strong enough. A maximum power output of 0.02 mW is produced by the final prototype, for a wind speed of 6 m/s.

The main challenge for future research efforts are related to the optimization of the present device in terms of power and size reduction. In the next prototype to be built the piezoelectric element will be chosen with care on its non-linear damping characteristic and a higher electromechanical coupling will be a task to achieve. Since a conclusion of this work is that three-dimensional effects are non-negligible for the prototype considered, the bluff body length is a meaningful parameter to lower them as it is increased. For the latter reason, the T-shaped layout will be investigated, since it makes possible the use of longer bluff body without a decrease of the electromechanical coupling. The prototype will also be tested with different power acquisition methods in order to demonstrates which is the most suitable method.

APPENDIX A

A.1 Autonomous Wireless Sensor Network

Under the acronym of WSN (Wireless Sensor Network) there have been conducted a number of researches aimed at defining a new generation of sensor communication with enhanced characteristics for information capability, diagnosis possibility and heath control. A self-powered sensor that is able to communicate in a wireless network open a huge scenario currently being investigated for a wide range of applications. With respect to a traditional cabled network there is not only the advantage to reduce setup cost and maintenance cost, but also the opportunity to collect more significant and reliable information.

Wireless sensor node

The basic unit of a WSN is a wireless sensor node. This unit is designed for a self-powered functioning and an autonomous communication with the other nodes in the network. It is basically composed by a central controller, an energy harvesting device, a sensing unit and a transmission system as represented in.

The harvester has to provide sufficient average power to the rest of the device. It is comprised of an appropriate circuitry that has to accomplish this task. The harvester in fact, may be not considered as a continuous source of energy because of the discontinuity of the source from

which the energy is extracted. For this reason, a proper circuit has to collect the power and store it in order to make it available when needed by the system.

The sensor unit is aimed at gathering information from the surrounding environment by means of sensors that send their information to the central unit. It is composed by an interface that includes analog-to-digital converter (ADC) which converts the signal from the sensors into readable values for the central core.

The wireless module is responsible for the data streaming to air at a certain frequency and power depending on the number of data to be transmitted and the distance at which the communication is requested. In general, it operates discontinuously with a certain frequency and in accordance to the availability of a communication channel with the network.

The core unit of the whole system is a processor which is responsible for the other subsystems interfaces and correct functionality. It may have also to process the information that it receives from the sensors in order to communicate autonomously on the environment status. In general, the controller is also accompanied by a memory unit that is used for storing the information acquired in a queue, while the device waits before a data connection is set. This centralized controller has also the task to impose a certain duty cycle and to activate or deactivate the sleep mode in order to maintain the sufficient average power granted by the energy harvester.

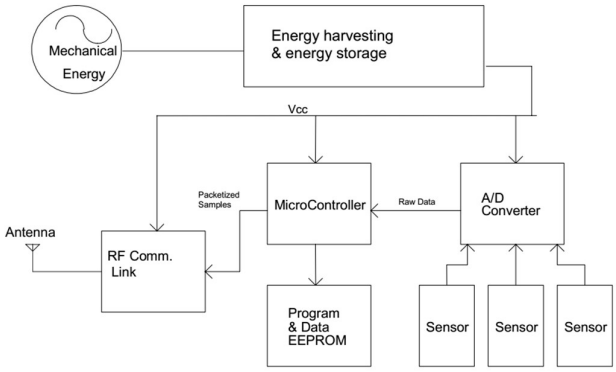

Figure 4.38 Schema of a wireless self-powered mechanical energy harvester

Power requirements

The system power requirements are commonly dictated by the wireless module mounted. Control unit and sensors do not normally require a particular level of power even if they typically operate continuously.

There are many available wireless protocols and modules, which primarily differ for range of connection and power requirements. The most common protocols are

- IEEE 802.11 typically found in WLAN; speed 2-200 Mbps; range 10–100m
- IEEE 802.15 for WPAN applications, subdivided into:
  - IEEE 802.15.3 High Rate WPAN for high quality connection
  - IEEE 802.15.1 which is based on Bluetooth technology with a maximum range of 243.5 m and a maximum speed of 50 Mbit/s
  - IEEE 802.15.4/Low Rate WPAN: very low power demands and low transmission rates

The most common protocols implemented in a WSN are the Bluetooth and the LR-WPAN, especially in the ZigBee and MiWi versions. Few examples of commercially available sensor nodes are listed in Table 4.12 with focus on the average power required. It is clear that a wireless module must be used with care with respect to the power available and that the management of its cyclic activations from sleep modes is a key point for a better device efficiency.

	Crossbow MICAz	**Intel IMote2**	**Jennic JN5139**
Radio standard	IEEE 802.15.4/ZigBee	IEEE 802.15.4	IEEE 802.15.4/ZigBee
Typical range	100 m (outdoor), 30 m (indoor)	30 m	1 Km
Data rate (kbps)	250 kbps	250 kbps	250 kbps
Sleep mode (deep sleep) 2.8 µA (1.6 µA)	15 µA	390 µA	2.8 µA (1.6 µA)
Processor only	8 mA active mode	31–53 mA	2.7+0.325 mA/MHz
RX	19.7 mA	44 mA	34 mA
TX	17.4 mA (+0dbm)	44 mA	34 mA (+3 dBm)
Supply voltage (minimum)	2.7 V	3.2 V	2.7 V
Average	2.8 mW	12 mW	3 mW

Table 4.12 Comparison of commercial wireless module sensors

Power management

In order to prevent the system from running out of power the Sensor Node must be able to balance the rate of discharge and the rate of charge. The prototype assembled by Arms et al. [61], that is reported in Figure 4.39 (a), has proved capable of shutting down power consuming elements so to allow energy storage elements to be re-charged. It was also experimentally verified that the streaming data consumption could be reduced by approximately 9 times if the data to be sent is previously logged and/or processed. The authors also proposed and applied the following methods in order to reduce the average power consumed by the system sensing elements:

- Turn on power to the sensors only when sampling
- Sample sensor(s) only on event
- Reduce the sensor sample rate to the minimum required by the application
- Sleep between samples
- Maximize bandwidth of electronics to minimize electronics settling time

and by the system RF transceiver elements:

- Reduce the total amount of data transmitted through compression
- Lower to the minimum the transceiver duty cycle and frequency of data transmission
- Implement strict power management – use power down and sleep modes
- Transmit only on sensor event(s)

When higher sampling rate are required, it may be convenient, depending on the application requests, to program the node to sample bursts of data at the desired frequency, provided that the energy stored is sufficient to deliver the peak currents needed.

Existing applications

As the advances in WSN technologies grow a new paradigm of network is being experimented in many class of applications. Habitat monitoring is for example a field in which WSN outclasses traditional cabled network. In fact, it is a substantially more economical method for conducting long-term studies and it is also less invasive for the habitat involved. An example of habitat monitoring network is the one set by Mainwaring et al. [62] which consists of 32 sensing nodes. In this kind of application, the outdoor

conditions must be prevented from damaging the sensor node and appropriate materials must be employed such as the ones proposed by the authors in Figure 4.39 (c).

Other environment monitoring may also be set for an increased productivity in agriculture. An example for this category is the monitoring of a vineyard status developed by Beckwith et al. [63], which implements multiple nodes with humidity and temperature sensors for a better control of the grapes growing.

WSN does also suggest enhanced characteristics that can be applied to bring more useful information to the end-user. A significant example is the A-life prototype presented by Michahelles et al. [64] that offers a triage feature for avalanche rescue, by combining and evaluating the information received from the sensors applied on each companion.

In medical field an autonomous concept for Body Sensor Network is under investigation, which applies wearable or implantable technology and ambient sensors in order to monitor patients' health status. The main challenges for BSN are illustrated by Lo and Yang [65] and may be synthetized as:

- Sensor sensitivity to motion artifacts, interference and bio-fouling, that could be tackled by using multiple sensors in array so to fuse information and improve reliability.
- The wearable and implantable device must be completely biocompatible and must also use a wireless communication involving low power radios to minimize radiation.
- Autonomic sensors are needed which provide properties such as: self-management, self-configuration, self-optimization, self-healing, self-adaptation, self-integration and self-scaling.
- A secure and protected communication protocol must be adopted in order to guarantee the patients' privacy.

Structural Health Monitoring

The purpose of Structural Health Monitoring (SHM) is to access a building, bridge or vehicle operational status in order to prevent damage and to avoid non-effective scheduled maintenance. WSNs are an interesting opportunity for this topic because they offer to deploy a cost-effective network with the possibility of entering inaccessible locations for a cabled classic network.

Nevertheless, wireless structural monitoring systems open a set of technical challenges if compared to traditional networks: wireless transmission is inherently less reliable and with

lower transfer rate, it also requires a high-power demand for the energy harvesting device and it requires a perfect clock synchronization of multiple sensing units. A comparison between a cabled network and a new generation of wireless autonomous sensing nodes was done by Wang et al. in the monitoring of the Voigt Bridge [66]. The prototype built include a piezoelectric energy harvesting unit as can be seen in Figure 4.39(d). The authors validated the accuracy of the sensing unit, after observing that there was a close match between the data collected by the two network systems with a strong agreement of the two sets of FFT.

Another relevant prototype is the self-powered wireless sensor designed for a pump condition monitoring described by Discenzo et al. [67]. This unit extracts energy from ambient vibrations using a tuned piezoelectric element that is indicated in Figure 4.39(b) and report wirelessly on the status of the machinery to a central station.

Lynch and Loh [68] have reviewed an emerging concept in which the wireless node has the enhanced capability to command an actuation unit. The so called active sensing wireless node is then able to interact with its environment typically by means of a piezoelectric patch. Grisso et al. [69] have proposed a prototype called MEMS-Augmented Structural Sensor with the purpose of performing impedance based SHM. This device is tailored to use a piezoelectric element for sensing, actuation and power harvesting. It has been proved that the node is able to conduct a structural test among the environment by sending a sinusoidal mechanical input signal to the structure it is attached to. It has been shown that with this method it is possible to detect a crack in a beam or to evaluate the damage level of a structure.

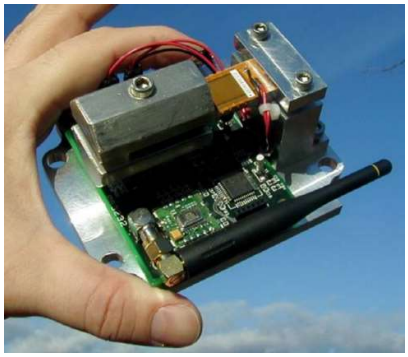

(a)

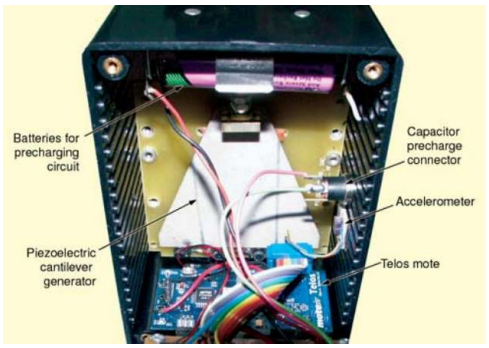

(b)

(c)

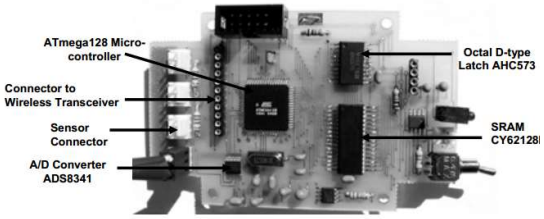

(d)

Figure 4.39 Existing Wireless Sensor Node with energy harvesting capabilities

APPENDIX B

B.1 Datasheet

PRODUCT DATA

V406 and V408 Shakers
Metric

Performance Parameters and Characteristics*

Shaker	V406	V408
Standard LDS Amplifier	PA500L	
Sine Force (peak) – forced air cooled	196 N	196 N
Armature Resonance (f_n)	9 kHz	9 kHz
Useful Frequency Range	5 Hz – 9 kHz	5 Hz – 9 kHz
Effective Mass of Moving Element	0.200 kg	0.200 kg
Velocity (sine peak)	1.78 m/s	1.78 m/s
Maximum Acceleration (sine peak) – naturally cooled	50 g	50 g
Maximum Acceleration (sine peak) – forced air cooled	100 g	100 g
Max. Random Force (rms)	89 N	89 N
Displacement (pk–pk) – continuous	17.6 mm	17.6 mm
Suspension Axial Stiffness	12.3 N/mm	12.3 N/mm
Aux. Suspension Axial Stiffness	35.1 N/mm	35.1 N/mm
Shaker Body Mass – base mounted	14.1 kg	14.1 kg
Shaker Body Mass – trunnion mounted	22.7 kg	22.7 kg
Impedance at 500 Hz	2.5 Ω	2.5 Ω
Cooling Air Flow	0.014 m^3/s	0.014 m^3/s
Armature Diameter	38 mm	38 mm
Armature Insert Pattern:		
Centre Insert	1	1
2.54 mm PCD†	6	6
Insert Threads	M4	10/32 UNF

* Shaker ratings are those which can be achieved with a larger amplifier than that supplied as standard.
† PCD inserts equi-spaced

This range of permanent magnetic shakers is ideal for vibration testing of components, small assemblies or modal and structural analysis. The shakers' efficient armature design enables them to deliver impressive peak forces and accelerations over a wide frequency range.

The V400 series are wide frequency band electro-dynamic transducers capable of producing a sine vector force up to 196 N. They are also suitable as non-seismic pick-ups and are widely used in educational and research establishments to investigate the dynamic behaviour of structures and materials.

Features
- Wide frequency band combined with high peak forces
- Low mass, high performance armature construction
- Base or trunnion mounted
- Powered by compact, quiet and energy efficient amplifiers
- Robust, lightweight suspension system provides excellent torsional and traverse stiffness with minimal impact on system acceleration

Industry Applications
- Modal and structural analysis
- Electronic assembly testing
- Laboratory experiments and various medical purposes
- Fatigue and resonance testing
- Use as velocity transducer or high speed actuator

Brüel & Kjær

Some of the features listed are available as standard, others as options. Please contact Brüel & Kjær for advice on the optimum specification to meet your system needs

System Characteristics

V406/8 Shaker + LDS Amplifier	PA100E	PA500L
System Sine Force (peak) – naturally cooled	98 N	98 N
System Sine Force (peak) – forced air cooled	98 N	196 N
System Velocity (sine peak)	1.52 m/s	1.78 m/s
System Displacement (pk–pk) – continuous	14.0 mm	17.6 mm
System Maximum ½-sine Shock Force*	90 N	200 N
System Random Force (rms) – ISO5344	38 N	89 N
Acoustic Noise at 1 m Distance:†		
Shaker‡ – naturally cooled	82 dBA	82 dBA
Shaker‡ – forced air cooled	105 dBA	105 dBA
Amplifier	silent	47 dBA
Total Heat Dissipation:		
Shaker	340 W	340 W
Amplifier	0.15 kW	0.8 kW
Shaker Cooler Fan	–	0.46 kW
Max. Working Ambient Temperature:		
Shaker	30° C	30° C
Amplifier	35° C	40° C
Electrical Requirement:		
Amplifier	1.3 kVA	1.3 kVA
Cooling Fan	0.2 kVA	0.25 kVA
Amplifier Rating	0.147 kVA	0.7 kVA
Maximum Shaker Weight	22.7 kg	
Maximum Dimensions (H × W × D)	273.8 × 165 × 259 mm	

* ½-sine shock force is calculated with the standard payload, 2 ms pulse width, 10% pre/post pulse
† Measured at a height of 1.60 m above floor level in enclosed cell
‡ Maximum noise when running at full level

Amplifier Data

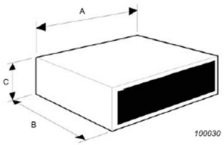

	PA100E	PA500L
A:	340 mm	340 mm
B:	290 mm	290 mm
C:	270 mm	270 mm
Wgt:	25 kg	25 kg

Characteristics:		
Rated Sinusoidal Power Output – matched resistive load	147 W (2R9)	500 W
Signal-to-noise Ratio	>75 dB	>75 dB
Total Harmonic Distortion – at rated output	Typically 0.5%	Typically 0.1%
Input Sensitivity for Maximum Output (400 Hz)	1.0 V rms	1.0 V rms
Amplifier Efficiency	58%	59%
Voltage Regulation	3%	2%
Maximum Continuous Sinusoidal VA Output (0.5 pf)	147 VA	700 VA
Frequency Range – at rated power	10 Hz – 10 kHz	20 Hz – 14 kHz
Output Current – at rated VA	7 A rms	18 A rms
Random Output Current	14 A pk	54 A pk
Maximum Output Current	7 A rms	18 A rms
Maximum Output Voltage	20 V rms	40 V rms
Maximum No Load Voltage	32 V rms	45 V rms
Overcurrent Trip Level	10 A rms	19 A rms
Protection	Fast acting current limit	Output device protection

Shaker Options

Insert Selection:	
M4	◆
10/32" UNF	◆
Mounting Selection:	
Base Mounting	◆
Support Trunnion	●
Other Options:	
Cooling Fan	◆
Auxiliary Suspension	●

Key:
◆ Standard – Available on shortest delivery
● Option – Stocked item, available on short delivery

Cooling Fan

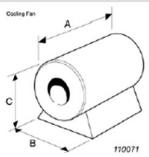

Dim. A:	389 mm
Dim. B:	241 mm
Dim. C:	249 mm
Weight:	17 kg

Health and Safety

Designed in accordance with:
- EN 61010 – 1:2001

Complies with the following EU directives:
- EMC: 2004/108/EC
- Machinery: 2006/42/EC
- Low Voltage: 2006/95/EC

Make Our Experience Your Advantage
From application engineering, installation and training through to maintenance, spares and repairs, Brüel & Kjær offers a total service approach to keep your system operating efficiently and reliably. All LDS systems (standards and specials) are designed and manufactured to ISO9001. Brüel & Kjær offers a comprehensive range of vibration, measurement and analysis equipment. Please consult our website for details.

BP 2399 – 12 2012-05 Brüel & Kjær reserves the right to change specifications and accessories without notice.

HEADQUARTERS: Brüel & Kjær Sound & Vibration Measurement A/S · DK-2850 Nærum · Denmark
Telephone: +45 7741 2000 · Fax: +45 4580 1405 · www.bksv.com · info@bksv.com
Local representatives and service organisations worldwide

Brüel & Kjær

2.1 PRODUCT: PPA-1001

The PPA-1001 is a single layer product recommended for energy harvesting and sensing applications. It also exhibits good performance as a resonant actuator. It is not recommended for applications requiring high force output. This product does not have mounting and alignment holes like the other products; but it is the most cost effective option Midé has.

SPECIFICATIONS

Overview	
Capacitance (nF)	100
Mass (g)	2.8
Full Scale Voltage Range (V)	±120

Layer Material[1]	Thickness (mils)	Thickness (mm)
Polyester	2.0	0.05
Copper	1.4	0.03
PZT 5H	6.0	0.15
Stainless Steel 304	6.0	0.15
Polyimide	1.0	0.03
Total	18.0	0.46

[1]Information on material properties is provided in Section 5.

[2]The layer thicknesses do not perfectly add up to the actual thickness of the product due to the epoxy layers. These epoxy layers can be ignored for finite element analysis however.

Stiffness			
Parameter	Clamp -6	Clamp 0	Clamp 6
Effective Stiffness (N/m)	N/A	452.15	275.52
Effective Mass (g) Max Peak to Peak	N/A	0.918	0.714
Deflection (mm)	N/A	24.0	20.0

See Section 4.3 for more information on how to use this data to tune your piezo.

DESCRIPTION

Performance data for the PPA-1001 is summarized in the following tables and plots. Refer to Section 6 for information on how this data was gathered. Please note that this data is to be used only as reference and that there is some variability from unit to unit. Temperature, clamp conditions, drive quality, all can contribute to additional variability. All test data was gathered at room temperature and with the PPA-9001 clamp kit hardware.

DIMENSIONS

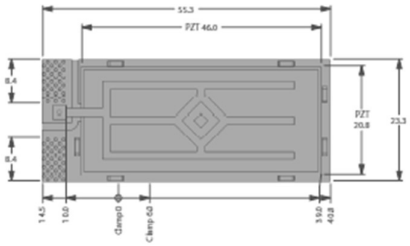

Figure 9: The overall dimensions (mm) for the PPA-1001 are shown. The total thickness is 0.46 mm (18 mils).

2.2 PRODUCT: PPA-1011

The PPA-1011 is recommended for energy harvesting and sensing applications. It also exhibits good performance as a resonant actuator.

SPECIFICATIONS

Overview	
Capacitance (nF)	100
Mass (g)	3.0
Full Scale Voltage Range (V)	±120

Layer Material[1]	Thickness (mils)	Thickness (mm)
FR4	3.0	0.08
Copper	1.4	0.03
PZT 5H	6.0	0.15
Copper	1.4	0.03
FR4	14.0	0.36
Total[2]	28.0	0.71

[1]Information on material properties is provided in Section 5.

[2]The layer thicknesses do not perfectly add up to the actual thickness of the product due to the epoxy layers. These epoxy layers can be ignored for finite element analysis however.

Stiffness			
Parameter	Clamp -6	Clamp 0	Clamp 6
Effective Stiffness (N/m)	267.45	446.28	591.81
Effective Mass (g) Max Peak to Peak	0.645	0.614	0.506
Deflection (mm)	21.0	20.5	17.0

See Section 4.3 for more information on how to use this data to tune your piezo.

OVERVIEW

Performance data for the PPA-1011 is summarized in the following tables and plots. Refer to Section 6 for information on how this data was gathered. Please note that this data is to be used only as reference and that there is some variability from unit to unit. Temperature, clamp conditions, drive quality, all can contribute to additional variability. All test data was gathered at room temperature and with the PPA-9001 clamp kit hardware.

DIMENSIONS

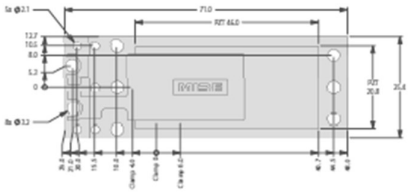

Figure 14: The overall dimensions (mm) for the PPA-1011 are shown. The total thickness is 0.71 mm (28 mils).

BIBLIOGRAPHY

[1] J. P. Den Hartog, Mechanical Vibrations, New York: Dover Publications, 1956.

[2] G. V. Parkinson and J. D. Smith, "The square prismas an aeroelastic nonlinear oscillator," *Quarterly Journal of Mechanics and Applied Mathematics,* vol. 17, pp. 225-239, 1964.

[3] A. Barrero-Gil, G. Alonso e A. Sanz-Andres, «Energy harvesting from transverse galloping,» *Journal of Sound and Vibration,* n. 329, p. 2873–2883, 2010.

[4] L. Zhao, L. Tang e Y. Yang, «Comparison of modeling methods and parametric study for a piezoelectric wind energy harvester,» *SMART MATERIALS AND STRUCTURES,* vol. 22, p. 125003 (12pp), 2013.

[5] J. Sirohi e R. Mahadil, «Harvesting Wind Energy Using a Galloping Piezoelectric Beam,» *Journal of Vibration and Acoustics,* vol. 134, p. 011009 (8pp), 2012.

[6] A. Bibo e M. F. Daqaq, «On the optimal performance and universal design curves of galloping energy harvesters,» *AIP Applied Physics Letters,* n. 104, p. 023901 (pp6), 2014.

[7] A. Bibo e M. F. Daqaq, «An analytical framework for the design and comparative analysis of galloping energy harvesters under quasi-steady aerodynamics,» *Smart Materials and Structures,* vol. 24, p. 094006 (16pp), 2015.

[8] S. J. Roundy, Energy Scavenging for Wireless Sensor Nodes with a Focus on Vibration to Electricity Conversion, The University of California, Berkeley, 2003.

[9] T. Starner, "Human-powered wearable computing," *IBM SYSTEMS JOURNAL,* p. (12pp), 1996.

[10] S. R. Anton e H. A. Sodano, «A review of power harvesting using piezoelectric materials (2003–2006),» *SMART MATERIALS AND STRUCTURES,* vol. 16, p. R1–R21, 2007.

[11] J. M. Gilbert e F. Balouchi, «Comparison of Energy Harvesting Systems for Wireless Sensor Networks,» *International Journal of Automation and Computing,* vol. 4, pp. 334-347, October 2008.

[12] S. Percy, C. Knight, F. Cooray e K. Smart, «Supplying the Power Requirements to a Sensor Network Using Radio Frequency Power Transfer,» *Sensors,* vol. 12, pp. 8571-8586, 2012.

[13] S. P. Beepy, R. N. Torah, M. J. Tudor, P. Glynne-Jones, T. O'Donnell, C. R. Saha and S. Roy, "A Micro Electromagnetic Generator for Vibrational Energy Harvesting," *Journal of Micromechanics and Microengineering,* vol. 17, no. 7, pp. 1257-1265, 2007.

[14] A. Premount, Vibration Control of Active Structures, An Introduction 3rd Edition, Universitè Libre de Bruxelles: Springer.

[15] N. E. Du Toit, Modeling and Design of a MEMS Piezoelectric Vibration Energy Harvester, Massachusetts Institute of Technology, 2005.

[16] D. A. Howey, A. Bansal e A. S. Holmes, «Design and performance of a centimetre-scale shrouded wind turbine for energy harvesting,» *SMART MATERIALS AND STRUCTURES,* vol. 20, p. 085021 (12pp), 2011.

[17] S. Priya, "Modeling of electric energy harvesting using a piezoelectric windmill," *AIP Applied Physics Letters,* vol. 87, no. 184101, 2005.

[18] J. Kan and et al, "Study on a piezo-windmill for energy harvesting," *Renewable Energy,*

vol. 97, pp. 210-217, 2016.

[19] G. Diana e F. Cheli, Dinamica e vibrazione dei sistemi, 1993.

[20] L. A. Weinstein, M. R. Caca, P. M. So and P. K. Wright, "Vortex shedding induced energy harvesting from piezoelectric materials in heating, ventilation and air conditioning flows," *SMART MATERIALS AND STRUCTURES,* vol. 21, p. 045003 (10pp), 2012.

[21] M. Zhang e J. Wang, «Experimental Study on Piezoelectric Energy Harvesting from Vortex-Induced Vibrations and Wake-Induced Vibrations,» *Journal of Sensors,* p. (8 pp), 2016.

[22] M. Bryant e E. Garcia, «Modeling and Testing of a Novel Aeroelastic Flutter Energy Harvester,» *Transactions of the ASME,* vol. 133, pp. 011010-1 (11pp), 2011.

[23] H. L. Dai, A. Abdelkefi, U. Javed e L. Wang, «Modeling and performance of electromagnetic energy harvesting from galloping oscillations,» *Smart Materials and Structures,* vol. 24, p. 045012 (11pp), 2015.

[24] H.-J. Jung e S.-W. Lee, «The experimental validation of a new energy harvesting system based on the wake galloping phenomenon,» *SMART MATERIALS AND STRUCTURES,* vol. 20, p. 055022 (10pp), 2011.

[25] S. Li, J. Yuan e H. Lipson, «Ambient wind energy harvesting using cross-flow fluttering,» *Journal of applied Physics,* vol. 109, 2011.

[26] A. Erturk, W. G. R. Viera, C. De Marqui Jr. e D. J. Inman, «On the energy harvesting potential of piezoaeroelastic systems,» *AIP Applied Physics Letters,* vol. 96, p. 184103 (4 pp), 2010.

[27] S. Kwon, "A T-shaped piezoelectric cantilever for fluid energy harvesting," *AIP Applied Physics Letters,* vol. 97, p. 164102 (4pp), 2010.

[28] J. Sirohi e R. Mahadil, «Piezoelectric wind energy harvester for low-power sensors,» *Journal of Intelligent Material Systems and Structures,* vol. 22(18), p. 2215–2228,

2011.

[29] F. Ewere, G. Wang e B. Cain, «Experimental investigation of galloping piezoelectric energy harvesters with square bluff bodies,» *Smart Materials and Structures,* vol. 23, p. 104012 (12pp), 2014.

[30] L. Zhao e Y. Yang, «Enhanced aeroelastic energy harvesting with a beam stiffener,» *Smart Materials and Structures,* vol. 24, p. 032001 (11pp), 2015.

[31] L. Zhao e Y. Yang, «Analytical solutions for galloping-based piezoelectric energy harvesters with various interfacing circuits,» *Smart Materials and Structures,* vol. 24, p. 075023 (24pp), 2015.

[32] Y. Yang, L. Zhao and L. Tang, "Comparative study of tip cross-sections for efficient galloping energy harvesting," *AIP Applied Physics Letters,* vol. 102, p. 064105 (5), 2013.

[33] R. Song, X. Shan, F. Lv e T. Xie, «A study of vortex-induced energy harvesting from water using PZT piezoelectric cantilever with cylindrical extension,» *Ceramics International,* vol. 41, p. S768–S773S768–S773, 2015.

[34] H. D. Akaydin, N. Elvin e Y. Andreopoulos, «Energy Harvesting from Highly Unsteady Fluid Flows using Piezoelectric Materials,» *Journal of Intelligent Material Systems and Structures,* vol. 21, pp. 1263-1278, 2010.

[35] G. Piccardo, L. C. Pagnini and F. Tubino, "Some research perspectives in galloping phenomena: critical conditions and post-critical behavior," *Continuum Mech. Thermodyn.,* vol. 27, no. 1-2, pp. 261-285, 2014.

[36] C. Mannini, A. Marra e T. Massai, «Interference of vortex-induced vibration and transverse galloping for a rectangular cylinder,» *Journal of Fluids and Structures,* vol. 66, pp. 403-423, 2016.

[37] Laneville and Parkinson, "Effects of turbulence on galloping of bluff," *Proceedings of the Third International Conference on Wind,* pp. 787-797, 1971.

[38] A. N. Ryabinin and V. D. Lyusin, "Galloping of small aspect ratio square cylinder," *ARPN Journal of Engineering and Applied Sciences,* vol. 10, no. 1, pp. 134-138, 2015.

[39] A. Barrero-Gil, A. Sanz-Andrès e M. Roura, «Transverse galloping at low Reynolds numbers,» *Journal of Fluids and Structures,* vol. 25, p. 1236–1242, 2009.

[40] L. Carassale, A. Freda e M. Marrè-Brunenghi, «Effects of free-stream turbulence and corner shape on the galloping instability of square cylinders,» *Journal of Wind Engineering and Industrial Aerodynamics,* vol. 123, p. 274–280, 2013.

[41] *Blockage corrections for bluff bodies in confined flows,* ESDU 80024, 1998.

[42] C. Mannini, A. M. Marra e G. Bartoli, «VIV–galloping instability of rectangular cylinders: Review and new experiments,» *Journal of Wind Engineering and Industrial Aerodynamics,* vol. 132, pp. 109-124, 2014.

[43] G. V. Parkinson and M. A. Wawzonek, "Some considerations of combined effects of galloping and vortex resonance," *Journal of Wind Engineering and Industrial Aerodynamics,* vol. 8, pp. 135-143, 1981.

[44] R. M. Coreless e G. V. Parkinson, «A model of the combined effects of vortex induced oscillation and galloping,» *Journal of Fluids and Structures,* vol. 2, pp. 203-220, 1988.

[45] A. Abdelkefi, M. R. Hajj and A. H. Nayfeh, "Power harvesting from transverse galloping of square cylinder," *Nonlinear dynamics,* no. 70, p. 1355–1363, 2012.

[46] A. Erturk e D. J. Inman, «On Mechanical Modeling of Cantilevered Piezoelectric Vibration Energy Harvesters,» *JOURNAL OF INTELLIGENT MATERIAL SYSTEMS AND STRUCTURES,* vol. 19, pp. 1311-1325, 2008.

[47] G. Tomasini, S. Giappino e A. Costa, *Galloping-based piezo-aeroelastic energy harvester for wireless sensors to be installed on freight trains,* Milano,Italy: Politecnico di Milano, 2016.

[48] A. Abdelkefi, Z. Yan and M. R. Hajj, "Power generation from Galloping-based Piezoaeroelastic Energy Harvesters for different cross section geometries," *American*

Institute of Aeronautics and Astronautics, 2013.

[49] A. Erturk e D. J. Inman, «An experimentally validated bimorph cantilever model for piezoelectric energy harvesting from base excitations,» *SMART MATERIALS AND STRUCTURES,* vol. 18, p. 025009 (18pp), 2009.

[50] A. Erturk and D. J. Inman, "A Distributed Parameter Electromechanical Model for Cantilevered Piezoelectric Energy Harvesters," *Journal of Vibration and Acoustics,* vol. 130, p. 041002 (pp15), 2008.

[51] Z. Yan, A. Abdelkefi e M. R. Hajj, «Piezoelectric energy harvesting from hybrid vibrations,» *Smart Materials and Structures,* vol. 23, p. 025026 (14pp), 2014.

[52] L. Tang, L. Zhao, Y. Yang and E. Lefeuvre, "Equivalent Circuit Representation and Analysis of Galloping-Based Wind Energy Harvesting," *IEEE/ASME TRANSACTIONS ON MECHATRONICS,,* vol. 20, no. 2, pp. 834-844, 2015.

[53] M. W. Hooker, "Properties of PZT-based piezoelectric ceramics between -150 and 250°C," *NASA Contract Report,* Vols. Report No NASA/CR-1998-208708, 1998.

[54] A. Abdelkefi, M. R. Hajj e A. H. Nayfeh, «Temperature impact on the performance of galloping-based piezoaeroelastic energy harvesters,» *SMART MATERIALS AND STRUCTURE,* n. 22, p. 055026 (14pp), 2013.

[55] G. Alonso, J. Meseguer and I. Prez-Grande, "Galloping stability of triangular cross-sectional bodies: a systematic approach," *Journal of Wind Engineering and Industrial Aerodynamics,* vol. 95, pp. 928-940, 2007.

[56] M. Novak and H. Tanaka, "Effect of turbolence on galloping instability," *ASCE Journal of the ENgineering Mechanics Division,* vol. 100, pp. 27-47, 1974.

[57] S. C. Luo, Y. T. Chew, T. S. Lee and M. G. Yazdani, "Stability to translational galloping vibration of cylinder at different mean angles of attack," *Journal of Sound and Vibration,* vol. 215, no. 5, pp. 1183-1194, 1998.

[58] A. Abdelkefi, M. R. Hajj e A. H. Nayfeh, «Performance analysis of galloping-based piezoaeroelastic energy harvesters with different cross-section geometries,» *Journal of Intelligent Material Systems and SStructures,* vol. 25, n. 2, pp. 246-56, 2014.

[59] MIDE, *PPA PRODUCTS Datasheet & User Manual,* www.mide.com, 2016.

[60] G. Diana e F. Cheli, Advanced dynamics of mechanical systems, 2015.

[61] S. W. Arms, C. P. Townsend, D. L. Churchill, J. H. Galbreath and S. W. Mundell, "Power Management for Energy Harvesting Wireless Sensors," *SPIE Int'l Symposium on Smart Structures & Smart Materials,* p. (9pp), 9 March 2005.

[62] A. Mainwaring, J. Polastre, R. Szewczyk, D. Culler and J. Anderson, *Wireless Sensor Networks for Habitat Monitoring,* University of California at Berkeley.

[63] R. Beckwith, D. Teibel e P. Bowen, *Unwired Wine: Sensor Networks in Vineyards,* Intel Research, USA: IEEE, 2004.

[64] F. Michahelles, P. Matter, A. Schmidt and B. Schiele, "Applying wearable sensors to avalanche rescue," *Computers & Graphics,* vol. 27, p. 839–847, 2003.

[65] B. Lo e G.-Z. Yang, *Body sensor networks - research challenges and opportunities,* London UK: Institute of Biomedical Engineering - Imperial Collage London.

[66] Y. Wang, K. J. Loh, J. P. Lynch, M. Fraser, K. Law and A. Elgamal, "Vibration Monitoring of the Voigt Bridge using Wired and Wireless Monitoring Systems," *The Proceeding of 4th China-Japan-US Symposium on Structural Control and Monitoring,* 2006.

[67] F. M. Discenzo, D. Chung e K. A. Loparo, «Pump Condition Monitoring Using Self-Powered Wireless Sensors,» *Sound and Vibrations,* pp. 12-15, May 2006.

[68] J. P. Lynch e K. J. Loh, «A Summary Review of Wireless Sensors and Sensor Networks for Structural Health Monitoring,» *The Shock and Vibration Digest,* pp. 91-128, March 2006.

[69] B. L. Grisso, L. A. Martin and D. J. Inman, "A wireless active sensing system for impedance-based Structural Health Monitoring," in *23rd Conference and Exposition on Structural Dynamics*, Orlando, FL; United States, 2005.

ACRONYMS

ADC	Analog to Digital Converter
BSN	Body Sensor Network
COM	Center Of Mass
DAC	Digital to Analog Converter
DAQ	Data AcQuisition System
GECO	Galloping Energy Converter
GPEH	Galloping Piezoelectric Energy Harvester
LCO	Limit Cycle Oscillation
MEMS	Micro Electro-Mechanical Systems
PVDF	Polyvinylidene Fluoride
PZT	Piezoelectric lead Zirconate Titanate
SDOF	Single Degree Of Freedom
SHM	Structural Health Monitoring
VIV	Vortex-Induced Vibration
VPEH	Vibration Based Energy Harvester
WSN	Wireless Sensor Networks